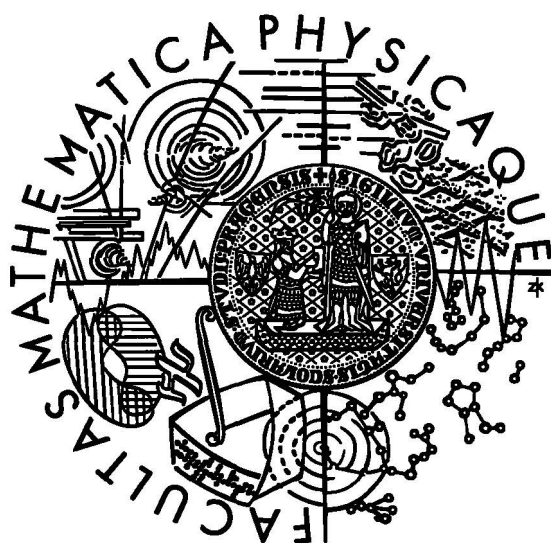Univerzita Karlova v Praze
Matematicko-fyzikální fakulta

DIPLOMOVÁ PRÁCE

Petr Nečesal

Testování modelů interakcí kosmického záření na urychlovači LHC

Prohlašuji, že jsem svou diplomovou práci napsal samostatně a výhradně s použitím citovaných pramenů. Souhlasím se zapůjčením práce.

V Praze dne   Petr Nečesal

Contents

Název práce: *Testování modelů interakcí kosmického zaření na urychlovači LHC*
Autor: *Petr Nečesal*
Katedra (ústav): *Ústav časticové a jaderné fyziky*
Vedoucí diplomové práce: *prom. fyz. Jan Řídký, CSc.*
E-mail vedoucího: *ridky@fzu.cz*

Abstrakt: Kosmické záření obsahuje velmi energetické částice a jádra, které v atmosféře způsobují vznik rozsáhlých atmosférických spršek. Detekce rozsáhlých spršek, které jsou způsobeny primární částicí s energií větší než přibližně 10^5 GeV, se provádí pomocí pozemních detektorů. Vlastnosti primární částice (energie, hmotnost) se určují pomocí rekonstrukce spršky z naměřených hodnot z pozemních detektorů. K tomuto účelu se používají Monte Carlo generátory. Největší vliv na výsledek simulace spršky mají hadronové modely, které jsou součástí generátoru interakcí. Pro nalezení Monte Carlo generátoru, který odpovídá reálné skutečnosti nejlépe, je nejvhodnější srovnání získaných dat z urychlovačů a jejich porovnání se simulacemi. Pomocí LHC urychlovače umístěného v CERN bude možno urychlit částice i ionizovana jádra na energie mnohem větší než na dnešních urychlovačích. ATLAS detektor představuje jeden z experimentů, pomocí něhož bude možno měřit rozdělení produkovaných částic a porovnávat je s generovanými daty. Toto srovnání přispěje k nalezení nejvhodnějšího simulátoru a k zpřesnění použitých parametrů.
Klíčová slova: Hadronové interakční modely, Monte Carlo generátory, minimum bias eventy, LHC, ATLAS.

Title: *Testing of Interaction Models of Cosmic Radiation at LHC Collider*
Author: *Petr Nečesal*
Department: *Institute of Particle and Nuclear Physics*
Supervisor: *Dr. Jan Řídký*
Supervisor's e-mail address: *ridky@fzu.cz*

Abstract: Cosmic radiation contains very energetic particles and nuclei, which cause extensive air showers. Detection of extensive showers induced by primary particle with energy higher than approximately 10^5 GeV is performed by means of ground detectors. Properties of primary particles (energy, mass) are determined according to reconstruction of the shower from values measured by ground detectors. Monte Carlo generators are used for these purposes. Hadronic models contained in generators most influence the results of shower simulations. Comparison of reached data from accelerators with simulations is the most suitable way for finding generator, which is closely to the real situation. LHC accelerator being builded at CERN will be able to accelerate particles even ionized nuclei to energy, which will be much more than energy reached by nowadays accelerators. ATLAS detector represents one of experiments, which will be suitable to measure distributions of produced particles and to comparison them with generator data. This comparison will contribute to find the most suitable generator and to its improvement.
Keywords: Hadronic interaction models, Monte Carlo generators, minimum bias events, LHC, ATLAS.

Chapter 1

Introduction

Monte Carlo event generators are very helpful and necessary instrumentations for all high energy experiments. They are used to simulate interactions to design properly detectors according to particular needs of individual experiments. Monte Carlo (MC) simulators help to optimize detectors before construction and therefore play an irreplaceable role in High Energy Physics (HEP).

Simultaneously the interpretation of extensive air shower (EAS) measurements depends on results and comparisons with EAS simulations. Energy reached at present day colliders is much smaller than energy of EAS. Therefore MC generators represent the only way how to construe measured data. The most important problem and the biggest challenge is to extrapolate accelerator data to ultra-high energies ($\simeq 10^{20}$ eV) encountered in Cosmic Ray (CR) physics.

Particles and nuclei coming from the universe (so called cosmic rays) turn out to have energy up to 10^{11} GeV. The energy spectrum of cosmic rays is steeply falling. It can be described by means of a power law in energy with index -2.7. At about $4 \cdot 10^6$ GeV (so called *knee*) the index changes to -3.1 (see Fig. 1.1) [1, 2]. The steepening of the spectrum seems to give additional information about particle sources. The sharp edge indicates the end of one energy spectrum. Some experimental data predict that CR energy spectrum start to rise up again in the energy beyond 10^{19} GeV (see Fig. 1.1). The decrease and following rising up of the total energy spectrum can be interpreted as a sum of particular energy spectra. Particles with energy below the *knee* are considered to be predominantly from our Galaxy. It is assumed that energy above the *knee* belongs to end of spectrum of galactic particles and emerging spectrum of extragalactic particles. Cosmic ray spectrum has two distinct regions. The second one, so called *ankle* is beyond 10^{19} GeV. This area is not properly explored, however, it is of essential interest because of possible upper limit of particle energy. This cut-off is called the Greisen-Zatsepin-Kuzmin (GZK) limit [3, 4] and it refers to interaction of cosmic rays (with sufficient energy) with background radiation.

Energy and other properties of cosmic rays can be measured directly (for example by detectors carried by balloons or by satellites), however only up to energy of about 10^5 GeV. Beyond this limit data have to be collected by ground detectors of EAS.

These experiments are based on measurement of the air showers induced in the atmosphere. Cosmic rays are rare at higher energies according to flux, therefore long time exposure and large detector sizes are needed. This is necessary to detect sufficient amount of events.

The description of interactions of hadronic particles in the showers with the nuclei in the atmosphere is the most crucial aspect of simulations. Therefore the reliability is indispensable. However, hadronic interactions are still inaccurately described in EAS energy regions. Interaction models have to provide results in accordance with data acquired at colliders. Nowadays the highest energy (2 TeV in center of mass) is accessible at collider Tevatron in Fermilab. This energy corresponds to $2 \cdot 10^3$ TeV in $p\bar{p}$ laboratory system. The laboratory system is the natural system for description of EAS. To perform successful comparison, detector has to cover very forward regions for particles with small transverse momenta and high energies. These events dominate in the development in EAS. Full coverage detectors are technically demanding and area along beam pipe is not covered at colliders.

Testing and checking the credibility of hadronic interaction models is crucial for cosmic rays physics. By measuring so called minimum bias events in the very forward area this can be done. Minimum bias events are usual, common and the most frequent ones. These interactions could be characterized by low-$p_\perp$ parton scatterings (see A.6), because high-$p_\perp$ scatterings are rare. In various texts different definitions of minimum bias events can be found. Sometimes they are described like non-single diffractive interactions. Minimum bias events are closely connected to EAS events, because they represent the vast majority of detected events.

New opportunities appear at Large Hadron Collider (LHC) at CERN. The aim of the presented work is to study particle production in conditions of the ATLAS detector at LHC. It offers better conditions to study event generators as the energy 14 TeV in the Center of Mass System (*CMS*) of proton-proton collisions corresponds already to the 'knee' region. Capabilities of ATLAS detector are enormous and therefore they could be utilized in nucleus-nucleus and proton-nucleus interactions relevant to cosmic rays studies [6]. Except ATLAS, there are 3 other LHC experiments under construction: CMS, ALICE, LHCb. They also bring opportunities for nuclear physics, especially the experiment ALICE is dedicated for nuclear physics program, but these detectors do not belong to the subject of this thesis.

The most obvious variables to test particle production at LHC are multiplicity, transverse momentum and energy distribution of secondary particles produced, rapidity and pseudorapidity distribution (definitions of all variables can be found in Appendix A). Pseudorapidity is the approximation of rapidity for the case that particle velocity is $\beta = 1$ or the mass of particle is $m = 0$. On the other hand pseudorapidity can be measured even in the case, when the energy and momentum of a particle are not known.

Interactions of cosmic rays in the atmosphere involve proton-nucleus and nucleus-nucleus collisions. They differ from nucleon-nucleon interactions in many aspects and mechanisms which one has to consider. The complexity of the field brings new
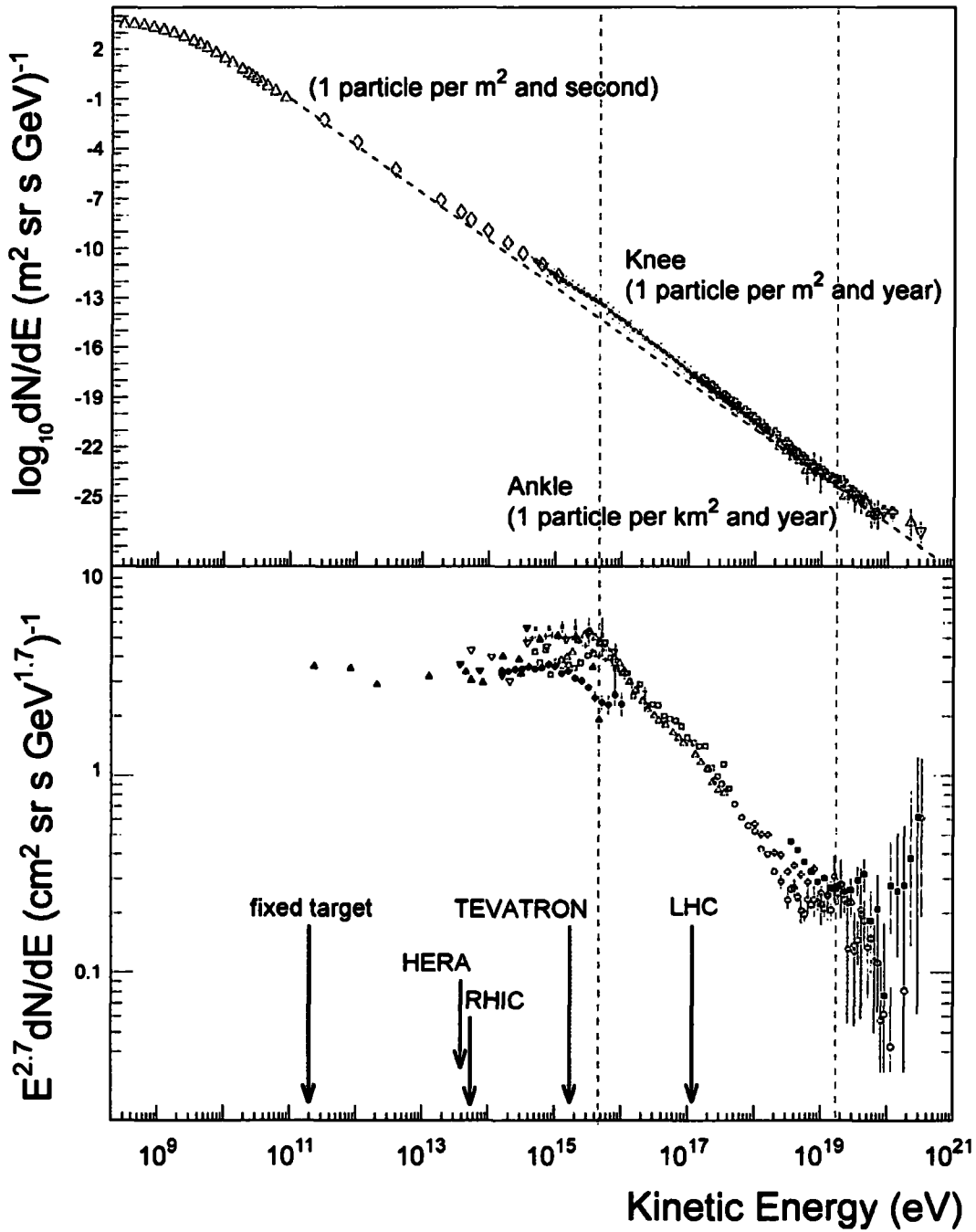
Figure 1.1: The cosmic ray energy spectrum. Dashed lines mark regions usually called 'knee' and 'ankle'. Red arrows indicate energies achieved by various collider experiments and blue arrow specifies energy achievable in fix target experiments. Taken from [5] and modified.

issues and questions to be answered. Heavy Ion Physics (HIP) is trying to obtain information about a new presumed phase of matter, the Quark Gluon Plasma (QGP). Quarks and gluons are no longer confined in this state and chiral symmetry is restored [7]. Even without this phase transition interaction models involving nuclei are far from being complete. Particles emitted in the very forward region bear most of the collision energy. Their kinematic parameters cannot be presently calculated by means of the field theory of strong interactions, the Quantum Chromodynamics (QCD), because of small momentum transfer. Theory can provide account of perturbative processes, but non-perturbative effects have to be included as well. Just size of incident nuclei implicates more frequent occurrence of these phenomena. Also the high density of produced particles can cause non-linear effects.

A plan of this work is to compare PYTHIA [8], QGSJET [9], HIJING [10] and QGSJET-II [11] at LHC energy region. PYTHIA is frequently used to simulate high energy collisions of elementary particles. For these interactions PYTHIA is considered to be the etalon. HIJING Monte Carlo generator achieves successes in generation of hadron-nucleus and nucleus-nucleus collisions. These achievements are connected to reproducing the data from RHIC accelerator more closely then other generators [12]. QGSJET is considered as the base for calculations at super-high energies of cosmic rays. It is in good accordance with the data and therefore QGSJET is thought to be a standard in CR physics. QGSJET-II is the new version of QGSJET written by the same author, which improved the generator by including new phenomena. However QGSJET-II has still the beta version status. The MC models are described and discussed in Chapter 2. It comprises also classification of models in general and more detailed descriptions of relevant models. The main goal is to find significant differences between these generators which could be seen in the ATLAS detector. Results from particular simulators are included in Chapter 3. At first, there are comparison of mentioned generators in proton-antiproton interactions corresponding to Tevatron energy, that is in the region where the real data have been already obtained. Detector response and capability to compare simulations with measurements depends on the ATLAS detector design and coverage of very forward regions, too. Description of the ATLAS detector and intended application for nuclear physics can be found in Chapter 4. Proton-nucleus and nucleus-nucleus interactions will be studied in this work. Differences of generators in such regions of kinematic variables, where it is possible to measure by detectors are discussed in Chapter 4. There are detectable regions with significant differences among simulators. On the base of such results and after performing relevant experiments at LHC and ATLAS one could decide which of these models is approaching the real situation the best. Chapter 5 contains conclusions and summary of this work. Variables and quantities used for description can be found in Appendix A.

Chapter 2

Monte Carlo Simulators

2.1 Review of Generators

Many interaction models are used to simulate and describe particles and nuclei collisions. They have to describe vast amount of phenomena. They also have to reproduce accelerator data and give as much details of interactions as possible. Therefore they contain perturbative QCD processes to take into account hard processes and also soft processes. Currently many models are used and they differ in implementation and how much they are inspired by QCD. According to this, models which are not so theoretically inspired contain more phenomenological parameters than others. Total multiplicity is most influenced by the underlying soft events. Properties of these events are quite model-dependent. Models of nuclei interactions are not so standardized in contrast with hadron-hadron ones. This could be accounted to higher complexity of relativistic nucleus-nucleus interactions. Especially non-perturbative effects which are dealt with by models, increase with the nuclear size. As a result, some non-linear effects in particle densities can be observed and are of much importance in nucleus-nucleus collisions. The time evolution of the heavy ion collisions is not described in such detail as in the case of hadron-hadron event generators [13]. Space-time framework is included implicitly or explicitly in models which aim to describe heavy ion collisions.

The interpretation of EAS (PeV region) depends strongly on hadronic interaction models. Many EAS experiments have used various models to determine the primary particle, its energy and consequently mass composition of cosmic rays. These tools of nuclear physics are needed to describe collision processes of the primary particles (hadrons or nuclei) with air nuclei by extrapolating to higher energies and small momentum transfers. Nuclear collisions cannot be described only as a sum of nucleon-nucleon interactions and such simplest models give wrong results. It means that some collective effects appear. On the other hand, elementary nucleon-nucleon interaction is taken as a basis. Different models are proposed under different theoretical assumptions. However, the use of the same physical model does not necessarily lead to the same results. Physical model describes the framework of interaction and

stages which partons go through. Consequently, observables depend not only on the particular model, but also on implementation of the physical ideas.

Results obtained from models of the hadronic interactions suffer from various uncertainties. Firstly, some of them are caused by necessary approximations implied in the model construction. Secondly, due to inconsistencies in the experimental results taken as a basis for extrapolations. These data also suffer from systematic uncertainties which are in consequence contained and amplified in the hadronic interaction models. For instance, nucleon-carbon cross sections have been obtained at energies 200–280 GeV as $\sigma_{inel} = 225 \pm 7\,mb$ [16] and $\sigma_{inel} = 237 \pm 2\,mb$ [17] with uncertainties mainly of systematic character. Total cross section of proton-antiproton collisions has been measured by different collaborations at Tevatron. At the highest energy of $\sqrt{s} = 1.8\,\text{TeV}$ total proton-antiproton cross section was determined as $\sigma_{tot} = 72.8 \pm 3.1\,\text{mb}$ [18], $\sigma_{tot} = 80.03 \pm 2.24\,\text{mb}$ [19], and $\sigma_{tot} = 71.71 \pm 2.02\,\text{mb}$ [20], respectively. The probability that values are consistent with each other is only 1.6 % [20]. On the account of such differences, uncertainties of 5–10 % are propagated when constructing hadron-air and nucleus-air cross sections for EAS simulations. Several interaction models have been developed for modeling EAS in program CORSIKA [21]. Simulations done with CORSIKA show that effects on predictions are substantial. For example in case of primary proton with 10^{14}–10^{15} eV an increase of hadron-air σ_{inel} by 10 % implies a decrease of the number of high-energy hadrons ($>$ 100 GeV) by up to 50 % and of the electron number ($>$ 300 MeV) by $\simeq$ 15 % [22]. These results are calculated for EAS of vertical incidence at sea level. Interpretations of EAS are affected by such errors. As an illustration, the mass composition of primary particles (at highest energies) is derived from the depth of shower maximum. As a result the composition varies from mixed to pure iron according to particular model. On the other hand, the strong dependence of the hadronic EAS observables on details of the interaction models gives opportunity to make comparisons and test the models. The conclusions lead to constraints of the model free parameters despite our limited understanding of the primary interactions.

Interaction models can be classified by different criteria. It is very difficult and delicate because they are almost mixed and division is therefore ambiguous due to different points of view. Models contain description of several stages of the collision. They involve elementary interactions between partons and strings and also for example evolution of hadrons. Heavy ion collision is divided into elementary interactions on several microscopic levels. Each stage refers to particular space scale and time scale of the collision. Models can be therefore characterized according to which stage is the mainly emphasized one and which assumptions for it are used [13]. Although most of them are mixed it is possible to classify them with dominant characteristics.

From other point of view, models can be classified according to whether they mainly pay attention to the *hard* or *soft* part of the collision, which is related to the value of transferred momentum in the interaction (more information about these concepts can be found at the beginning of the Subsec. 2.2.3).

Both of these classifications will be discussed in next Sec. with main representa-

Parton formation   Parton evolution   Hadron gas
Preequilibrium   Equilibrium, QGP   evolution
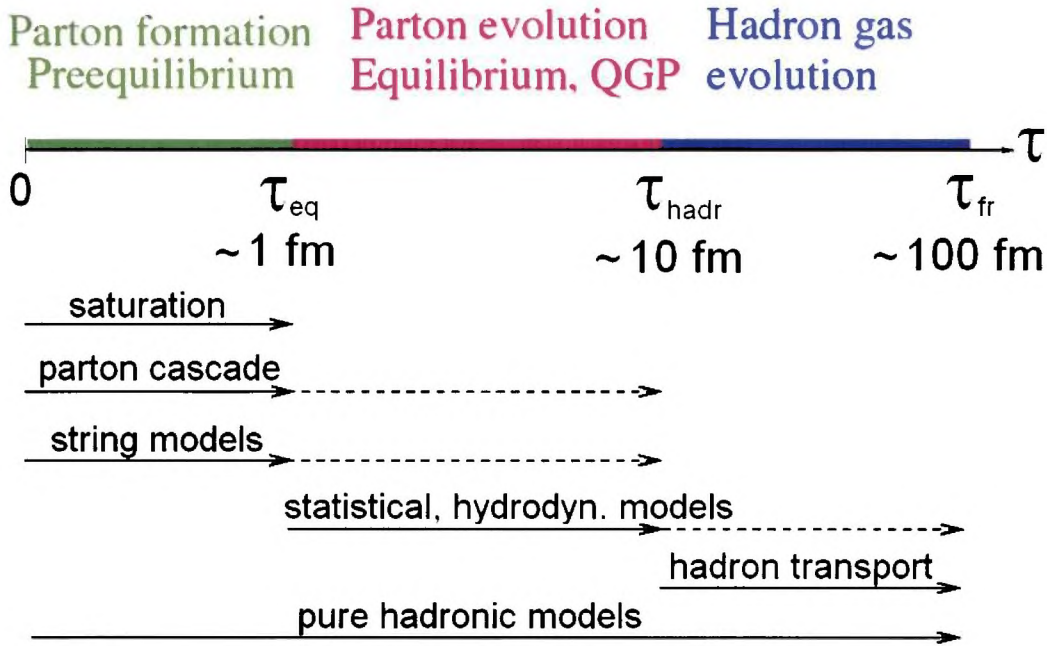
Figure 2.1: Schematic diagram of stages of a heavy ion collision. There are classes of models with their main emphasis on particular stages (solid lines). Dashed lines indicate extension of models to successive stages. The axis τ is a time scale indicating time after collision. Taken from [13] and modified.

tives of the models.

2.2 Classification of Models by Reaction Mechanism

As mentioned above, models can be divided into several groups according to stages, by which they pass through. Fig. 2.1 shows a sketch of the stages of heavy ion collision and corresponding classes of models which were proposed for them. Solid lines represent stages for which the models were originally designed. Dashed lines signify subsequent stages to which the models are extended. There is a time scale given in orders of magnitude.

Immediately after such a dense energy region is formed. After a short time of the order of τ_{eq} partons rescatter. That leads to thermalization of the system and to creating of equilibrium of quarks and gluons, which is called Quark Gluon Plasma (QGP). After τ_{eq} QGP evolves and cools down until it reaches the critical temperature.

Afterwards hadrons start to be created, this refers to the time τ_{hadr}. The next stage called *mixed phase* is composed of cooling down QGP and formation of hadrons. In Fig. 2.1 this stage is absent to simplify the situation. This stage ends in the point called *chemical freeze-out*, where hadrons are already formed and exchange of quarks and gluons is stopped. The system of hadrons is still interacting and therefore *hadron gas* is the convenient label. Interactions (scattering) of hadrons end at point of *thermodynamical freeze-out* corresponding to τ_{fr} time. Needless to say, division to individual stages is artificial and physically there are no borders, but it is helpful for Monte Carlo implementation and causality. In practise, the real stages overlap each other. There are some types of models which are trying to describe the initial stage, called *pre-equilibrium*, and how the system evolves to equilibrium. Parton cascade and string models belong to this group. It is necessary to remark, that no existing Monte Carlo simulator describes saturation stage. The mentioned models are built primarily to implement various ideas on the initial stage, however, to give an account of collision observables they are extended to successive stages after equilibration. Hydrodynamical or statistical models are describing the equilibrated partonic stage (QGP). The last stage is called hadronic phase and can be included. Hadronic transport models are intended for treatment of the hadronic phase. The whole history of a hadron collision is simulated by *pure hadronic models* (to avoid ambiguity with the concept of a *hadronic model* which consists of several parts to describe final stage of interaction).

2.2.1   Pure Hadronic Models

These models interpret and describe nuclear collisions as simple superposition of hadron-hadron collisions. They use Glauber-Gribov model and nuclear geometry to calculate the number of such collisions for a given impact parameter b. LUCIFER [23] and LEXUS [24] belong to this category. As mentioned above, this simplification of interactions fails as collective effects appear with increasing number of nucleon-nucleon collisions.

2.2.2   Parton Cascade Models

The Parton Cascade Model (PCM) [25] uses quarks and gluons as degrees of freedom for microscopic approach. The PCM is convenient tool to study hot and dense partonic stage QGP. It describes the dynamics of the pre-equilibrium deconfined reaction phase. There are several physical issues which are connected to this approach such as mechanisms of parton equilibration, the production of heavy quarks and the emission of photons and dileptons in the phase before equilibrium and the dynamics of energy loss in a deconfined medium.

The state of the dense partonic system in PCM is characterized by a set of one-particle distribution functions $F_i(x^\mu, p^\alpha)$, where $i = g, u, \bar{u}, d, \bar{d}, \ldots$ is the flavour index and functions depend on coordinates x^μ, p_α in the eight dimensional phase

space. These models solve a relativistic Boltzmann equation for partons:

$$p^\mu \frac{\partial}{\partial x^\mu} F_i(x, \vec{p}) = C_i[F] ,$$ (2.1)

with collision term C_i which is a nonlinear functional of the distribution function. Cross sections and splittings are calculated in perturbative Quantum Chromodynamics (pQCD) at lowest order (leading order). Partons propagate on-shell and along classical trajectories in phase space (according to the rules of the relativistic kinematics) between individual parton-parton interactions. The initial state is either constructed from experimentally measured nucleons and nuclei structure functions and elastic form factors or provided by a model of the initial state of collisions. AMPT [26] and GROMIT [27] represent Monte Carlo codes of PCMs which use partons produced in initial parton-parton collision provided by HIJING (see Sec. 3.1.1) as initial condition to generate parton distribution. VNI [28] and VNI/BMS [29] take initial conditions from parton distribution functions from measured data. Initial and final state radiation is included.

2.2.3   String Models

Before discussion of string models it is necessary to introduce essential concepts of *soft* and *hard* interactions. *Hard* interaction is characterized by large momentum transfer and can be therefore dealt by pQCD. On the other hand, *soft* interaction is a notion for small momentum transfer processes. Distribution of transverse momenta $p_\perp$ (A.6) of secondary particles is convenient for distinction of hard and soft interactions. Such

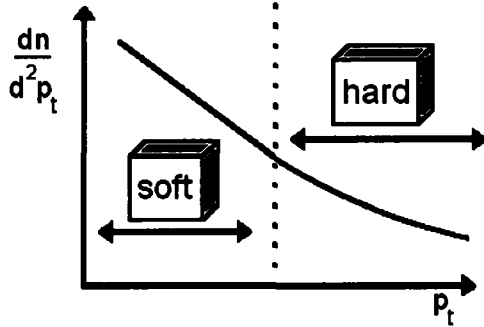Figure 2.2: Transverse momentum distribution separating soft and hard scattering. Taken from [30] and modified.

a distribution is actually different for both types of interactions (scatterings). For instance pion $p_\perp$ spectra for $p_\perp < 2\,\mathrm{GeV}$ behave exponentially in contrast to large-$p_\perp$ part of spectra with a power law distribution [30]. A rough scheme of such $p_\perp$
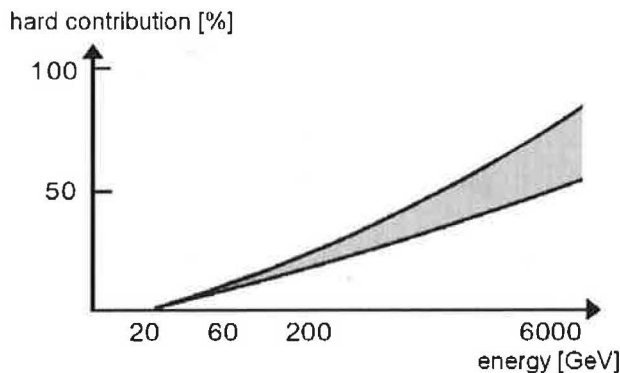
Figure 2.3: Ratio of hard scatterings versus center of mass energy. Taken from [30] and modified.

distribution is in Fig. 2.2 with logarithmic scale on y-axis. The exponential low-$p_\perp$ part is due to soft processes, whereas dependence of the form $p_\perp^{-m}$ corresponds to hard processes, which can be described by QCD diagrams. A ratio of soft and hard interactions (actually a ratio of hard and soft cross sections) depends on energy of interaction. With increasing energy of the collision hard interactions begin to appear and then become preponderant over the soft ones. Fig. 2.3 demonstrates contribution of hard interactions in dependence on the energy. It shows that at energy region of about 7 TeV (energy available at future LHC collider, see Chapter 4) hard scattering will be of the crucial importance, whereas at energy up to ~20 GeV hard interactions do not emerge.

String models describe collisions via exchanges of colour and momentum between partons in the target and projectile. Partons become connected by objects called strings, ropes or flux tubes. Many models can be assigned into this group, e.g. HIJING (see 3.1.1), QGSM [31], PSM [32], DPMJET (Monte Carlo implementation of Dual Parton Model) [33], NEXUS [34], LUCIAE [35], VENUS [36], FRITIOF [37] or SFM [38].

String models are models providing description of soft low-$p_\perp$ hadronic and nuclear interactions up to moderately high energy (< 100 GeV). There are string models based on Gribov-Regge Theory (GRT) [36] and even more phenomenological models. GRT string models are within the framework of relativistic quantum theory, compatible with QCD, and they will be discussed later. In spite of theoretical approach of GRT, this theory can be also considered to be phenomenological one in the sense that many assumptions are introduced to provide a link with QCD. The basis of Gribov-Regge theory of multiple Pomeron exchange are Reggeons and Pomerons [36]. The Pomeron is an elementary exchange object, but it is not elementary in terms of quarks and gluons. Data suggest that at high energy Pomerons turn out to be dominant, whereas high energy scattering in leading log approximation is dominated by gluon

pomeron amplitude   "cut cylinder"
(sum of QCD diagrams)

Figure 2.4: Imaginary part of Pomeron amplitude is proportional to square of sum of all cut cylindrical diagrams (gluons and closed quark loops on a cut cylinder surface. Pomeron amplitude on the left side is illustrated as zigzag line. Taken from [30].

ladders [36]. Therefore according to Veneziano, Pomeron is identified with the sum of all QCD cylindrical diagrams (cylinder of gluons and quark loops fitting on a surface, see Fig. 2.4). Reggeons are connected to planar diagrams, also by means of the sum of all planar diagrams. On the other hand, only Pomerons can be considered as exchange object, because high energy scattering is dominated by them.

In the simplest case of one Reggeon there is connection of the Reggeon amplitude and squared cut plane. The Reggeon amplitude is given by one-Reggeon exchange. Some well known facts about planar QCD diagrams have to be considered. Especially, that planar diagrams have similar properties as compared to fragmentation of strings. In the case of one Pomeron, a squared cut cylinder refers to imaginary part of the Pomeron amplitude and corresponds to two fragmenting relativistic strings (see Fig. 2.4). Dynamics and fragmentation of strings are the essential parts of models. Relativistic string is a two-dimensional surface in a four-dimensional Minkowski space. It is object with mass and behaviour in accordance with equations of motion derived from Hamilton principle. In the colour string models the string can be considered as a flux tube connecting two colour charges. The homogeneous colour field induces production of pairs of coloured partons. It causes the neutralization of colour field and simultaneously creation of two substrings. Successive decays may occur in the similar way. (In [36] comprehensive information about strings and fragmentation can be found.)

In this framework, for instance interaction of two incident hadrons $\tilde{f}_1$ and $\tilde{f}_2$ via exchange of colour between two partons i and j results in two strings. Endpoints of one string are $\tilde{f}_1 - i$ and j, endpoints of the second string are $\tilde{f}_2 - j$ and i. Using symbols $\{\cdots | \cdots\}$ for strings, with $\tilde{p}_1, \tilde{p}_2, k, l$ being the incident hadron momenta and parton momenta, respectively, the interaction can be written as

$$\tilde{f}_1\left(\tilde{p}_1\right) + \tilde{f}_2\left(\tilde{p}_2\right) \longrightarrow \{\tilde{f}_1\left(\tilde{p}_1\right) - i\left(k\right) | j\left(l\right)\} + \{\tilde{f}_2\left(\tilde{p}_2\right) - j\left(l\right) | i\left(k\right)\} \qquad (2.2)$$

It seems to be very useful to introduce quark line diagrams to keep track of flavour flow (see Fig. 2.5 for graphical demonstration of Eq.. 2.2). Fig. 2.5 represents single colour exchange, i.e. nondiffractive scattering. Quarks are represented by horizontal lines. Vertical lines indicate strings which link quarks together. Quarks are depicted by dots. Intersections of strings and quarks lines without dots have no meaning. The colour exchange is represented by an arrow between two quark lines. Initial (or intermediate) configurations of quarks can be indicated by empty dots, in the final stage of strings, quarks are plotted by full dots. Incident hadrons $\tilde{f}_1$ and $\tilde{f}_2$ are colour singlets and the final products - partons linked together: $\tilde{f}_1 - i$ with j and also $\tilde{f}_2 - j$ with i are singlets. It is the reason for term *colour exchange* between partons i and j. One has to keep in mind that quarks in Fig. 2.5 correspond to the so called *constituent quarks*. There is non-zero probability of colour exchange involving $q - \bar{q}$ pair from so called *sea* (virtual pairs of parton-antiparton). Resulting diagrams with colour exchange regarding sea quarks correspond to diffractive excitations of projectile or target or both. As a consequence, there are four types of colour exchange between quarks: nondiffractive, diffractive excitation of initial particles and double diffractive excitation (so called *Pomeron-Pomeron scattering*). For antiquark colour exchange the situation is rather different. The diquarks in Fig. 2.5 have to be replaced by four quarks to keep singlet character while other relations hold. The single colour exchange can be generalized to multiple colour exchange. Also generalization to nucleus-nucleus interactions can be done. A simple example of quark line diagram for nucleus-nucleus collision is shown in Fig. 2.6 with the same rules as written above.

Strings generated by colour exchanges undergo fragmentation process in the framework of classical relativistic string theory. Strings break up in such way, that decay products can be either again strings or particles depending on the masses of the strings. Several string fragmentation models are used, e.g. Lund model JETSET [39] and AMOR [36]. Model AMOR is covariant and also gauge invariant. Lund fragmentation model conserves both energy and momentum via connection partons by a colour field. It considers also two partons and by means of fragmentation step new hadron is formed which contains one of the partons. AMOR model is based on string decay into two substrings (of arbitrary masses), whereas in the Lund model string decays into string and hadron (of specific mass). That is an iterative mechanism limited by masses of the strings (some cut-off). They split while their masses are above some cut-off in both models. Below this limit, strings become stable hadrons or resonances. The Lund model JETSET uses the framework of classical relativistic strings, it conserves energy and momentum and JETSET is also covariant model.

So far *independent string models* were discussed. This type of models considers an independent fragmentation of each string. Higher energy of collision, degree of centrality and larger size of nuclei implicate larger amount of strings. It is supposed this leads to interaction among strings at very high energy heavy ion collisions. These processes can be seen as connection or alternative to *nuclear shadowing effect* leading to reduction in multiplicities at central rapidity regions [15]. *Shadowing effect* causes shielding of interactions of participants. Because of large size of nuclei, nucleons can
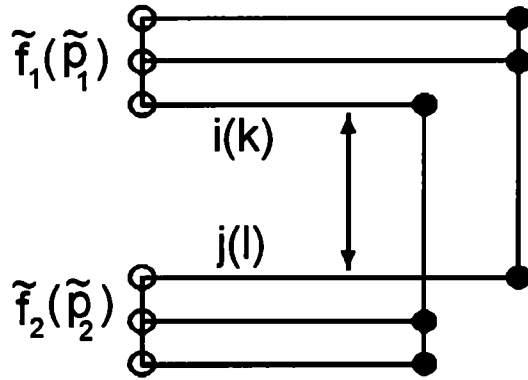
Figure 2.5: Quark line diagram. Colour exchange between partons i and j corresponding to a nondiffractive scattering. Taken from [30] and modified.
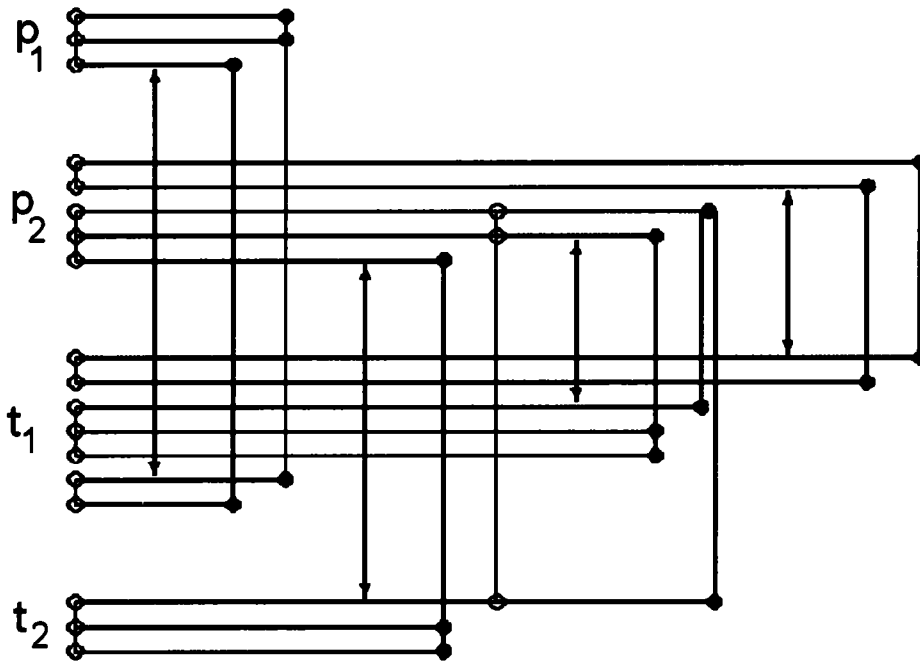

Figure 2.6: Quark line diagram for a nuclear collision. p_1 and p_2 are the projectile hadrons, whereas t_1 and t_2 are the target hadrons. Taken from [30] and modified.

not interact with those which are shadowed. There are limitations of *independent string model* approach corresponding to *high energy limit*, *low energy limit* and *high density limit*.

The *low energy limit* is an implication of *Gribov-Regge formalism*. It is based on asymptotic considerations for center of mass energy (see A.3) $s/\text{GeV} \gg 1$ and it forms an essence of string model. There are other arguments for such energy limitation from below. Consider nucleon-nucleus interaction. String models admit several interactions of hadron while passing through the nucleus. After the first interaction strings are created. One of the ends of each string can be denoted as *leading* (in fact parton) which is the most energetic. It traverses the whole nucleus and does not form hadrons, but does interact whenever target nucleon is close enough. This concept needs enough energy that restricts energy range of string model. The *hadronization time* for forming hadrons has to be larger than the *traversal time* necessary for projectile nucleon to traverse the nucleus. It leads to minimum center of mass energy [30]:

$$\sqrt{s_{\min}} \approx 5\,\text{GeV}\,. \tag{2.3}$$

The *high energy limit* is related to new phenomena turning up at high energy nucleon-nucleon scattering. At energies beyond 100 GeV in center of mass a bunch of secondary particles going in almost the same direction comes into view. This bunch is called *jet*. By means of evaluating elementary QCD diagrams the inclusive cross section σ_{jet} for jet production can be calculated. According to [40] $\sigma_{jet} = 0$ mb up to $\sqrt{s} \approx 30$ GeV. Between 30 GeV and 100 GeV σ_{jet} increases slowly up to 5 mb. Then it rises quickly with energy to $\sigma_{jet} \approx 40$ mb around 10^3 GeV. Comparison of σ_{jet} with the total cross section of *p-p* interaction σ_{tot} indicates concerment of the hard processes. $\sigma_{tot} \approx 40$ mb at $\sqrt{s} = 30$ GeV, $\sigma_{tot} \approx 45$ mb at $\sqrt{s} = 100$ GeV and $\sigma_{tot} \approx 70$ mb at $\sqrt{s} = 10^3$ GeV [41]. The string model as model for soft interaction has therefore the upper energy limit at:

$$\sqrt{s_{\max}} \approx 30 - 100\,\text{GeV}\,. \tag{2.4}$$

To include high energies in the string model also hard processes have to be dealt with. This can be done by standard pQCD calculation. Its basis is hard scattering, where inclusive jet cross section σ_{jet}^{ac} for production of parton jet pairs from hadrons A and B in the sense of parton model can be written according to:

$$\sigma_{jet}^{AB} = \sum_{i,j=q,\bar{q},g} \int dx_1 \int dx_2 \int_{p_\perp^2 > Q_0^2} dp_\perp^2\, f_i^A\left(x_1, Q^2\right) f_j^B\left(x_2, Q^2\right) \frac{d\hat{\sigma}_{ij}}{dp_\perp^2}\,, \tag{2.5}$$

where $f_i^A\left(x_1, Q^2\right)$ and $f_j^B\left(x_2, Q^2\right)$ are momentum distribution functions of partons i and j in hadron A and B, when probed at virtuality scale Q^2. Therefore, $\frac{d\hat{\sigma}_{ij}}{dp_\perp^2}$ is the differential cross section of partons i and j (see Fig. 2.7 on the left). This quantity represents the elementary cross section, calculated from sum of QCD diagrams at the lowest order. To preserve convergence and to be computable in framework of
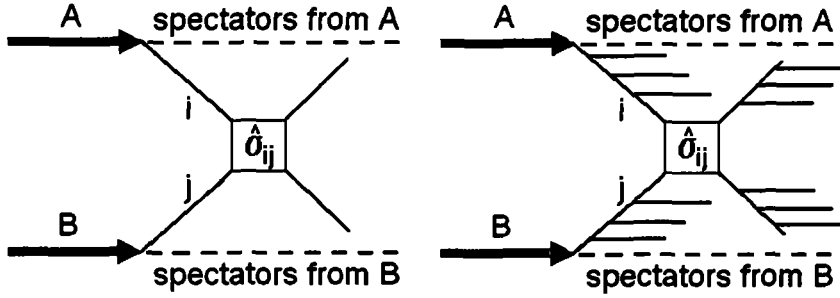
Figure 2.7: QCD scheme: Hard scattering of partons i and j from nucleons A and B (left picture) and additional initial and final state radiation of partons i and j (right picture).

pQCD it is necessary to integrate Eq. 2.5 with a low $p_\perp$ cut-off parameter Q_0. In the following, f_i represents a fundamental fermion of flavour i, i.e. d, u, s, c, b, t, e^-, ν_e, μ^-, ν_μ, τ^-, ν_τ. $\bar{f}_i$ denotes corresponding antifermion. Quarks, antiquarks and gluons are explicitly denoted as q, $\bar{q}$ and g, respectively. Left Fig. 2.7 is an example of $2 \rightarrow 2$ QCD interactions which include following processes:

$$q_i q_j \rightarrow q_i q_j, \quad q_i \bar{q}_i \rightarrow q_k \bar{q}_k, \quad q_i \bar{q}_i \rightarrow gg, \quad f_i g \rightarrow f_i g, \quad gg \rightarrow f_k \bar{f}_k, \quad gg \rightarrow gg. \qquad (2.6)$$

Models also encompass processes with *initial and final state radiation*, in which parton with a squared mass Q^2 radiates another parton before hard scattering (or after hard scattering) and the latter one carries part of initial Q^2. This process can be repeated in the same way (see Fig. 2.7 on the right).

Partons i and j in Eq. 2.5 participate in the high $p_\perp$ jet production and originate from partonic cascades in hadrons A and B, being emitted by parent partons of smaller $p_\perp$ and larger energy, those in turn being emitted by their own parents and so on. The whole described process is usually called *parton ladder*. It appears mandatory to consider multiple jet production processes, in other words, to describe the interaction as multiple exchange of parton ladders (see Fig. 2.8). Inelastic cross
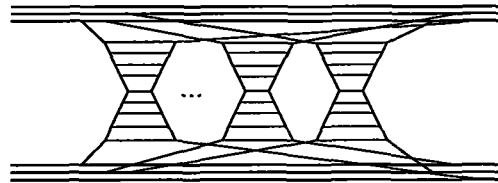

Figure 2.8: Hadron-hadron scattering, which is represented by multiple exchange of parton ladders, taken from [42].

sections can be written in the same *eikonal form* for soft and even hard multiple

scattering as derived from multiple colour exchanges and multiple jet production (see [30]).

$$\sigma_{inel,i} = \int d^2b \left[1 - \exp^{-2\chi_i\left(b^2,s\right)}\right] , \qquad (2.7)$$

where $i = s, h$ for *soft* and *hard* case, $\chi_i\left(b^2, s\right)$ is the so called *eikonal* for soft or hard scattering depending on impact parameter b and energy s. Eikonals can be expressed in term of cross sections and function dependent on b:

$$\chi_h\left(b^2, s\right) = \frac{1}{2}\sigma_{jet}(s) \, T_{NN}(b) , \qquad (2.8)$$

$$\chi_s\left(b^2, s\right) = \frac{1}{2}\sigma_{soft}(s) \, T_{NN}(b) , \qquad (2.9)$$

with hadronic overlap function

$$T_{NN}(b) = \int d^2b' \, T_N\left(b - b'\right) \, T_N\left(b'\right) , \qquad (2.10)$$

where $T_N = \int dz \, \rho_N\left(z, b\right)$ is the nucleon profile function, ρ_N is a nucleon density. For $b = 0$ fm $T_{NN}(b)$ represents complete overlap of nucleon functions and it is largest. If b is equal to $2R_{nucleon}$, $T_{NN}(b)$ is smallest and it occurs in the case of touching nucleons. In Eq. 2.9 soft interactions are represented by inclusive soft cross section σ_{soft} to get similar terms, but it is determined only phenomenologically, in contrast to σ_{jet}. With conventional structure functions and above mentioned low $p_\perp$ cut-off parameter Q_0 the inclusive jet cross section σ_{jet} is calculated by means of pQCD. To include hard and soft interactions, total eikonal divides into soft and hard part:

$$\chi\left(b^2, s\right) = \chi_s\left(b^2, s\right) + \chi_h\left(b^2, s\right) . \qquad (2.11)$$

Then the total inelastic cross section σ_{inel} is expressed similar to Eq.. 2.7:

$$\sigma_{inel} = \int d^2b \left[1 - \exp^{-2\chi\left(b^2,s\right)}\right] , \qquad (2.12)$$

where $\chi_i\left(b^2, s\right)$ was replaced by the total eikonal $\chi\left(b^2, s\right)$. Similarly, it is possible to express the elastic σ_{el} and total cross section σ_{tot} of nucleon-nucleon interaction:

$$\sigma_{el} = \int d^2b \left[1 - \exp^{-\chi\left(b^2,s\right)}\right]^2 , \qquad (2.13)$$

$$\sigma_{tot} = 2 \int d^2b \left[1 - \exp^{-\chi\left(b^2,s\right)}\right] . \qquad (2.14)$$

Unitarity of the cross section is included in the Eq. 2.12, which is obvious after expansion:

$$\sigma_{inel} = \int d^2b \sum_{c_s+c_h \geq 1} \sigma\left(c_s, c_h, b^2, s\right) , \qquad (2.15)$$

with the sum running over c_s soft elementary interactions and c_h hard elementary interactions. An insight how to obtain Eq. 2.12 is demonstrated below. We introduce the average number of hard scatterings $\bar{n}$ as

$$\bar{n} = \sigma_{jet} T_{NN}(b).$$ (2.16)

with the same meaning of $T_{NN}(b)$ as introduced above for two nucleons. Under assumption of independent multiple scattering, the probability $\epsilon_n(b)$ of n hard scatterings (multiple jet production) is given as a Poissonian with parameter b:

$$\epsilon_n(b) = \frac{(\sigma_{jet} T_{NN}(b))^n}{n!} \exp^{-\sigma_{jet} T_{NN}(b)} \quad j \geq 1.$$ (2.17)

Considering σ_{soft} in a similar way, the probability $\epsilon_0(b)$ of soft interactions without any hard ones is determined by:

$$\epsilon_0(b) = \left(1 - \exp^{-\sigma_{soft} T_{NN}(b)}\right) \exp^{-\sigma_{jet} T_{NN}(b)}.$$ (2.18)

The latter Eq. is composed of product of two terms, where

$$\left(1 - \exp^{-\sigma_{soft} T_{NN}(b)}\right) = \sum_{n=1}^{\infty} \frac{(\sigma_{soft} T_{NN}(b))^n}{n!} \exp^{-\sigma_{soft} T_{NN}(b)}$$ (2.19)

represents the probability of all possible 'pure' soft interactions and expression $\exp^{-\sigma_{jet} T_{NN}(b)}$ corresponds to the probability of no hard process. The inelastic cross section is therefore given by summing over n of probability $\epsilon_n(b)$ and integrating over b.

$$\sigma_{inel} = \int d^2 b \sum_{j=0}^{\infty} \epsilon_n(b)$$

$$= \int d^2 b \left(1 - \exp^{-(\sigma_{soft} + \sigma_{jet}) T_{NN}(b)}\right),$$ (2.20)

which is the equation 2.12 with convention 2.8, 2.9 and 2.11.

When the density of produced hadrons is too large (*the high density limit*), the independent string model is insufficient and fails. One of the possibilities to solve this issue is *string fusion*. It considers interactions between strings before hadrons are formed. Strings fuse as soon as their transverse position is close enough, in the interaction area. In particular, the fusion possibility is determined by the parton-parton cross section in practical Monte Carlo implementation. Properties of new strings arise from ancestor strings, namely from colour and flavour characteristics in accordance with the SU(3) colour composition laws and composition of flavour. Strings fusion leads to an enhancement of baryon and antibaryon production and also to heavy flavour enhancement. In nucleus-nucleus collisions particles outside the nucleon-nucleon kinematic region are produced. This so called *cumulative effect* is caused by the fact, that the resulting fused string has an energy-momentum equal to

the sum of the energy-momenta of its ancestors. It can exceed the energy-momentum achievable from isolated nucleon-nucleon collision. But the most important effect of string fusion is suppression of total multiplicities. Pions at central rapidity region are reduced, but rapidity distributions rise up at fragmentation regions. SFM [38] is an example of the string fusion model.

Beside mentioned string models at the beginning of this Subsec. there are transport models like RQMD [43], UrQMD [44], HSD [45] using strings as initial conditions for subsequent calculations (see 2.2.5). Strings are also employed for fragmentation stage of collision in many models. Some models deal with high-colour fields and also string fusion (HIJING, LUCIAE, DPMJET, RQMD). It is worthwhile to note, that string models have been primarily intended for hadron-hadron interactions, its generalization to hadron-nucleus and nucleus-nucleus was done through Glauber-Gribov approach. In this theory nucleus-nucleus scattering amplitude is defined by the sum of contributions of diagrams, corresponding to multiple elementary scattering processes between parton constituents of projectile and target nucleons.

2.2.4   Thermodynamical and statistical models

A basic hypothesis of the statistical and thermodynamical models is the assumption that local thermodynamical equilibrium is achieved at a partonic level. Statistical models consider that the system is a grand canonical ensemble with a temperature T and a chemical potential μ_B as free parameters. From results of the model which was able to reproduce data from e.g. SPS central Pb-Pb events, the boundary between QGP and the hadron gas can be studied. Especially temperature of so called *chemical freeze-out*. It corresponds to the time τ_{cf} after collision when hadrons stop exchanging quarks and hadron gas is formed as written above. Equilibrium QGP evolves in these models and some of them emphasize the phase transition to hadrons linked to hadronic transport (e.g. UrQMD, see Subsec. 2.2.5). Some models consider an initial condition given by HIJING.

2.2.5   Hadron transport models

These models solve relativistic Boltzmann equation (Eq. 2.1) for hadrons in the last stage of the collision after hadronization. AMPT, RQMD, UrQMD and HSD belong to this type. Such models have to imply huge variety of hadron species and of cross sections. High energy inelastic hadron-hadron collisions are usually described by string model, for example HSD uses FRITIOF string model (including PYTHIA). Low energy interactions are simulated according to experimental cross sections. And for example AMPT uses A Relativistic Transport Model for Hadrons (ART) for treating hadronic scatterings after hadronization. In addition, simple models for rescattering of secondary particles have been introduced in LUCIAE, DPMJET and PSM.

2.3   Classification of Models by Kinematics

In the previous Sec. one possible division of models has been outlined. As written above, there is not only the one way how to classify the models. They can be looked at by *hardness* of interaction, and accordingly they are classified into groups with main emphasis on *hard* of *soft* part of the interaction. Beside these two groups the third category comprises statistical and thermodynamical models with main predictions oriented to ratios between different kinds of particles, not to absolute multiplicities. These models have been discussed in Sec. 2.2.4.

Regarding models focusing on hard processes there are PYTHIA, ISAJET [46], HIJING, HERWIG [47], COJETS/WIZJET [48], EUROJET [49]. They calculate the cross section perturbatively, using the QCD improved parton model. They use some cut-off parameter $p_{\perp 0} \approx 1 - 2\,\mathrm{GeV}$ to compute perturbatively the number of minijets or partons with transverse momentum above this limit. Such calculations of events with large $p_{\perp}$ processes have been introduced in the string model Subsec. as a way to include hard part of an interaction (see Subsec. 2.2.3). Partons arising from the hard collision are used for subsequent evolution and hadronization. On the other hand models imply also a soft interaction part extracted for example from accelerator data.

DPM (DPMJET as Monte Carlo implementation), QGSM, VENUS, SFM, RQMD, UrQMD, FRITIOF, NEXUS and LUCIAE rank among models putting emphasis on soft part of the collision. Although they stress the soft/semihard interactions, the hard part is also included. The jet cross section is added to the elementary soft cross section as contribution to the *eikonalized* part. The perturbatively calculated cross section (2.5) is inclusive cross section and at high energies it exceeds the inelastic cross section and total cross section. For this purposes it is necessary to consider multiple scattering approach so that the unitary is not violated. The most naive idea, that σ_{tot} is a simple sum of σ_{jet} and σ_{soft} is wrong. Multiple scattering turns up according to a Poissonian distribution. The average number of scattering is proportional to the mentioned inclusive cross section and some profile function, therefore it is dependent on impact parameter b (see Subsec. 2.2.3).

A common approach how to combine soft and semihard scattering stems from the fact, that at high energies the amplitude can be written by means of mentioned *eikonal* [36]. It is divided into hard and soft part which ensures unitarity. The experimental data are necessary to find out information about eikonals. Such approach to hard and soft components of amplitude contributions is used in many models. E.g. DPM is based on Pomeron exchange and there are two types of Pomerons, soft and hard Pomerons, which contribute to amplitudes. The total and inelastic cross sections are provided by the sum of amplitudes corresponding to particular numbers of soft and hard Pomerons. This approach represents a microscopic model and the idea of two types of Pomerons is in fact phenomenological eikonal ansatz.

Chapter 3

Tested Models

3.1 The Heavy-Ion Jet Interaction Generator - HIJING

3.1.1 The Description of HIJING

HIJING is a Monte Carlo Program based on pQCD to study jets and associated particle production in proton-proton, proton-nucleus and nucleus-nucleus interactions. This generator uses physical principles and approaches of multiple *minijet* production, soft interaction, nuclear shadowing of parton distribution functions and jet interaction in dense matter. As written in Subsec. 2.2.3 jets emerge in hard parton scattering. Jets played an important role in $p\bar{p}$ collisions at CERN Sp$\bar{p}$S and Fermilab Tevatron energies. Jets can be identified experimentally as hadronic clusters in solid angle with sufficient transverse energy $E_\perp$ (see A.7). It is necessary to distinguish jets from underlying background and to reconstruct them from detector data, because in such cases $E_\perp$ is usually greater than usually several GeV, jets can be reconstructed from calorimeter study. But if the transverse energy of jets are smaller, it is more difficult to identify jets from background, however, it is expected that hard parton scattering continues to the regions of lower transverse momenta. *Minijets* are jets, which can not be experimentally resolved due to small transverse energy, but corresponding parton scattering can be still calculable by means of pQCD. Minijets play a significant role in high energy interactions of heavy ions, 50 % of the *transverse energy* is associated to minijets at RHIC energies and even more (about 80 %) is expected at LHC energies. Transverse energy $E_\perp$ for instance of a jet is given by the total energy E of a jet and by the angle θ between the beam direction and the jet as $E_\perp = E \sin(\theta)$. Therefore minijets will dominate the central rapidity region. It is very important to calculate these background processes in order to study QGP, because minijets cause correlations between some observables which could be signatures of QGP.

HIJING is a Monte Carlo program designed to study collisions in wide range of

initial conditions. This generator provides an opportunity for theoretical studies of jets, *jet quenching* and nuclear effects. *Jet quenching* is a process where partons lose energy as they pass through the dense matter. High energy partons which would create a jet dissipate some part of their energy among other partons produced in the collision. Jet quenching is included in the generator and it is modelled by means of an effective energy loss parameter dE/dx. It enables to study the dependence of moderate and high $p_\perp$ observables on the model parameter — energy loss per unit length dE/dx. Jet quenching causes a moderate enhancement of particle production in the central rapidity region and reduction of yield in the forward regions [15] In pp and $p\bar{p}$ interactions HIJING attempts to cover the whole spectrum of possible parton interactions from low $p_\perp$ non-perturbative processes to hard pQCD processes.

This program uses subroutines of PYTHIA for simulation of hard scattering, multiple minijet production with initial and final state radiation. Minijet production is dominated by gluon scatterings. Kinematic variables of hard scattered partons are generated in the spirit of PYTHIA. HIJING uses also string fragmentation JETSET routines for hadronization. Cross section for hard scattering σ_{jet} is calculated in leading order, but so called *K-factor* ≈ 2 is used to simulate roughly higher order correlations. Low $p_\perp$ cutoff parameter $p_{\perp 0} = 2\,\text{GeV}$ is used to calculate inclusive cross section σ_{jet}. Nuclear shadowing of parton structure functions enables to study nuclear effects. Parton structure functions are modified in the nucleus and it has been observed [50], that the effective number of quarks and antiquarks is diminished in a nucleus. Therefore some partons are shadowed by others as discussed in Subsec. 2.2.3. Shadowing effect for gluons is expected to be the same like that for quarks.

The scheme of soft interactions is similar to FRITIOF model. This type of interactions is characterized by the small transverse momentum $p_\perp$ which is extended to the minijet cutoff $p_{\perp 0}$. Soft interactions are modelled by multiple soft gluon exchanges between valence quarks or diquarks. In addition to the soft gluon exchanges $p_\perp < p_{\perp 0}$, HIJING includes very low $p_\perp$ transfers to the valence quarks or diquarks at the string ends. The distribution of such extra $p_\perp$ kick is chosen to ensure a smooth extrapolation of $p_\perp$ from soft to hard processes.

HIJING can also use triggering on large $p_\perp$ jet production in order to increase the simulation efficiency. It causes enhancement of minijet production. HIJING provides also decays of unstable particles.

Nucleus-nucleus collision is decomposed into particular binary nucleon-nucleon collisions. Their number is computed by means of Wood-Saxon nuclear density at a given impact parameter for collision. For each of the binary collisions, the eikonal formalism is used to compute the probability of elastic, inelastic collision or number of jets. Wounded nucleons, which are generally the interacting ones, are represented by the excited strings along the beam direction.

HIJING has been extensively tested and tuned to data of pp and $p\bar{p}$ in a wide energy range of $\sqrt{s} = 50\text{-}1800\,\text{GeV}$ and to data from $p + A$ and $A + A$ (A means nucleus) collisions at moderate energies $\sqrt{s} \leq 20\,\text{GeV}/N$ [51].

3.1.2 Use of HIJING

Simulations were performed with HIJING Monte Carlo program available at website of Xin-Nian Wang (one of the author of HIJING) [52]. Program description with the main options and parameters can be found in [51]. HIJING is composed of two files, which denote also the used version of program: *hijing1.383* and *hipyset1.35*. Monte Carlo generator contains also decays of unstable particles, which were used in order to leave in final state only $\pi^{\pm}$, K_L^0, $K^{\pm}$, γ, p, $\bar{p}$, n, $\bar{n}$, $\mu^{\pm}$, $e^{\pm}$ and *neutrinos*. HIJING uses two types of frame of the collision: laboratory and *CMS* frame, the latter one is more convenient for generating events in condition of the LHC and ATLAS. Elastic scattering and diffraction reactions were turned off to test minimum bias events. According to the HIJING manual [51], the program contains a specific variable to inform whether collision is elastic, inelastic, single diffractive or double diffractive. However double diffraction is not implemented in used version of the code.

3.2 PYTHIA

3.2.1 The Description of PYTHIA

The Monte Carlo generator PYTHIA is well known program in high energy particle physics. It is frequently and successfully used to reproduce multiparticle production involving e^+e^-, ep and pp collisions. PYTHIA is based on pQCD with around 240 different hard processes of type $2 \rightarrow 1$ and $2 \rightarrow 2$ involving 1 and 2 final-state objects. Beside hard interactions, PYTHIA includes soft interactions: diffractive and elastic scattering. Additionally there are many other groups of processes such as heavy-flavour production, photon-induced processes ($\gamma g \rightarrow q\bar{q}$), standard model Higgs production, W/Z production, prompt photon production ($qg \rightarrow q\gamma$). The cross section for process $ij \rightarrow k$ is given by

$$\sigma_{ij \rightarrow k} = \int dx_1 \int dx_2 \, f_i^1(x_1) \, f_j^2(x_2) \, \hat{\sigma}_{ij \rightarrow k} \,, \qquad (3.1)$$

where $\hat{\sigma}_{ij \rightarrow k}$ is the elementary cross section for the hard partonic interaction and $f_k^a(x_a)$ is the parton distribution function of a parton k inside particle a. The cutoff parameter is $p_{\perp 0} = 2$ GeV as the minimum transverse momentum in hard processes.

Initial and final state radiation is included as a sequence of $1 \rightarrow 2$ processes. The probability for a parton to branch is given by the so called *branching func-tions*, which emerge in the *DGLAP* evolution equations [53]. Branching functions in QCD can be obtained by means of generalization of the basic idea of the so called *Weizsäcker-Williams approximation* in Quantum Electrodynamics (QED) [53]. In PYTHIA several branching processes have been included. They involve quarks (q), gluons (g), leptons (l) and photons (γ): $q \rightarrow qg$, $g \rightarrow gg$, $g \rightarrow q\bar{q}$, $q \rightarrow q\gamma$, $l \rightarrow l\gamma$.

PYTHIA uses Lund-type model for string fragmentation along the lines of JET-SET. Beside this, independent fragmentation is an option. Fragmentation proceeds

iteratively, namely string→ hadron + remainder string and so on. Branching processes are of probabilistic nature. Most of particles produced in the fragmentation process are unstable and subsequently decay into stable particles.

3.2.2 Use of PYTHIA

Program PYTHIA is available at webpage [54] as an independent code, but it is also feasible to run PYTHIA within the frame of program ROOT, data analysis tool [55]. PYTHIA version *6.221* which is included in ROOT version *4.00/93* was used. It allows to apply immediately ROOT tools for data analysis. PYTHIA uses several frames of a collision, but *CMS* frame is the most suitable for generating collisions described below. PYTHIA generates only collisions of elementary particles.

It is needful to keep consistency between events generated by different simulators. All available QCD hard processes were turned on: $f_i f_j \to f_i f_j$, $f_i \bar{f}_i \to f_k \bar{f}_k$, $f_i \bar{f}_i \to gg$, $f_i g \to f_i g$, $gg \to f_k \bar{f}_k$, $gg \to gg$ with the same notation used to describe processes 2.6. From soft QCD processes only low $p_\perp$ production was included. Single diffraction was turned off as well as double diffraction and elastic scattering. PYTHIA includes decays of unstable particles. Decays were turned on in order to have the same particles as in HIJING, i.e. $\pi^\pm$, K_L^0, $K^\pm$, γ, p, $\bar{p}$, n, $\bar{n}$, $\mu^\pm$, $e^\pm$ and *neutrinos*.

3.3 The Quark-Gluon String Model with Jets - QGSJET

3.3.1 The Description of QGSJET

The Quark Gluon String Model allows to consider hadron interactions at large distances and small transverse momenta. The probability of inelastic interaction between hadrons i and j can be defined by means of the following eikonal [9]:

$$\chi_{ij}^P (s, b) = \frac{\gamma_i \gamma_j}{R_{ij}^2} \exp \left(\Delta y - \frac{b^2}{4R_{ij}^2} \right) , \qquad (3.2)$$

where s is the *CMS* energy squared, b denotes the impact parameter, $y = \ln(s)$, $\Delta = \alpha_P(0) - 1$ and $R_{ij}^2 = R_i^2 + R_j^2 + \alpha_P'(0) y$. Δ and $\alpha_P'(0)$ are so called parameters of the Pomeron trajectory and with other parameters γ_i, R_i describe the Pomeron-hadron vertices. These parameters have to be extracted from the experimental data. QGSM model was also extended to dealt with hadron-nucleus interactions using Glauber approach [56].

Numerous CR data were reproduced in the framework of QGSM. For instance characteristics of EAS [57, 58, 59], muons and electrons in atmosphere [60] and so on. It became possible to consider QGSM as the base one for calculations at ultra-high energies. Approach of QGSM model offered simulation of ultra-high energetic CR

iteratively, namely string→ hadron + remainder string and so on. Branching processes are of probabilistic nature. Most of particles produced in the fragmentation process are unstable and subsequently decay into stable particles.

3.2.2 Use of PYTHIA

Program PYTHIA is available at webpage [54] as an independent code, but it is also feasible to run PYTHIA within the frame of program ROOT, data analysis tool [55]. PYTHIA version *6.221* which is included in ROOT version *4.00/93* was used. It allows to apply immediately ROOT tools for data analysis. PYTHIA uses several frames of a collision, but *CMS* frame is the most suitable for generating collisions described below. PYTHIA generates only collisions of elementary particles.

It is needful to keep consistency between events generated by different simulators. All available QCD hard processes were turned on: $f_i f_j \rightarrow f_i f_j$, $f_i \bar{f}_i \rightarrow f_k \bar{f}_k$, $f_i \bar{f}_i \rightarrow gg$, $f_i g \rightarrow f_i g$, $gg \rightarrow f_k \bar{f}_k$, $gg \rightarrow gg$ with the same notation used to describe processes 2.6. From soft QCD processes only low $p_\perp$ production was included. Single diffraction was turned off as well as double diffraction and elastic scattering. PYTHIA includes decays of unstable particles. Decays were turned on in order to have the same particles as in HIJING, i.e. $\pi^\pm$, K_L^0, $K^\pm$, γ, p, $\bar{p}$, n, $\bar{n}$, $\mu^\pm$, $e^\pm$ and *neutrinos*.

3.3 The Quark-Gluon String Model with Jets - QGSJET

3.3.1 The Description of QGSJET

The Quark Gluon String Model allows to consider hadron interactions at large distances and small transverse momenta. The probability of inelastic interaction between hadrons i and j can be defined by means of the following eikonal [9]:

$$\chi_{ij}^P (s, b) = \frac{\gamma_i \gamma_j}{R_{ij}^2} \exp \left(\Delta y - \frac{b^2}{4R_{ij}^2} \right) , \qquad (3.2)$$

where s is the *CMS* energy squared, b denotes the impact parameter, $y = \ln (s)$, $\Delta = \alpha_P (0) - 1$ and $R_{ij}^2 = R_i^2 + R_j^2 + \alpha_P' (0) \, y$. Δ and $\alpha_P' (0)$ are so called parameters of the Pomeron trajectory and with other parameters γ_i, R_i describe the Pomeron-hadron vertices. These parameters have to be extracted from the experimental data. QGSM model was also extended to dealt with hadron-nucleus interactions using Glauber approach [56].

Numerous CR data were reproduced in the framework of QGSM. For instance characteristics of EAS [57, 58, 59], muons and electrons in atmosphere [60] and so on. It became possible to consider QGSM as the base one for calculations at ultra-high energies. Approach of QGSM model offered simulation of ultra-high energetic CR

25

interactions, but also at lower energies this approach ensured a good agreement with the data.

The problem how to implement minijets into the QGSM come up, because modern accelerator data have demonstrated increasing influence of semihard processes. For this purpose, treatment of semihard interaction was proposed [61] and model denoted as *Quark-Gluon String model with JETs* (QGSJET) was created. It is based on eikonal approach, but it allows to include not only hard interaction of partons, but also the preceding soft preevolution as well [9, 42].

Interactions of partons can be divided into two parts. Non-perturbative soft cascades are characterized by small momentum transfer $Q_t^2 < Q_0^2$ and they are described as usual soft Pomeron emission. The second part is described perturbatively and it comprises hard cascades with $Q_t^2 > Q_0^2$. Q_0 is about $2\,\text{GeV}$. Cross sections can be calculated by means of the expression 2.11 which was discussed in Subsec. 2.2.3 in the previous Chapter. $\chi_s\left(b^2, s\right)$ represents the soft part of eikonal and it is the same as the one given by Eq. 3.2. It corresponds to the soft Pomeron exchange. The second term $\chi_h\left(b^2, s\right)$ corresponds to the semihard interaction treated as the soft Pomeron emission (soft preevolution) followed by the hard interaction of partons. Cross sections of various processes can be obtained in the same way as in the QGSM model, but one has to use the eikonal 2.11 instead of the 3.2. QGSJET model employs *semihard Pomeron* scheme, where phenomenological soft Pomeron treatment is applied for soft part of the parton cascade. General semihard processes are described as exchanges of a *semihard Pomeron* represented by a piece of QCD ladder sandwiched between two soft Pomerons (see 3.1). Consequently, a general Pomeron appears to be the sum of the semihard and soft ones. Soft Pomerons can be described as a cascade of partons with $p_\perp < Q_0$.
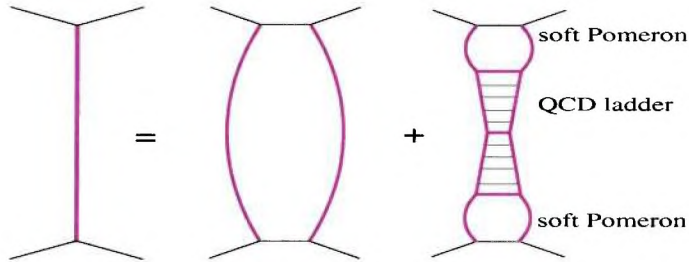

Figure 3.1: A general 'Pomeron' (l.h.s.) is the sum of the soft (the first graph on the r.h.s.) and semihard (the second graph on the r.h.s.) ones, taken from [42].

Initial and final state radiation are implicitly switched on due to method used to simulate hard processes. QGSJET reproduces the experimental EAS data quite well. Comparison of QGSJET predictions to experimental data at energies $10^{15} - 10^{19}\,\text{eV}$ demonstrated good agreement for instance in lateral distribution of muons and charged particles or correlation between shower maximum depth and primary

energy [9]. Among several interaction models, QGSJET reproduces the data from KASCADE experiment [62] best [1, 14]. On the other hand at large muonic shower sizes, which is encountered at energies above the knee, this model fails to reproduce certain observables. Model predicts more hadrons, than observed experimentally [14].

3.3.2 Use of QGSJET

QGSJET is one of the generators of high energy collisions (for particles with energy $E > 80\,\text{GeV}$) included in CORSIKA [21]. The version of QGSJET, by which collisions were generated, was denoted by author as *qgsjet01c*. QGSJET produces 20 types of particles: π^0, $\pi^\pm$, p, $\bar{p}$, n, $\bar{n}$, $K^\pm$, K^0_S, K^0_L, Λ, $\bar{\Lambda}$, $D^\pm$, D^0, $\bar{D}_0$, Λ_C, $\bar{\Lambda}_C$, η. QGSJET does not contain decays of unstable particles and therefore subroutines from CORSIKA of version *6.2040* were used for decay following particles: π^0, $K^\pm$, K^0_S, K^0_L, η and strange baryons: Λ, $\bar{\Lambda}$, $\Sigma^\pm$, Σ^0, $\Xi^\pm$, $\Omega^\pm$.

To switch on production of charmed particles, probabilities of cc quark pairs creation have to be set in *qgsjet01* code. These parameters have default values 0, because CORSIKA does not deal with charmed particles. Simulations were performed with nonzero probabilities, which are written as notes in the code by the author of QGSJET. Decays of charmed particles were carried out according to decay branching ratios [41]. Consequently, all unstable particles decayed and output of events contained only following particles: $\pi^\pm$, K^0_L, $K^\pm$, γ, p, $\bar{p}$, n, $\bar{n}$, $\mu^\pm$, $e^\pm$ and *neutrinos*.

QGSJET is originally proposed to generate cosmic ray interactions. This is why the energy of interaction is referred to the laboratory frame. QGSJET distinguishes between projectile and target particle.

Minimum bias events as discussed in Chapter 1 are defined as non-diffractive ones. Type of the interaction is stored in specific variable in QGSJET. Events which were denoted as diffractive were eliminated in order to produce only inelastic non-diffractive collisions.

3.4 QGSJET-II

3.4.1 The Description of QGSJET-II

QGSJET-II model is a new developed MC model [11]. It is based on and similar to QGSJET, but QGSJET-II accounts for non-linear corrections when calculating hadron-hadron cross sections and treats non-linear effects explicitly in individual hadronic and nuclear collisions. At very high energies and small impact parameters, high parton densities emerge. Therefore parton cascades are not independent as in Fig. 2.8. Parton cascades influence each other and overlap and these modifications give rise to non-linear effects. In particular, it can lead to merging of parton ladders, see Fig. 3.2. At high energies, parton densities in the low virtuality region are saturated. In other words, further parton branchings are compensated by the fusion of other parton cascades. A description of non-linear effects in the QGSJET-II
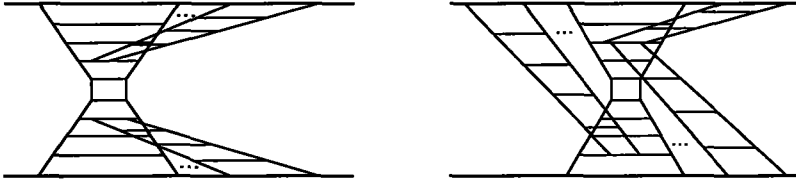
Figure 3.2: Diagrams of non-linear parton effects, taken from [42].

model is based on the assumption that saturation effects can be neglected for parton virtualities bigger than some fixed, energy independent cut-off parameter Q_0. In this approach multi-ladder graphs in Fig. 3.2 are described by interactions between Pomerons. Provided multi-Pomeron vertices are relevant for parton processes at low virtualities $|q^2| < Q_0^2$, all significant contributions of that kind can be summed. QGSJET-II employs this scheme for treating hadronic and nuclear collisions. The triple Pomeron coupling has been inferred from HERA data on hard diffraction in deep inelastic scattering.

3.4.2 Use of QGSJET-II

QGSJET-II was obtained by private communication with S. Ostapchenko, the author of the generator. Version *qgsjet-II-03* was used. This is not the final version of the program and therefore it is assumed that program will be tested and can be modified. QGSJET-II is originally designed for cosmic ray interactions as well as QGSJET, and it discerns between target and projectile particle. The natural frame for cosmic ray collisions is the laboratory system, which is used to set colliding parameters in QGSJET-II.

QGSJET-II produces only 14 types of secondary particles: π^0, $\pi^{\pm}$, p, $\bar{p}$, n, $\bar{n}$, $K^{\pm}$, K_L^0, K_S^0, η, Λ, $\bar{\Lambda}$. QGSJET-II does not work with charmed particles contrary to the QGSJET. No subroutines for particle decays are included as well. For this purpose subroutines included in program CORSIKA (version *6.2040*) were used for decay of π^0, K_S^0, η, Λ and $\bar{\Lambda}$. Eventually, the output from QGSJET-II contains the same particles as in cases of other used generators: $\pi^{\pm}$, K_L^0, $K^{\pm}$, γ, p, $\bar{p}$, n, $\bar{n}$, $\mu^{\pm}$, $e^{\pm}$ and *neutrinos*.

Every nucleon participating in collision is characterized according to the type of its interaction. Nucleons can be intact, recoiled from diffraction or they can suffer from inelastic interaction or diffraction. Events without inelastic interaction were left out. At least one inelastic interaction had to be among target as well as projectile nucleons. Events, which contained diffracted nucleons were also omitted.

3.5 Test of Generators at Tevatron Energy

Before tests of generators at LHC energies, it is useful to make simulations at lower energies, in energy region, where data have been already obtained. Comparison of simulation results at LHC energies with results at lower energies can demonstrate how differences of generators will show up after increase of energy up to value achievable at LHC. For purposes of making simulations at lower energies, $\bar{p}p$ collisions at Tevatron energy $\sqrt{s} = 1.8\,\text{TeV}$ are very convenient. Some generators can be tuned to reproduce the real data for mentioned energy region and differences among testing models can appear at higher energies. Collisions were generated with initial momenta of primary particles in z-axis. Fig. B.1 in Appendix B shows the orientations of momenta of $\bar{p}$ and p and the orientation of the z-axis. All unstable particles decayed as described above and event output contained only particles: $\pi^{\pm}$, K_L^0, $K^{\pm}$, γ, p, $\bar{p}$, n, $\bar{n}$, $\mu^{\pm}$, $e^{\pm}$ and *neutrinos*. Generators were set and used according to descriptions in particular Subsecs.. The total of $5 \cdot 10^5$ events were generated by every program.

There are comparisons of some quantities for particles: $\pi^{\pm}$, $K^{\pm}$, γ, p, $\mu^{\pm}$ below. Statistical errors are drawn in all histograms, but they are very small in some cases on account of large number of events. For lucidity, all histograms were normalized to 1000 events and also statistical errors were recalculated according to the normalization. There are four histograms with distributions of quantities for pions in Fig. 3.3. The y-axis denoted as N_{part} represents the number of particles. E_{part}, which denotes the y-axis in pseudorapidity histograms weighted by energy, means in other words the energy carried by particles in corresponding pseudorapidity interval. The upper left histogram represents multiplicity of pions produced per 1000 events. There is apparent similarity between HIJING and PYTHIA and also between QGSJET and QGSJET-II curves. On the other hand, two types of curves are of different shapes from each other. QGSJET and QGSJET-II most frequently produce about 20 charged pions, while PYTHIA and HIJING produce approximately two times more charged pions. The multiplicity of produced pions ends at 95 pions for PYTHIA and HIJING, whereas production of charged pions generated by QGSJET and QGSJET-II goes behind this limit. The lower part of QGSJET-II histogram is very interesting, because it is evident that in some events QGSJET-II produces no pions and production up to 10 charged pions is fairly frequent, while PYTHIA and HIJING produce in all cases more than 10 pions per event. QGSJET produces in some cases less than 10 pions per event, but it is insignificant. The QGSJET-II histogram is similar to the case of collisions with diffractive interactions. As the diffraction was switched off, events with small number of pions correspond to hard diffraction processes. The upper right histogram in Fig. 3.3 shows pseudorapidity distributions. PYTHIA and HIJING have almost the same pion pseudorapidity distribution, but QGSJET and QGSJET-II differentiate in the central region. The smallest number of pions in region $|\eta| < 3$ produces QGSJET-II.

Transverse momentum distributions of charged pions shows two types of curves again. In the region with $p_\perp > 0.8\,\text{GeV}$ QGSJET and QGSJET-II produce more high
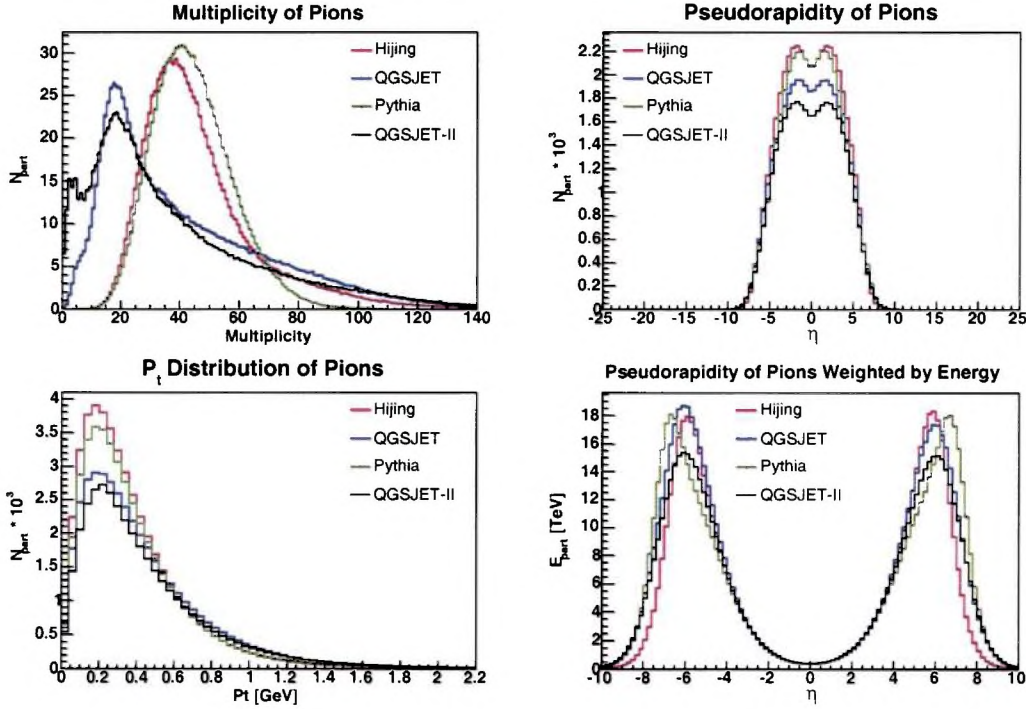
Figure 3.3: Results of generated collisions of $\bar{p}p$ at energy $\sqrt{s} = 1.8\,\text{TeV}$, charged pion distributions. Histograms are equivalent to 10^5 simulated events.

$p_\perp$ pions than other two generators.

Pseudorapidity distributions of $\pi^\pm$ weighted by energy are in range $|\eta| < 4$ the same for all generators and differs in the very forward regions.

Displayed errors are so small, that they are almost not visible in histograms and therefore the statistical errors do not influence conclusions. Histograms of mentioned quantities in case of all charged particles are almost same as in the case of charged pions, because pions represent the vast majority of charged particle production.

Fig. 3.4 comprises distributions of $K^\pm$ distributions. HIJING and PYTHIA have very similar multiplicity distribution of kaons. They produce a non-zero number of kaons (about 4) most frequently. QGSJET also produces non-zero number of kaons most frequently, but smaller than in the latter case. The high multiplicity (more than ten kaons) is more frequent for QGSJET than PYTHIA and HIJING. QGSJET-II produces so small number of $K^\pm$, that the most probable multiplicity is 0. Number of events characterized by nonzero multiplicity decreases with increasing multiplicity.

Pseudorapidity distributions (upper right histogram in Fig. 3.4) are considerably different for QGSJET-II and other generators. The discrepancy is caused by the total $K^\pm$ production, which is almost two times smaller for QGSJET-II than for others.

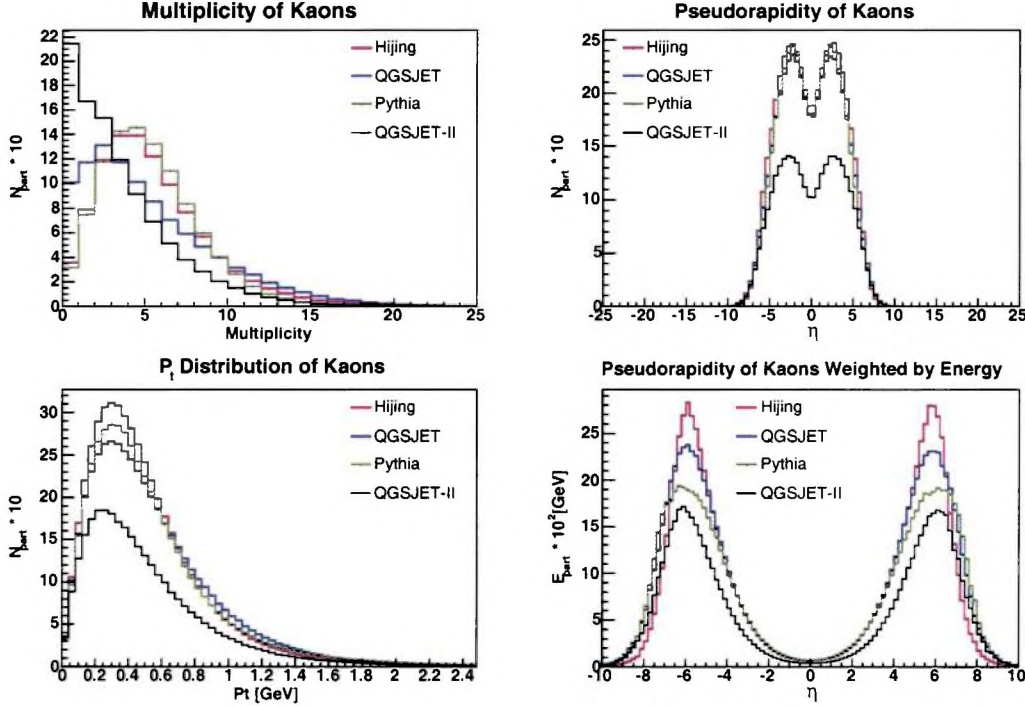The shape of transverse momentum distributions of $K^\pm$ for PYTHIA, QGSJET

Figure 3.4: Results of generated collisions of $\bar{p}p$ at energy $\sqrt{s} = 1.8\,\text{TeV}$, charged kaon distributions. Histograms are equivalent to 10^5 simulated events.

and HIJING is similar to that as in the case of $\pi^{\pm}$, but in general the width at half of maximum is greater for $K^{\pm}$. The curve corresponding to QGSJET-II is smaller due to the total $K^{\pm}$ multiplicity and the mean value is shifted closer to the zero.

Pseudorapidity weighted by energy in range $|\eta| < 5$ is almost identical for HIJING, PYTHIA and QGSJET and differs from curve belonging to QGSJET-II. But in the range $5 < |\eta| < 6.5$ all curves can be distinguished from each other and the highest value corresponds to HIJING.

Fig. 3.5 shows four histograms with quantities, which describe proton distributions. It is apparent that all generators differ in proton multiplicity and the highest is that of HIJING and the smallest values are those of QGSJET-II (see upper right histogram in Fig. 3.5, which describes the pseudorapidity distribution). Differences between QGSJET-II and HIJING is of the order of two in pseudorapidity range $|\eta| < 5$. QGSJET-II also produces most protons in the very forward region. In pseudorapidity interval $-9.5 < \eta < -6.5$ there are peaks in pseudorapidity distribution for all generators. The origin of this peak lies in leading particle effect. One of its quark plays the role of leading parton and after hadronization this quark appears in proton again. For instance in PYTHIA, this proton with $-9.5 < \eta < -6.5$ is almost in half of all collisions and there is no rapidity gap.
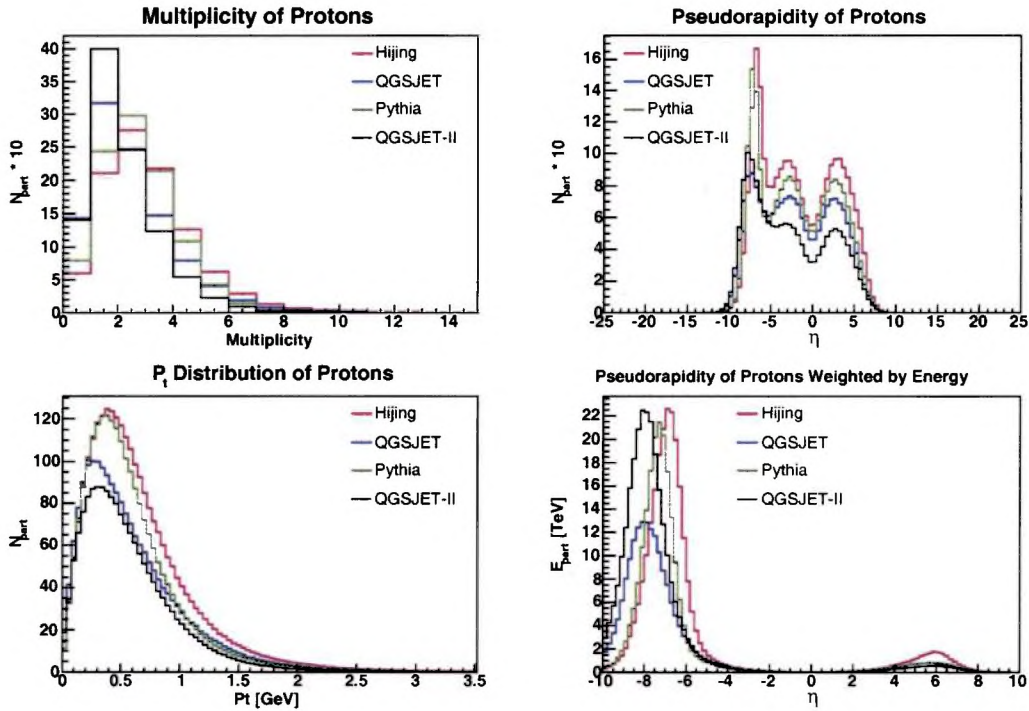
Figure 3.5: Results of generated collisions of $\bar{p}p$ at energy $\sqrt{s} = 1.8\,\text{TeV}$, proton spectra. Histograms are normalized to 1000 events.

Distributions of $\bar{p}$ are related to those of p. Multiplicity and $p_\perp$ distribution are almost the same for $\bar{p}$ and for p, but pseudorapidity distributions of $\bar{p}$ and p (and of course pseudorapidity distributions weighted by energy) are mirror symmetric to each other according to the axis $\eta = 0$. Symmetry is caused by the fact, that incident particles are just $\bar{p}$ and p and their momenta lies on the z axis with the opposite orientation.

Differences in pseudorapidity in very forward region are more distinctive when pseudorapidity is weighted by energy (see right down histogram in Fig. 3.5). HIJING has mentioned peak closest to the central region and on the other hand QGSJET-II has this peak most far from the central region. Pseudorapidity distribution histogram compared with the same distribution weighted by energy shows that protons corresponding to the forward peak are more energetic in QGSJET-II than in HIJING.

Properties of quantities corresponding to gamma particles can be seen in Fig. 3.6. The majority of gammas originates from π^0. This can be seen in multiplicity histogram as peaks for even multiplicities. π^0 decays most frequently into two γ and therefore even numbers of gammas are preponderant. PYTHIA produces gammas up to multiplicities of about 120, but other generators produce events with more gamma particles. The lower part of the QGSJET-II curve for γ multiplicity is worth
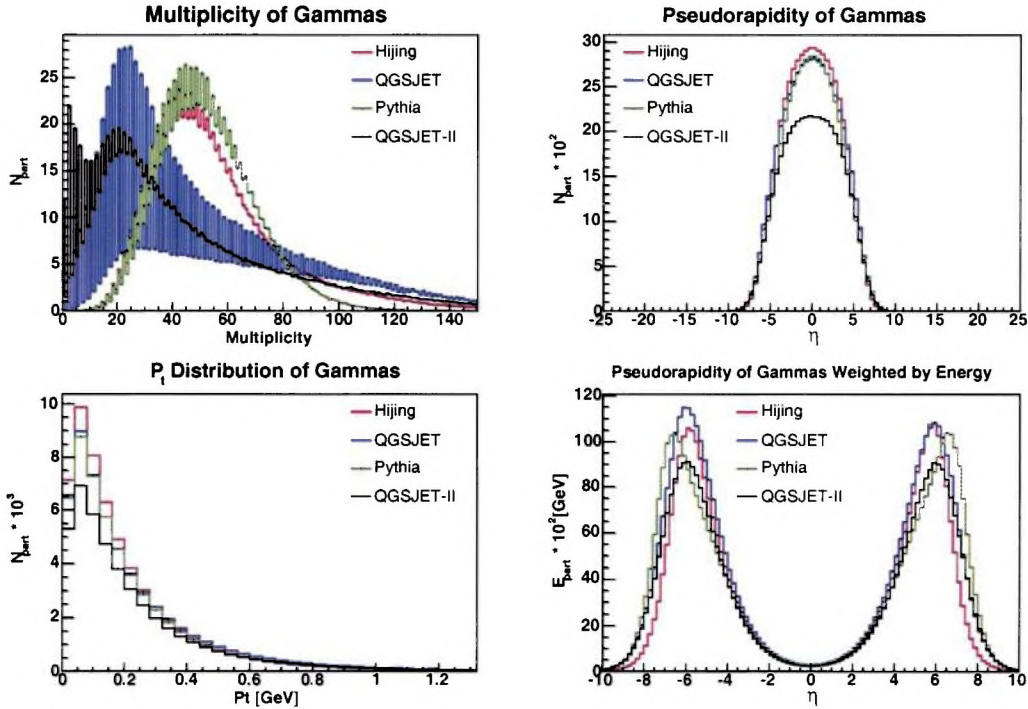
Figure 3.6: Results of generated collisions of $\bar{p}p$ at energy $\sqrt{s} = 1.8\,\text{TeV}$, gamma distributions. Histograms are normalized to 1000 events.

discussing. There is indispensable production of small number of γ. It is caused by specific collisions, in which small number of secondary particles are produced. For example only p, $\bar{p}$ and π^0. This interactions are marked as inelastic by means of variables in QGSJET-II program, but they are similar to diffractive ones. Pseudorapidity distributions of γ are very similar for HIJING, QGSJET and PYTHIA, but QGSJET-II produces again the smallest number of γ which is obvious in range $|\eta| < 5$. It is interesting, that accordance in pseudorapidity distribution is greater than in rapidity distribution of charged pions.

Two upper histograms in fig 3.7 shows multiplicity and pseudorapidity distributions of muons. There are only three non-zero curves, because QGSJET-II produces neither muons nor charmed particles, which are the only source of muons in QGSJET. It is apparent from multiplicity distribution that in most events there are no muons. It is obvious, that PYTHIA produces most muons among all generators, two times more than QGSJET, which has the smallest production. Histograms of Fig. 3.7 in which muon distributions are drawn are the only histograms, in which errors are not negligible. On the other hand there are regions in which differences among generators are so large, that statistical errors do not influence conclusions. In the range $|\eta| < 2$ the pseudorapidity distributions have small fluctuations. In forward region, the pro-
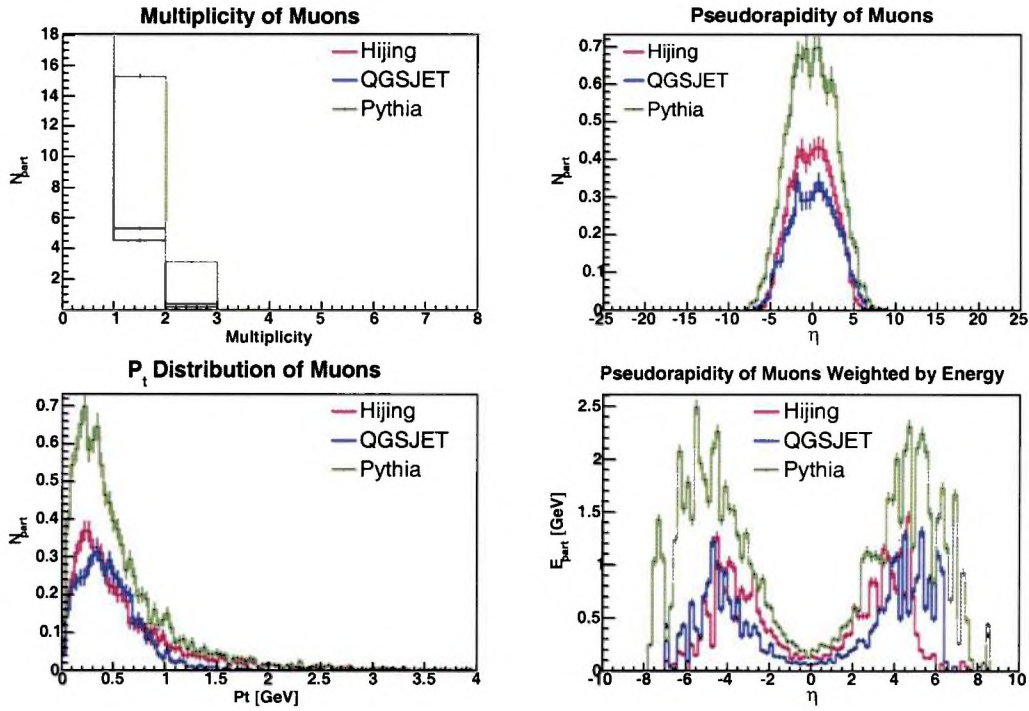
Figure 3.7: Results of generated collisions of $\bar{p}p$ at energy $\sqrt{s} = 1.8\,\text{TeV}$, muon histograms. Distributions are rescaled to 1000 events. QGSJET-II is not included because it does not produce muons.

duction of muons in QGSJET and HIJING is similar, but different from PYTHIA, which is apparent from all histograms, however, in this region large fluctuations are caused by energy weights.
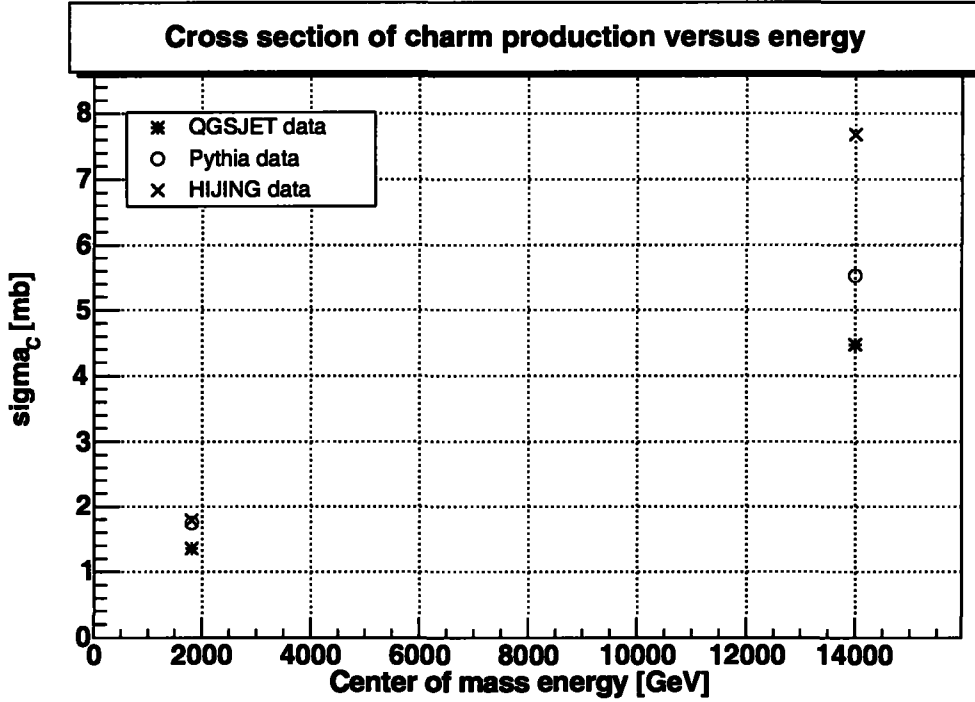
Cross section of charm production versus energy

Figure 3.8: Cross sections of charm production in pp collision for QGSJET, PYTHIA and HIJING.

3.6 Test of Charm Production

Test of charmed particle production in QGSJET, PYTHIA and HIJING has been performed. In QGSJET charmed particles are the only source of muons ($\pi^{\pm}$ are in this analysis considered as stable). QGSJET-II does not produce neither muons nor charmed particles. Charm productions were compared at Tevatron energy $\sqrt{s} = 1.8\,\mathrm{TeV}$ and at LHC energy $\sqrt{s} = 14\,\mathrm{TeV}$ in pp collisions. Sample of $N = 10^5$ events was generated inelastic collisions only. Every event was checked if some charmed particles (or J/ψ and its excitations) were produced. If σ_{inel} and σ_C represent inelastic cross section and cross section for charmed production, respectively, then:

$$\frac{N_C}{N} = \frac{\sigma_C}{\sigma_{inel}}. \tag{3.3}$$

Inelastic cross sections were taken from [41]. In HIJING and PYTHIA there are specific subroutines to make particles stable and they were used for particles with charm. There are 46 and 84 particles with charm in HIJING and PYTHIA, respectively. QGSJET produces only 6 types of charmed particles.

Charmed particle cross sections are plotted in Fig. 3.8. PYTHIA has the smallest charm production at Tevatron energy. Cross sections of HIJING and QGSJET are

35

very similar. Differences are larger at LHC energy. HIJING has at this energy the highest charm cross section and PYTHIA the smallest again.
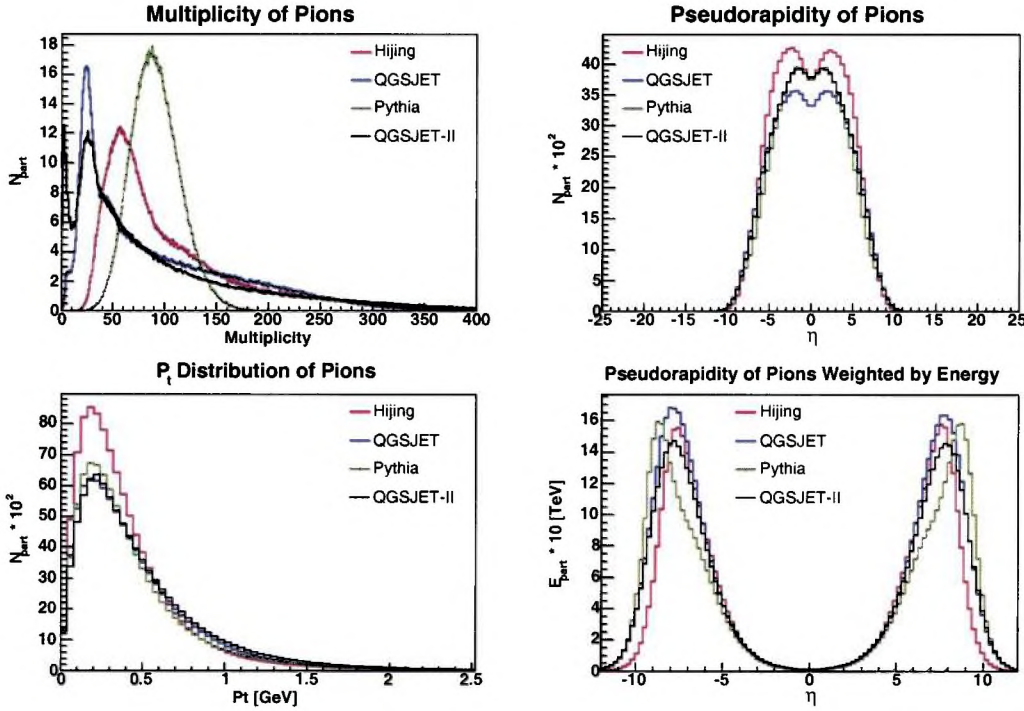
Figure 3.9: Results of generated collisions of pp at energy $\sqrt{s} = 14\,\mathrm{TeV}$, charged pion distributions. Histograms are normalized to 1000 events.

3.7 Test of Generators at LHC Energies

This section contains qualitative descriptions of simulation results of pp, pN, pS, pFe and NFe collisions generated at LHC conditions. Tables with mean values of multiplicities, energy distributions and $p_\perp$ distributions corresponding to each type of collision and generator are included in Appendix B.

3.7.1 Proton-Proton Collisions

The LHC collider and ATLAS experiment at CERN are primarily being constructed for pp collisions at CMS energy of $\sqrt{s} = 14\,\mathrm{TeV}$. No present-day collider can provide such energetic collisions, therefore information about particular particle productions given by generators are predictions. All four generators — PYTHIA, QGSJET, HIJING and QGSJET-II were tested. In order to be able to make a comparison with $\bar{p}p$ collisions at Tevatron energy (see Sec. 3.5) four-momenta of the same particles were stored and also the same settings of generators were used as written in Sec. 3.5. The total number of generated minimum bias events were $5 \cdot 10^5$, so that statistical errors do not influence conclusions concerning differences between simulators. There are five
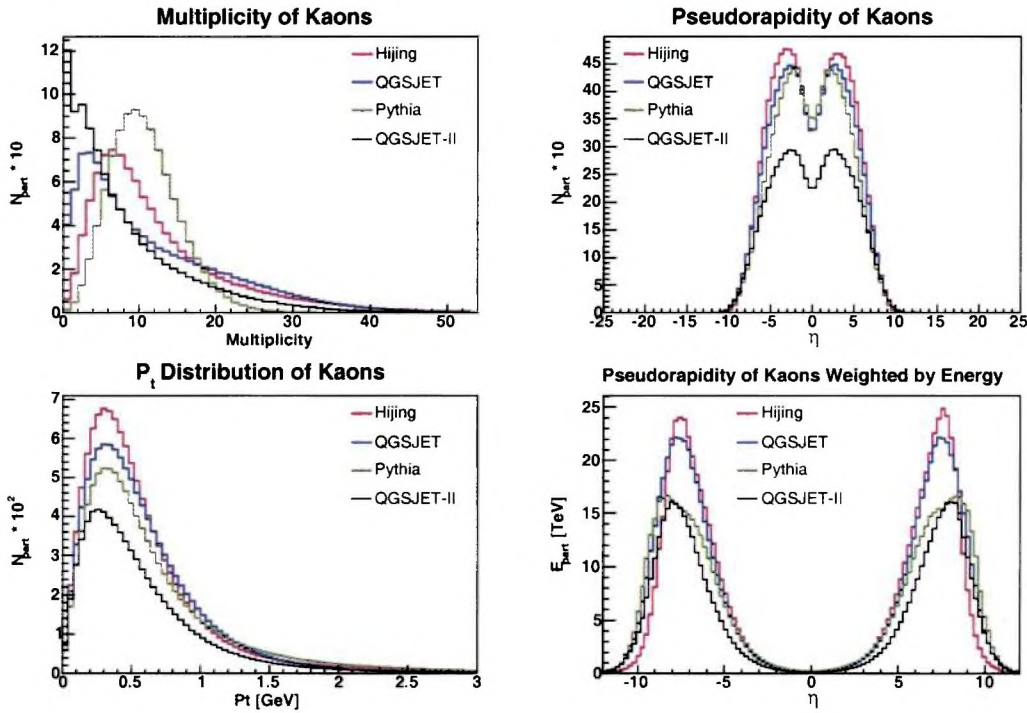
37

Figure 3.10: Results of generated collisions of pp at energy $\sqrt{s} = 14\,\mathrm{TeV}$, kaon spectra. Histograms are normalized to 1000 events.

figures with histograms of distributions of $\pi^{\pm}$, $K^{\pm}$, p, γ, $\mu\pm$. All histograms were normalized to 1000 events. Charged pion characteristics are drawn in Fig. 3.9. The upper left histogram describes $\pi^{\pm}$ multiplicities. General properties of histograms are the same as in $\bar{p}p$ collisions at Tevatron energy. Maximum multiplicity is two times higher than in $\bar{p}p$ interactions for PYTHIA and even more for other generators. There is also untypical amount of events with small number of pions (less than ten) among events generated by QGSJET-II. The peak representing events characterized by low $\pi^{\pm}$ multiplicity has approximately the same height as the peak between multiplicities 20 and 30, which represents the most frequent $\pi^{\pm}$ production. Large differences between HIJING and PYTHIA appear as compared with multiplicity of $\pi^{\pm}$ produced in $\bar{p}p$ collisions at Tevatron energy (see the upper left histogram in Fig. 3.3).

Pseudorapidity distributions of charged pions are drawn in the upper right histogram in Fig. 3.9. It is obvious, that QGSJET and PYTHIA generate almost the same rapidity distribution. Differences can be found in very forward regions if the rapidity is weighted by energy (the bottom right histogram in Fig. 3.9). HIJING produces the largest number of $\pi^{\pm}$ and therefore also the most of charged particles. On the other hand HIJING does not produce charged pions with absolute rapidity larger than 9.
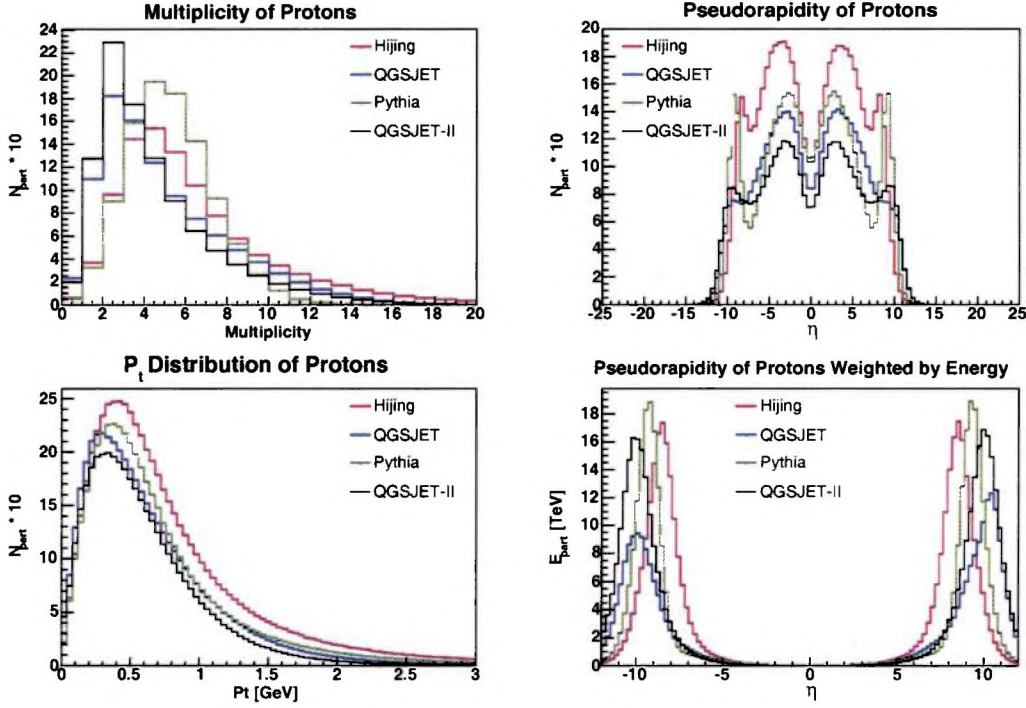
Figure 3.11: Results of generated collisions of pp at energy $\sqrt{s} = 14\,\mathrm{TeV}$, proton distributions. Histograms are normalized to 1000 events.

Four histograms concerning $K^{\pm}$ are drawn in Fig. 3.10. PYTHIA, HIJING and QGSJET produce in almost all events at least one charged K meson, but QGSJET-II produces most frequently no $K^{\pm}$. PYTHIA and HIJING do not have the same multiplicity curves as at Tevatron energy. Pseudorapidity distributions of kaons are very similar for PYTHIA, HIJING and QGSJET. The quantity of $K^{\pm}$ in pseudorapidity region $|\eta| < 5$ generated by QGSJET-II amounts to about 70 % of other simulator production. It is more than in $\bar{p}p$ interactions, but it still represents distinctly smaller amount.

Proton multiplicities (the upper left histogram in Fig. 3.11) differ from each other more than in $\bar{p}p$ collisions. HIJING produces the highest amount of protons. In central region ($|\eta| < 2$), production of protons in HIJING and PYTHIA is the same. QGSJET and QGSJET-II generate less protons in mentioned range, but differentials between HIJING and QGSJET-II are not so large as in $\bar{p}p$ interactions at lower energy. On the other hand, HIJING production of protons in region $4 < |\eta| < 8$ represents about 170 % of QGSJET-II production.

The upper left histogram in Fig. 3.12 shows multiplicities of gammas. General shape of curves is in principle similar to the results at Tevatron energy. PYTHIA differs markedly from HIJING in contrast to lower energy test. Gamma multiplicities
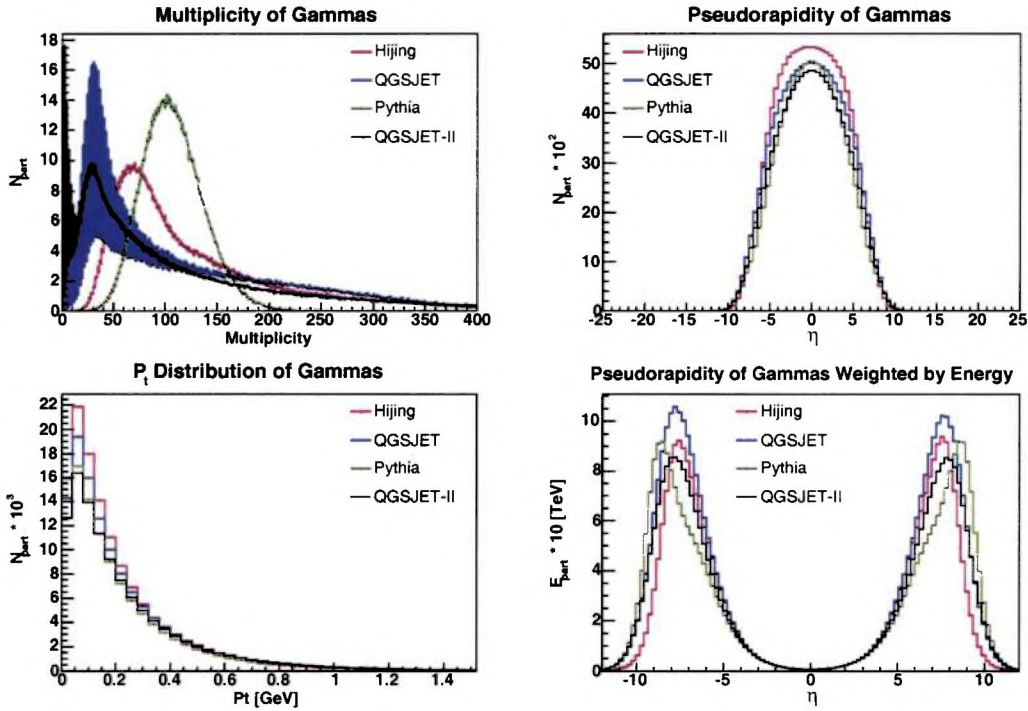
39

Figure 3.12: Results of generated collisions of pp at energy $\sqrt{s} = 14\,\text{TeV}$, gamma distributions. Histograms are normalized to 1000 events.

are quite similar in contrast to $\bar{p}p$ collisions. QGSJET-II increases the production of gammas comparatively to other generators.

Muon production is shown in histograms in Fig. 3.13. Differences among simulators are even larger than in test of generators at Tevatron energy. PYTHIA produces approximately three times more muons than QGSJET. There are statistical errors visible in histograms (see Fig. 3.13) in spite of $5 \cdot 10^5$ generated events. Fluctuations which influenced pseudorapidity distribution weighted by energy in range $|\eta| > 6$ (see the bottom right histogram) are caused by weights. QGSJET produces almost all muons with $p_\perp$ up to $\approx 1.5\,\text{GeV}$, whereas $p_\perp$ spectra of HIJING and PYTHIA are wider.
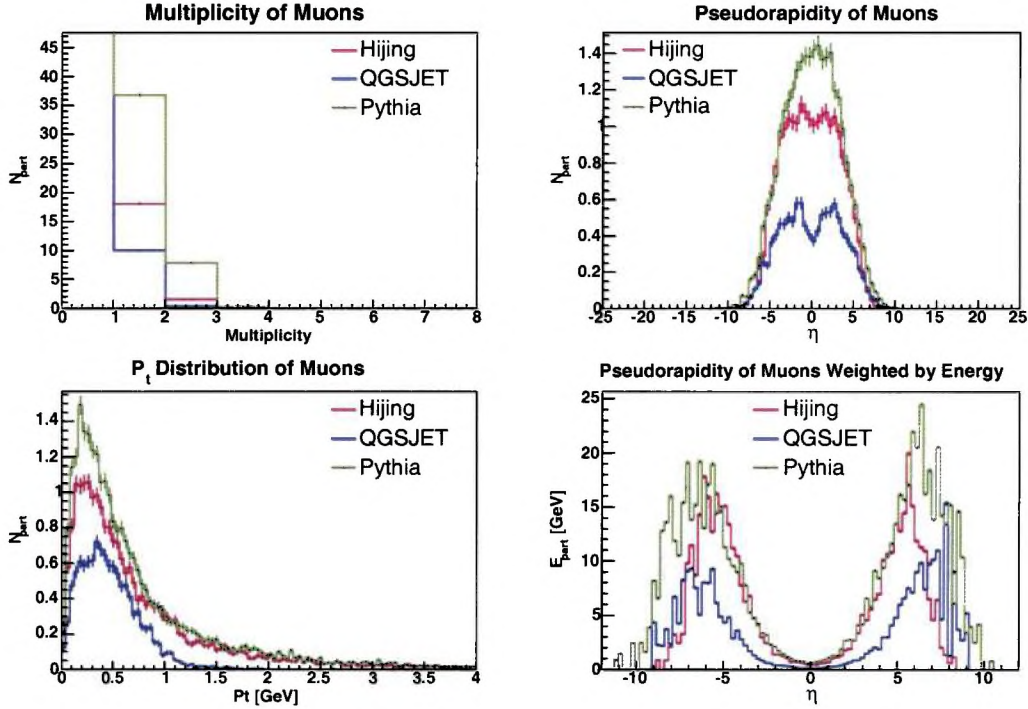
Figure 3.13: Results of generated collisions of pp at energy $\sqrt{s} = 14\,\text{TeV}$, muon spectra. Histograms are normalized to 1000 events. QGSJET-II is not included because it does not produce muons.

3.7.2 Proton-Nitrogen Collisions

To test proton-nucleus interactions nitrogen $^{14}_{7}\text{N}$ was used. The atmosphere consists of N_2, O_2 and Ar with the volume fractions of $78.1\,\%$, $21.0\,\%$ and $0.9\,\%$ [63]. Protons represents the vast majority of particles (including nuclei) contained in comic rays. Therefore pN collisions are very frequent and important for CR physics. PYTHIA can not be employed, because it generates only interactions between elementary particles. At LHC conditions nitrogen would have momentum of $p_N = 49\,\text{TeV}$ and proton $p_p = 7\,\text{TeV}$. It corresponds to *CMS* energy $\sqrt{s} \approx 37\,\text{TeV}$. After interaction four-momenta of secondary particles were transformed from particular generator frame to the frame, in which proton has momentum $7\,\text{TeV}$ and nitrogen $49\,\text{TeV}$ ('detector frame'). Directions and orientations of initial particle momenta and the z-axis after transformation are drawn in Appendix B in Fig. B.1. QGSJET and QGSJET-II are designed to generate $p \rightarrow A$ (or $A \rightarrow B$) collisions. Proton was the projectile and nitrogen was the target, this type of collision is natural for CR physics. The target nucleus is at rest in laboratory frame and non-interacting particles from target nucleus are not stored in QGSJET and QGSJET-II. Therefore only particles which
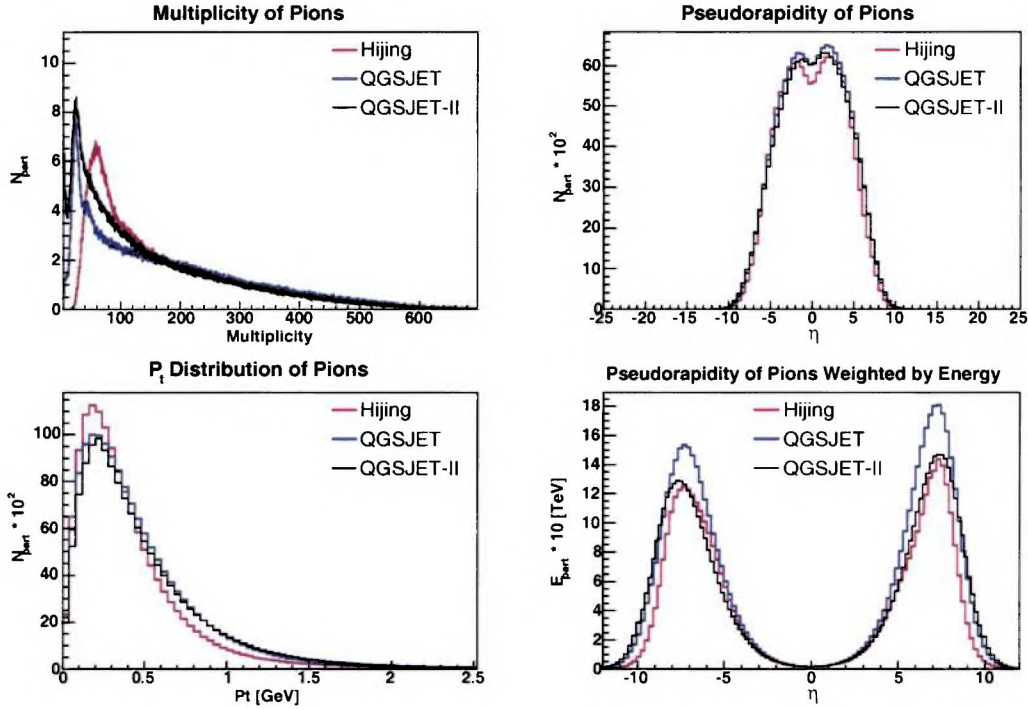
41

Figure 3.14: Results of generated collisions of pN at energy $\sqrt{s} = 37\,\mathrm{TeV}$, charged pion distributions. Histograms are normalized to 1000 events.

undergo some interaction were taken into account to set the same conditions for all generators. The settings of generators are the same as in the previous simulations and as described in Sec. 3.5. $350 \cdot 10^3$ of minimum bias events were generated and histograms were rescaled to 1000 events for lucidity.

Some properties of pion production are drawn in four histograms in Fig. 3.14. Number of particles is denoted as N_{part}, but in histograms describing pseudorapidity (or rapidity) weighted by energy, each value in particular bins means energy. Therefore y-axis is denoted as E_{part} similarly to previous Subsecs.. The most notable differences in pion multiplicities are in the region of small number of particles (the upper left histogram). Similarly to previous cases, HIJING does not produce events with pion multiplicity smaller than 20. Relatively large amount of QGSJET-II events has in the output less than 20 charged pions. The upper right histogram describing pseudorapidity distribution of pions demonstrates coincidence of results from all generators. It indicates that all generators have almost the same charged particle production, which is the very significant accordance.

Some differences can be found in $p_\perp$ distribution and in pseudorapidity weighted by energy in range $|\eta| > 6$. There is apparent asymmetry of pN collisions in the bottom right histogram.
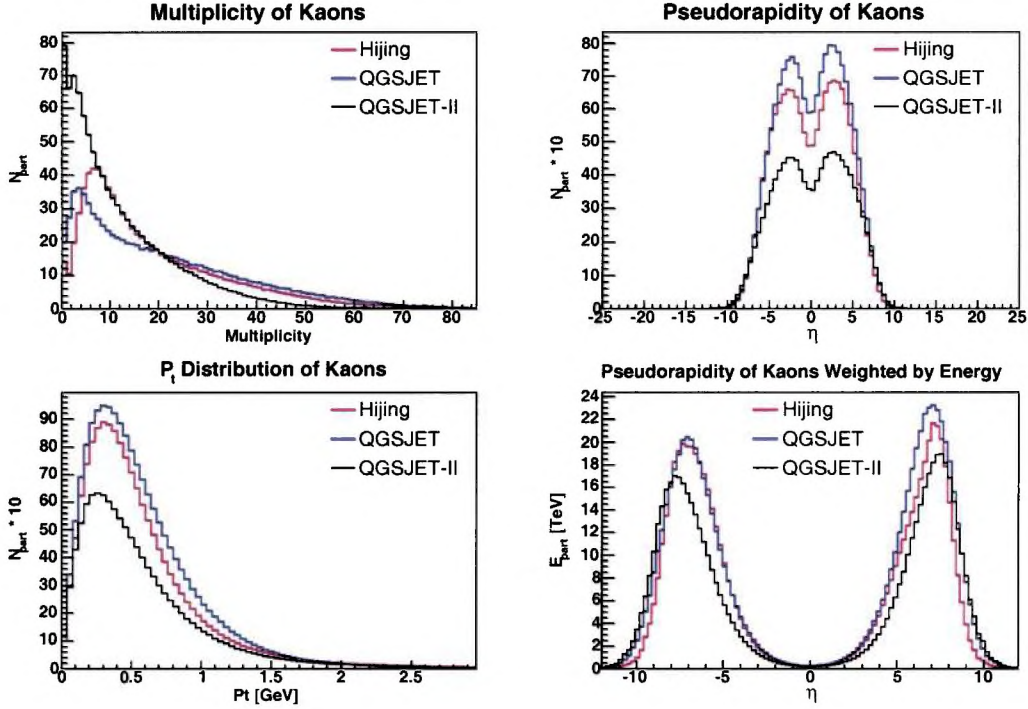
42

Figure 3.15: Results of generated collisions of pN at energy $\sqrt{s} = 37\,\text{TeV}$, kaon spectra. Histograms are normalized to 1000 events.

Some $K^{\pm}$ distributions are drawn in Fig. 3.15. They are very similar to those of K_L^0. QGSJET-II produces the smallest number of charged kaons again, but now there are differences even between HIJING and QGSJET of the order of 15 % at central region, QGSJET produces more $K^{\pm}$, whereas in pp collisions, HIJING was more productive in this regard.

QGSJET-II produces most frequently events with up to 5 secondary protons as noticeable from Fig. 3.16. HIJING and QGSJET multiplicities are similar. HIJING and QGSJET produce the same number of protons in central region, QGSJET-II generates smaller number of protons. Considerable differences among generators are apparent in the bottom right histogram, in which pseudorapidity weighted by energy is drawn. There are more protons with momentum in nearly the same directions as colliding particles in interactions generated by QGSJET and QGSJET-II. HIJING has more remnant protons than other generators. These protons are remnants from nitrogen nucleus and they have pseudorapidity more than 6. They are visible as peak in the pseudorapidity histogram (the upper right histogram in Fig. 3.16).

Gamma histograms are illustrated in Fig. 3.17. The general properties of multiplicity curves hold for all generators. Alternating numbers of events for even or odd gamma multiplicities for QGSJET again indicate that most of gammas originate
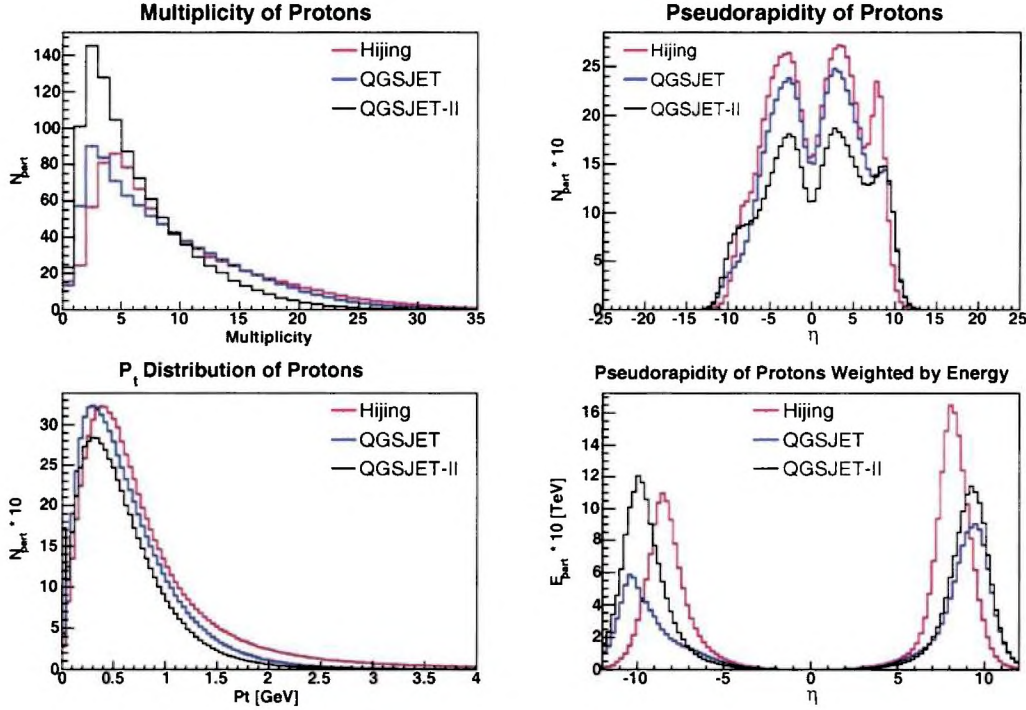
43

Figure 3.16: Results of generated collisions of pN at energy $\sqrt{s} = 37\,\mathrm{TeV}$, proton spectra. Histograms are normalized to 1000 events.

from π^0 decay. Pseudorapidity distribution shows, that QGSJET produces the most gammas and HIJING and QGSJET-II have the same gamma production, which is interesting, because charged pion pseudorapidity distribution is nearly identical for all generators. On the other hand not only π^0 are the source of gammas, of course. For example η decays in several decay modes into gammas and neutral pions without $\pi^\pm$ production. In other words, η can change the equilibrium between production of charged and neutral pions. The transverse momentum distribution of gammas does not indicate significant differences. Pseudorapidity distributions weighted by energy (the bottom right histogram in Fig. 3.17 are not symmetrical, because gammas going in the direction of incident nitrogen are more energetic that those with momenta orientated oppositely.

Histograms with muon characteristics in Fig. 3.18 indicate similar conclusions as in the case of pp collisions at $\sqrt{s} = 14\,\mathrm{TeV}$. QGSJET produces less than approximately half of muons than HIJING. Muons in QGSJET events originate from D-mesons, whereas HIJING has beside charmed particles also other sources of muons, for example B-mesons. This fact can be seen from charmed particle cross section (see Fig. 3.8). HIJING has cross section for charmed particle production larger by coefficient 1.4 in comparison with QGSJET at energy $\sqrt{s} = 14\,\mathrm{TeV}$. However, HIJING
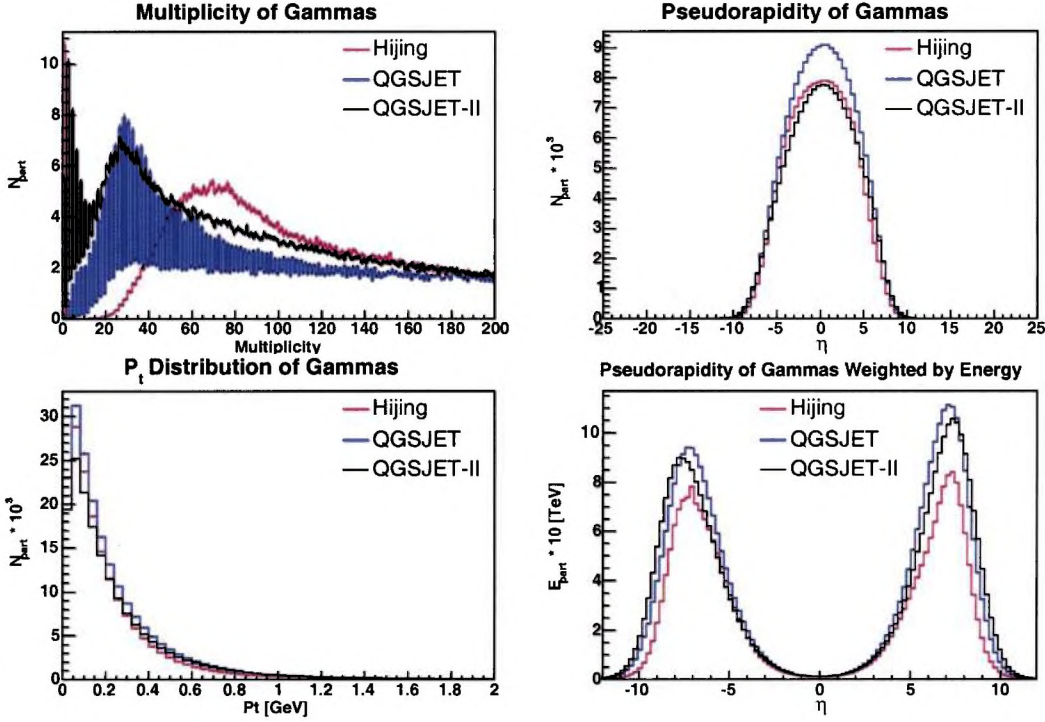
Figure 3.17: Results of generated collisions of pN at energy $\sqrt{s} = 37\,\mathrm{TeV}$, gamma spectra. Histograms are normalized to 1000 events.

produces two times more muons (see Fig. 3.13) than QGSJET. Therefore also in pN collisions other sources contribute to the muon production in case of HIJING. The shapes of pseudorapidity distributions are different as well. Muon production in range $|\eta| < 1$ is smaller than in range $1 < |\eta| < 3$ for QGSJET, while HIJING muon production in range $|\eta| < 3$ is quite flat.
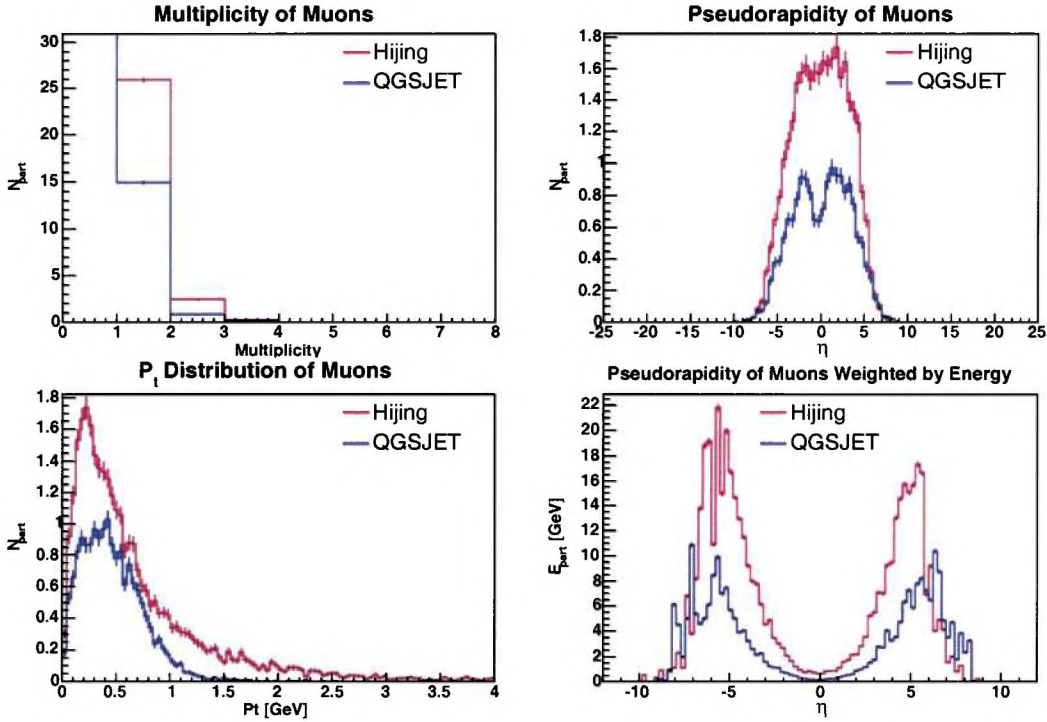
Figure 3.18: Results of generated collisions of pN at energy $\sqrt{s} = 37\,\text{TeV}$, muon distributions. Histograms are normalized to 1000 events. QGSJET-II does not produce muons and therefore it is not included in histograms.

3.7.3 Proton-Sulphur Collisions

In addition to proton-nitrogen collisions interactions of proton with heavier nuclei of sulphur $^{32}_{16}\text{S}$ were generated. Sulphur was chosen as nucleus with medium mass number. Similarly to other pA collisions, the sample of $350 \cdot 10^3$ minimum bias events were simulated by means of QGSJET, HIJING and QGSJET-II. Simulators were used with the same settings as described in Sec. 3.5. Inputs of QGSJET and QGSJET-II specify the incident and target particle (nucleus) as well as the energy of particle (nucleus) in the laboratory frame (see Subsecs. 3.3.2, 3.4.2). Proton was the incident particle with energy corresponding to the total *CMS* energy of the system $\sqrt{s} \approx 56\,\text{TeV}$. Four-momenta of stored secondary particles were transformed to the 'detector frame', in which proton has momentum $p_p = 7\,\text{TeV}$ and sulphur has momentum $p_S = 112\,\text{TeV}$. After transformation to the 'detector frame' the momentum of the incident sulphur nucleus had the same orientation as the z-axis (see Fig. B.1 in Appendix B).

Some results of simulations are very similar as for instance in the case of proton-nitrogen collisions, however spectra of the same particles are shown. Histograms
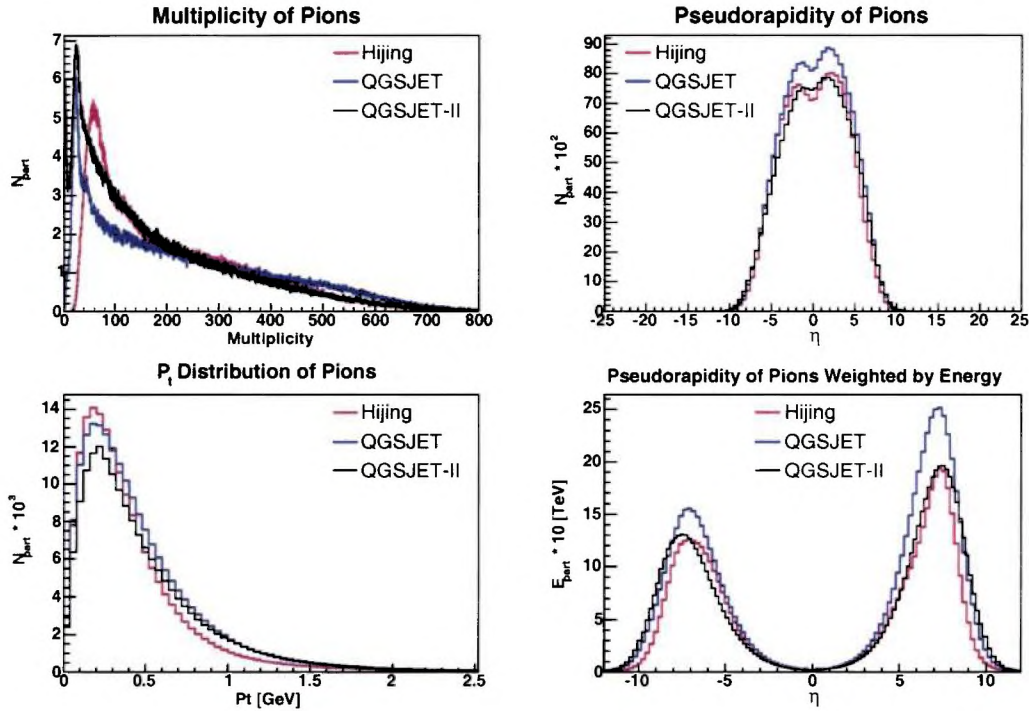
Figure 3.19: Results of generated collisions of pS at energy $\sqrt{s} = 56\,\text{TeV}$, charged pion distributions. Histograms are normalized to 1000 events.

are drawn with the same notation as in Sec.3.5. Pion variables which are drawn in Fig. 3.19 have similar characteristics as in the case of pN collisions. However, there are more charged pions, of course, as compared with previous simulations. Curves of multiplicity belonging to QGSJET and QGSJET-II are not so in accordance with each other in region with multiplicity > 300 as in histogram resulting from pN collisions (see Fig. 3.14). Nevertheless, QGSJET-II and HIJING produce very similar distributions of pion multiplicities in range of multiplicity > 100. The most prominent increase of secondary $\pi^\pm$ is in the central region, where HIJING and QGSJET-II give almost the same results for pseudorapidity distribution. Their pion production for pS collisions represent more than 50 % of pion production in pN interactions. QGSJET output data contain even more $\pi^\pm$ than other two generators. In contrast to other particles, pion rapidities weighted by energy have maximum for all simulators at almost the same pseudorapidity values. QGSJET and QGSJET-II produce almost the same pseudorapidity of charged pions weighted by energy in region with $|\eta| > 8$. They produce more energy carried by charged pions into very forward regions.

Results describing kaons are depicted in Appendix C in Fig. C.2. As can be seen in simulations described above, QGSJET-II produces most frequently no kaons, whereas HIJING and QGSJET give events with more than 70 $K^\pm$, in other words,
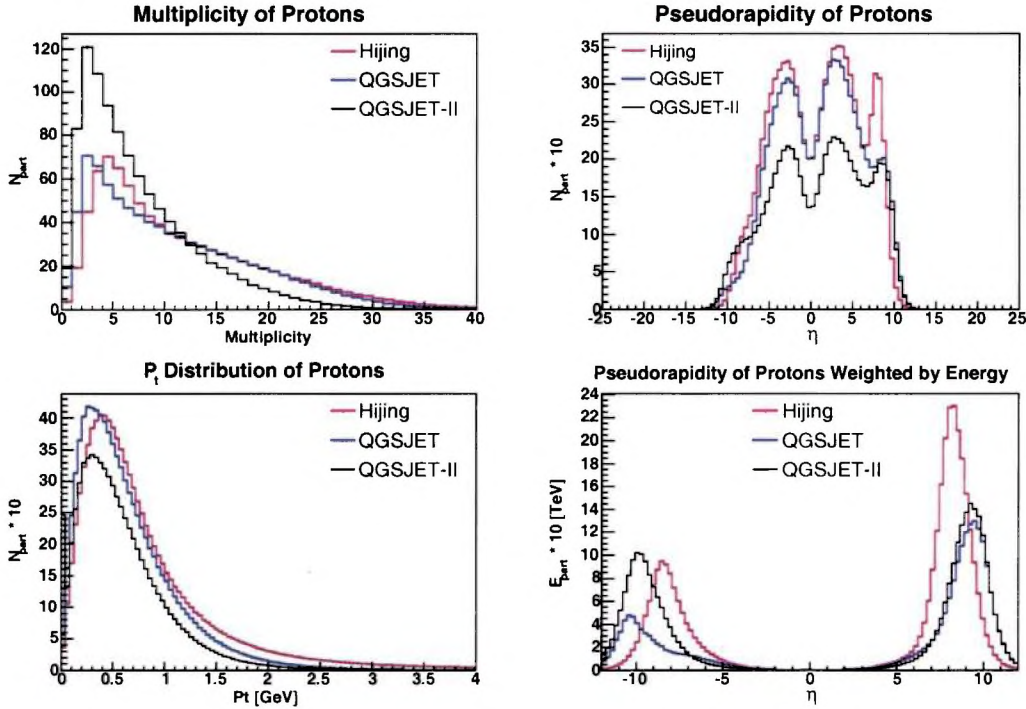
Figure 3.20: Results of generated collisions of pS at energy $\sqrt{s} = 56\,\text{TeV}$, proton histograms. Distributions are normalized to 1000 events.

beyond the maximum $K^{\pm}$ multiplicity limit of QGSJET-II. Except for the amount of charged kaons, all four histograms are in general similar to those of proton-nitrogen interactions. Differences in pseudorapidity distributions of kaons weighted by energy are not so substantial, energy weight compensates or does not increase differences in histograms.

Curves of proton multiplicities are shown in Fig. 3.20. HIJING and QGSJET give similar results and QGSJET-II differs in total multiplicity and also in the shape of curve. Pseudorapidity distributions are balanced for QGSJET and HIJING especially in central region. QGSJET-II has the bigger peak in the proton pseudorapidity weighted by energy in the direction of colliding proton. (the bottom right histogram). HIJING events contain the largest number of proton corresponding to fragments after nucleus disintegrations (the right peak in the upper right histogram in Fig. 3.20). Whereas QGSJET-II and HIJING produce protons with transverse momentum up to $p_{\perp} \approx 3\,\text{GeV}$, HIJING produces even protons with higher $p_{\perp}$ and its spectrum is relatively shifted to higher $p_{\perp}$. QGSJET and QGSJET-II again produce more energy into very forward regions.

Distributions of gammas are drawn in Appendix C in Fig. C.1. All three distributions of multiplicities meet at gamma multiplicity ≈ 300. Gamma production
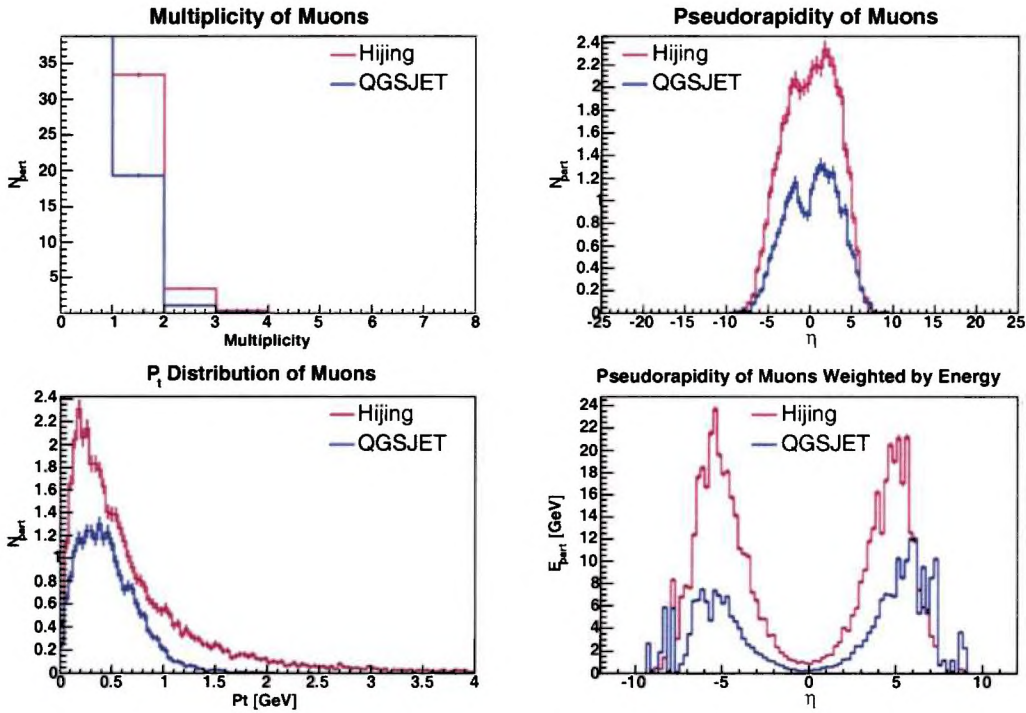
Figure 3.21: Results of generated collisions of pS at energy $\sqrt{s} = 56\,\text{TeV}$, muon distributions. Histograms are normalized to 1000 events. QGSJET-II is not included, it does not produce muons.

of QGSJET-II in central region represents only 70 % in comparison with amount of gammas produced by QGSJET, which is again the most productive. In spite of large differences in pseudorapidity distributions in the central region in QGSJET and QGSJET-II (see the upper right histogram), pseudorapidities weighted by energy in very forward regions are similar.

Fig. 3.21 shows four histograms of muon distributions. The total production of muons are higher than in previous collisions. Differences in production between HIJING and QGSJET are significant in all characteristics. QGSJET produces about 50 % of amount produced by HIJING. $p_{\perp}$ distribution of muons from HIJING are wider than corresponding one from QGSJET.
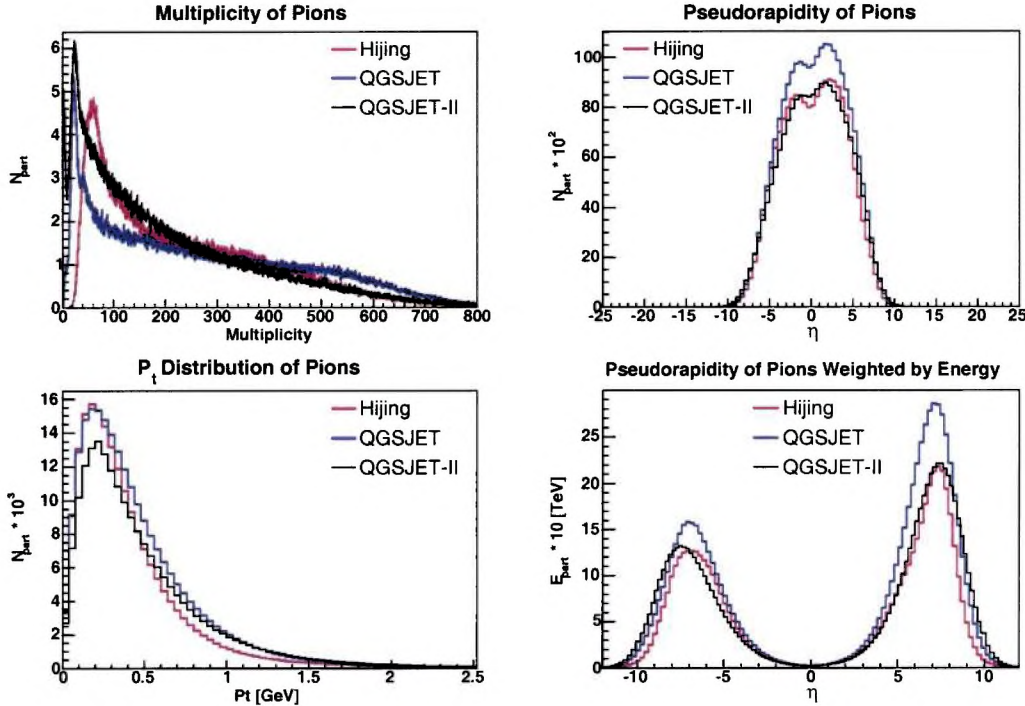
Figure 3.22: Results of generated collisions of pFe at energy $\sqrt{s} = 71\,\text{TeV}$, charged pion spectra. Histograms are normalized to 1000 events.

3.7.4   Proton-Iron Collisions

To compare differences among collisions of type pA with increasing mass number of the nucleus A iron $^{56}_{26}\text{Fe}$ was chosen as the heaviest nucleus. The upper limit of QGSJET for mass number of the colliding particle is 56. This feature is not a flaw, because of the characteristics of CR interactions. Type of these interactions is natural for simulations by QGSJET and CR interactions are caused by primary particle, which can be elementary particle or nucleus. The mass composition of cosmic rays is an object of many studies, but it is supposed, that there are no extremely energetic nuclei with mass number greater than 56, which corresponds to iron. Iron $^{56}_{26}\text{Fe}$ is the most stable nucleus at all. Nuclei with mass number significantly higher than 56 are not so stable to pass through Galaxy without decay into stable nuclei.

The *CMS* energy of the *pFe* interaction is $\sqrt{s} \approx 71\,\text{TeV}$ at LHC conditions provided that proton has momentum $p_p = 7\,\text{TeV}$ and iron $p_{Fe} = 182\,\text{TeV}$. According to *CMS* energy the energy of incident particles was set for QGSJET and QGSJET-II or the energy of nucleon-nucleon interaction in HIJING. Proton was the incident particle in events generated by QGSJET and QGSJET-II. All settings were identical with simulations described in Sec. 3.5 and $350 \cdot 10^3$ minimum bias events were generated.
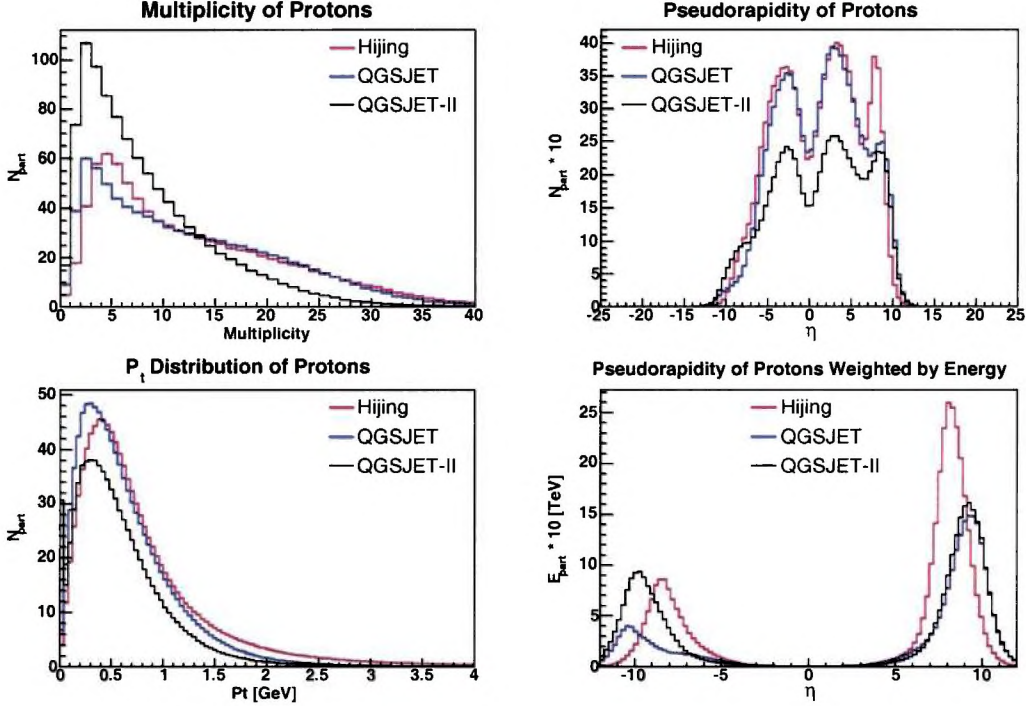
Figure 3.23: Results of generated collisions of pFe at energy $\sqrt{s} = 71\,\text{TeV}$, proton histograms. Distributions are normalized to 1000 events.

The resulting four-momenta of secondary particles were transformed to the specific 'detector frame', in which colliding particles have momenta in the direction of the z axis. In this frame proton has mentioned p_p momentum and iron has momentum p_{Fe} orientated same as the z axis (see Fig. B.1 in Appendix B). All histograms, which are drawn below are rescaled to 1000 events.

Four histograms describing pion production are drawn in Fig. 3.22. There are differences among generators in pion multiplicities up to 150 which are similar to the previous cases. Beside this region, there is another, in which differences start to appear in collisions of proton with heavier nucleus than nitrogen. QGSJET produces events which contain 400 – 700 pions more frequently than other simulators. It can be seen at first in pS interactions (see Fig. 3.19) and in pFe collisions it is more significant. The pion pseudorapidity distributions are very similar for QGSJET-II and HIJING. QGSJET produces relatively even more $\pi^\pm$ in comparison with other generators than in pS collisions (see the upper right histogram in Fig. 3.19). QGSJET-II and QGSJET produce more energetic pions than HIJING in very forward regions characterized by $|\eta| > 8$. Pseudorapidities of charged pions weighted by energy for QGSJET and QGSJET-II are again very similar in range $|\eta| > 8$.

Kaon histograms do not differ except for multiplicity from those of proton-sulphur
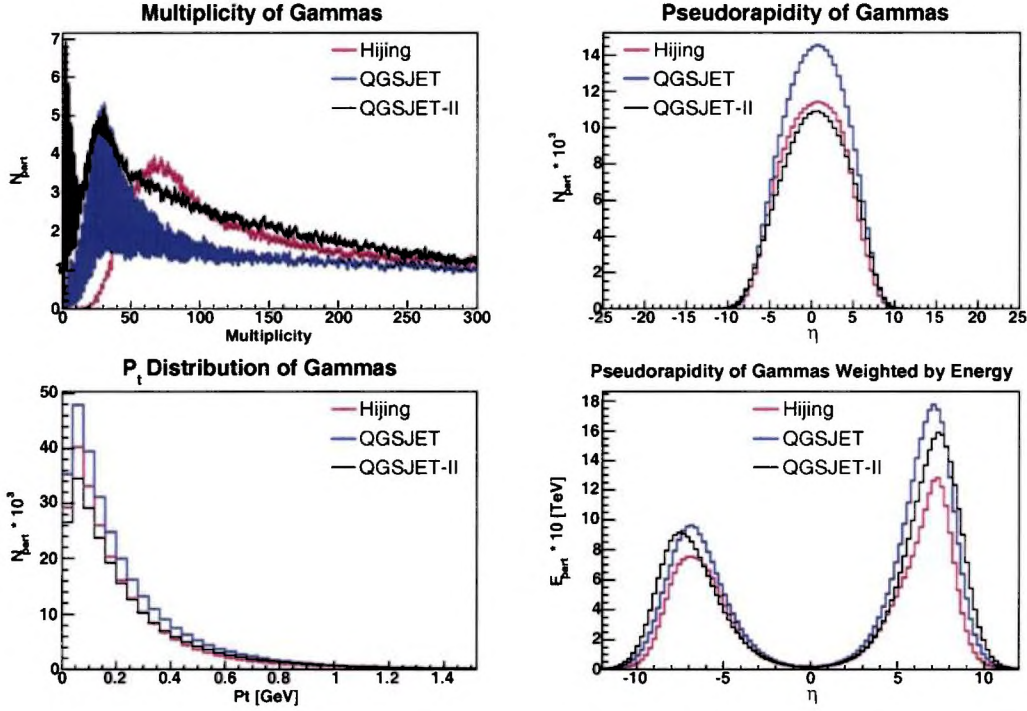
Figure 3.24: Results of generated collisions of pFe at energy $\sqrt{s} = 71\,\text{TeV}$, gamma spectra. Histograms are normalized to 1000 events.

interactions described above. Kaon distributions can be found in Appendix C in Fig. C.3. There are significant differentials among all generators which are caused mainly by the kaon multiplicity.

QGSJET and HIJING produce more events characterized by the proton multiplicities greater than 15 in comparison with QGSJET-II which generates most frequently events with up to 15 secondary protons in the output (see Fig. 3.23). Proton pseudorapidity histogram (the bottom left one in Fig. 3.23) shows that QGSJET-II gives different results in central region. HIJING has again the most remnants from nucleus, again. QGSJET-II and QGSJET generate energetic protons in the direction close to colliding axis more than HIJING. Especially QGSJET-II has peak with the mean value at $\eta \approx -10$ in pseudorapidity histogram weighted by energy (the bottom right one). There is also indication of such protons in pseudorapidity histogram. It signifies, that these protons are probably from interactions of low $p_\perp$ (but they are still denoted as inelastic) transfer which do not change distinctively the direction of the colliding protons.

Fig. 3.25 shows how HIJING differs from QGSJET in muon production. QGSJET produces approximately a half of the muon amount as compared with HIJING. More muons are emitted in the direction of the primary nucleus which is apparent from
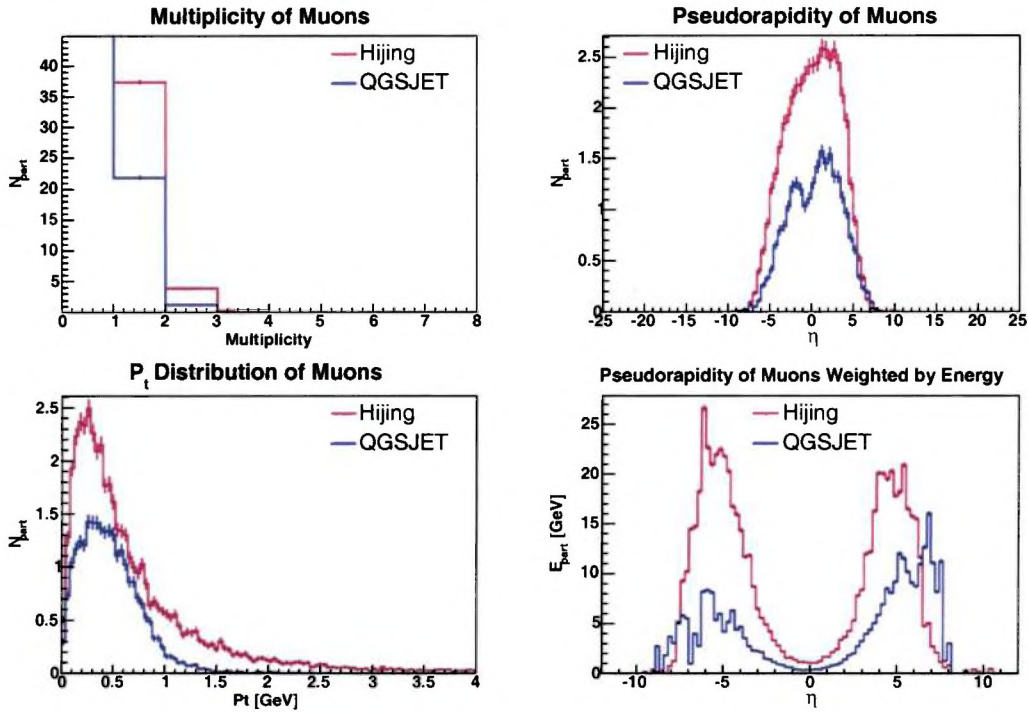
52

Figure 3.25: Results of generated collisions of pFe at energy $\sqrt{s} = 71\,\text{TeV}$, muon distributions. Histograms are normalized to 1000 events. QGSJET-II is not included in histograms, it does not produce muons.

pseudorapidity distribution histogram (the upper right one). On the other hand HIJING produces muons which are more energetic in the direction of the original colliding proton (compare right histograms in Fig. 3.25). $p_{\perp}$ distribution of HIJING is again wide than one corresponding to QGSJET. Muon production in HIJING with $p_{\perp} > 2\,\text{GeV}$ is non-negligible in contrast to muon distribution in QGSJET.
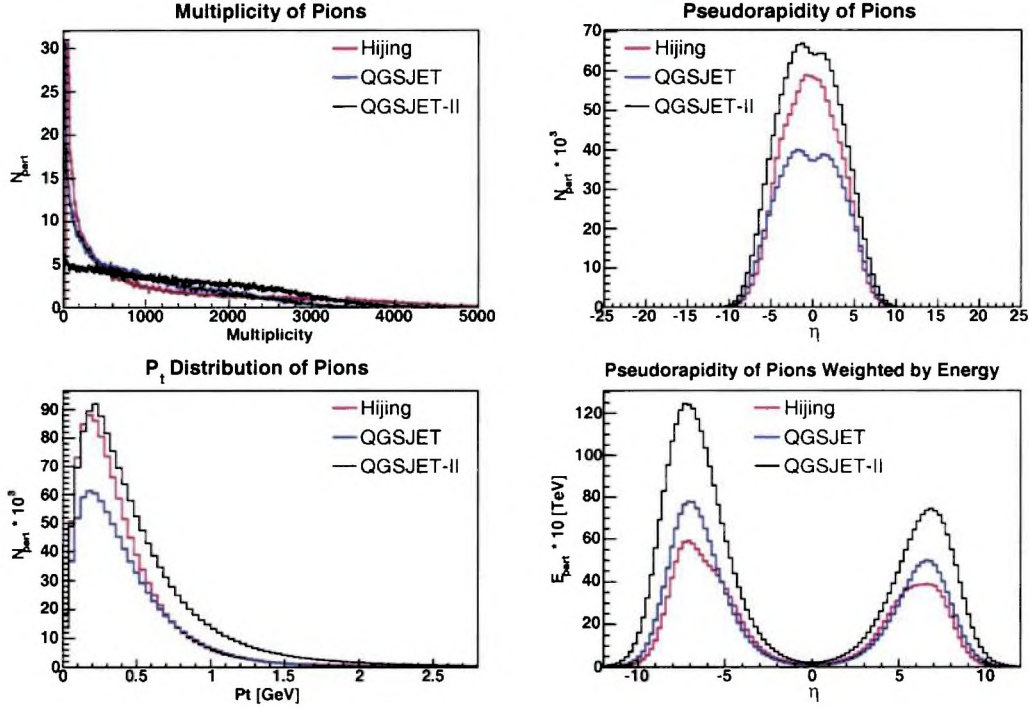
Figure 3.26: Results of generated collisions of NFe at energy $\sqrt{s} = 189\,\text{TeV}$, charged pion distributions. Histograms are normalized to 1000 events.

3.7.5 Nitrogen-Iron Collisions

In addition to proton-nucleus collisions also nucleus-nucleus interactions are interesting from point of view of CR physics. Nitrogen $^{14}_{7}\text{N}$ and iron $^{56}_{26}\text{Fe}$ are possible ones in CR physics. Iron and nitrogen can be accelerated at LHC to momentum $p_{Fe} = 182\,\text{TeV}$ and $p_N = 49\,\text{TeV}$, respectively. The *CMS* energy corresponding to collision of nitrogen and iron with momenta p_N and p_{Fe} is $\sqrt{s} \approx 189\,\text{TeV}$. Similarly to tests described above, resulting distributions of secondary particles were compared in the 'detector frame', in which incident nuclei have mentioned momenta p_{Fe} and p_N. Because of the vast number of produced secondary particles it was sufficient to generate 10^5 of minimum bias events with the same settings as in all previous simulations and as described in Sec. 3.5. Mainly QGSJET-II simulation is time-consuming operation and also particle output of such amount of events demands storage space of volume approximately 25 GB. Resulting histograms described below are drawn after transformation to the detector frame and the orientation of the incident nitrogen momentum was the same as orientation of the z axis (see Fig. B.1 in Appendix B).

Some distributions which differed only by total multiplicities in pA collisions changes the also shapes in AB collisions. The shape of multiplicity distributions
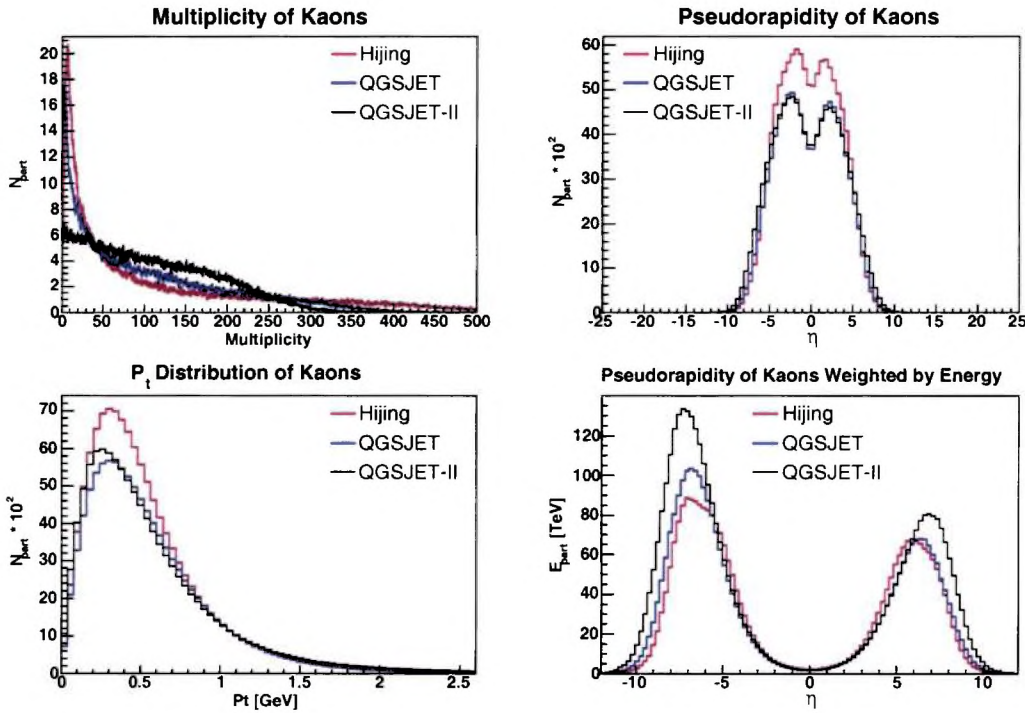
Figure 3.27: Results of generated collisions of NFe at energy $\sqrt{s} = 189\,\text{TeV}$, charged kaon histograms, which are normalized to 1000 events.

changes dramatically compared to pA collisions as described below.

Fig. 3.26 shows four histograms describing distributions of charged pions. They look very different from those, which originate from pA collisions. The upper left histogram of the pion multiplicity demonstrates differences between QGSJET-II and HIJING (QGSJET). The shape of QGSJET-II curve is quite flat in contrast to those of HIJING and QGSJET and also to the pion multiplicities in the cases of pA collisions. QGSJET-II produces the highest number of pions and therefore also the number of charged particles. HIJING differs from other generators by the shape of pseudorapidity distribution (see the upper right histogram in Fig. 3.26). The profile of its peak is narrow in the region of $|\eta| < 3$. QGSJET pion production in the central region represents approximately 60 % of the QGSJET-II production.

In spite of the very similar pseudorapidity distribution of kaons of QGSJET and QGSJET-II, their multiplicity is far from being equivalent (see Fig. 3.27). Whereas HIJING and QGSJET distributions decrease rapidly at lower multiplicities, QGSJET-II rate of events decreases in some range almost linearly. Multiplicities belonging to QGSJET and HIJING decrease in a similar way to QGSJET-II from multiplicities higher than 1000. Although HIJING has the highest number of secondary $K^{\pm}$, QGSJET-II produces more energetic charged kaons in regions with large pseudora-
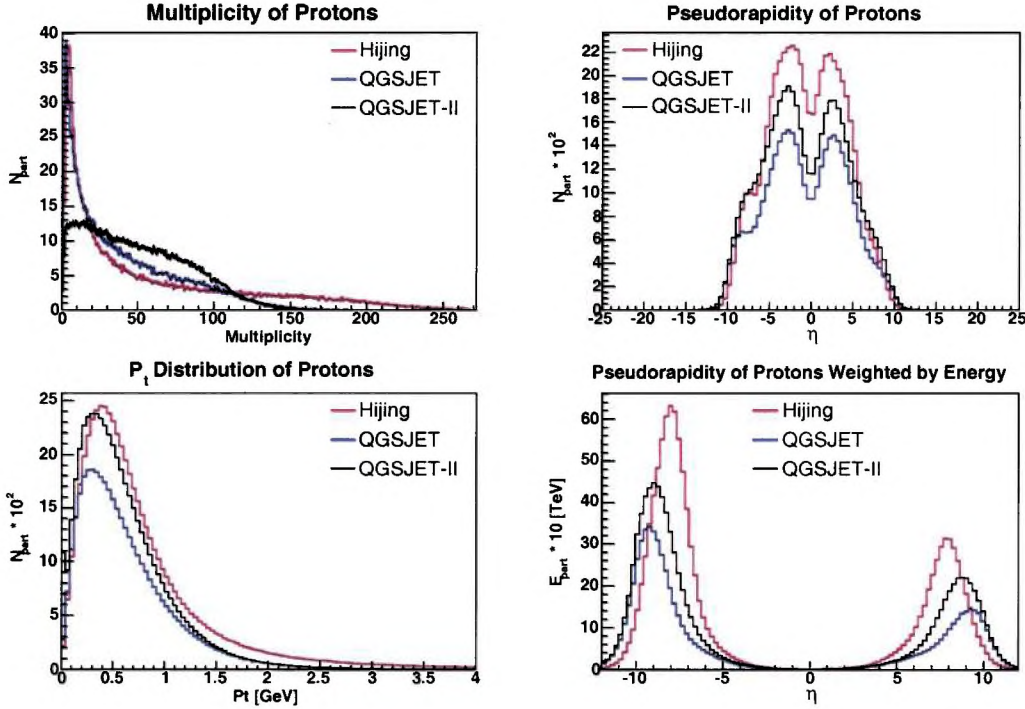
Figure 3.28: Results of generated collisions of NFe at energy $\sqrt{s} = 189\,\text{TeV}$, proton spectra. Histograms are normalized to 1000 events.

pidity.

Shapes of the multiplicity curves described in the case of kaons are similar to those of proton production except for total number of produced particles (see Fig. 3.28). Pseudorapidity distribution of protons shows differences between generators. HIJING produces the most protons, while QGSJET output contains approximately half of this amount in region with $|\eta| < 1$. The bottom right histogram shows again that QGSJET and QGSJET-II produce more energy into very forward regions.

The gamma distributions are in Fig. 3.29. QGSJET-II produces the highest number of produced gammas, which is evident from pseudorapidity distribution histogram (the upper right one). The shape of the peak in gamma distribution of HIJING is similar to that in the case of pion pseudorapidity distribution (see the upper right histogram in Fig. 3.26). QGSJET produces approximately 60 % of the amount of gammas produced by QGSJET-II and the shape of multiplicity is similar to gamma multiplicity of HIJING.

Fig. 3.30 shows muon distributions (QGSJET-II is not included, because it does not produce muons). Differences in total muon production between QGSJET and HIJING turn out to be the largest in nitrogen-iron collisions. The amount of muons produced by QGSJET represents approximately 40 % of number of muons contained

Figure 3.29: Results of generated collisions of NFe at energy $\sqrt{s} = 189\,\text{TeV}$, gamma distributions. Histograms are normalized to 1000 events.

in the HIJING output. Pseudorapidity of muons weighted by energy shows even larger discrepancies in range $3 < |\eta| < 6$. It is not so influenced by fluctuations as in previous collisions. Differences in $p_\perp$ distributions are similar to those in pA interactions. QGSJET does not almost produce muons characterized by $p_\perp > 1.5\,\text{GeV}$.

It is obvious from all pseudorapidity histograms weighted by energy, that QGSJET-II (and QGSJET) produce most energy in very forward regions. This conclusion coincides with pA simulations.
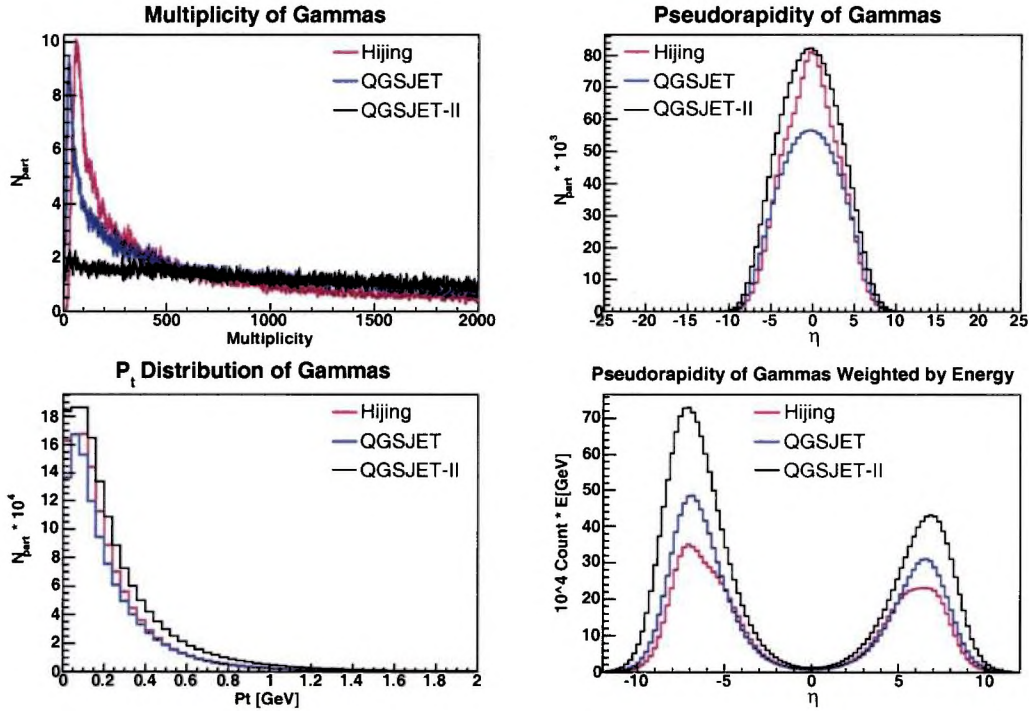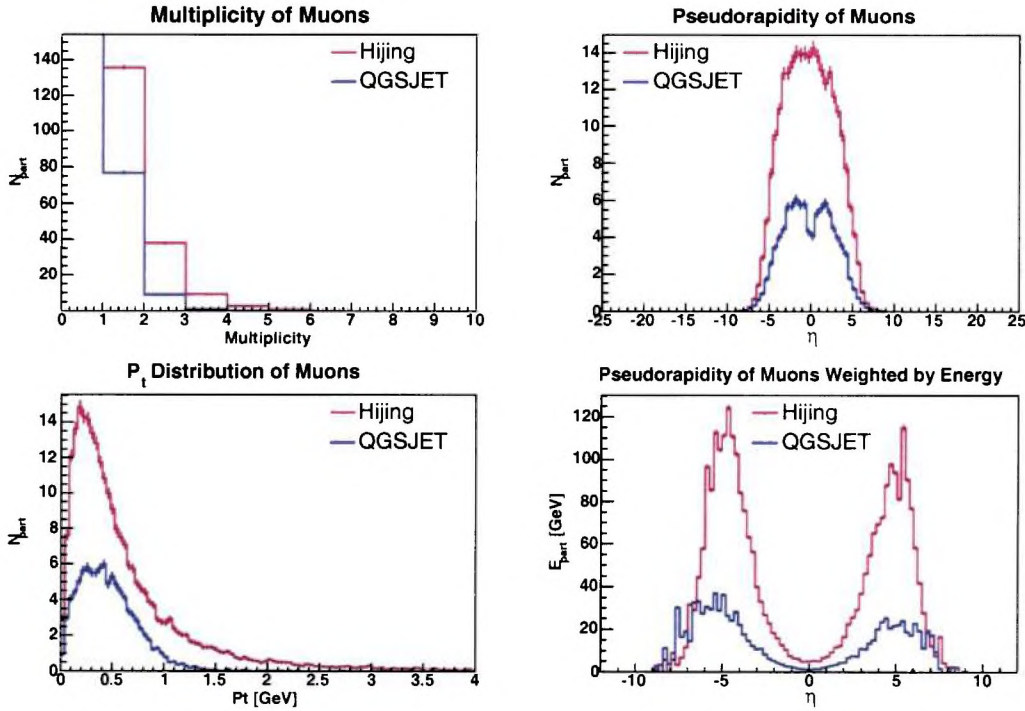
Figure 3.30: Results of generated collisions of NFe at energy $\sqrt{s} = 189$ TeV, muon histograms, which are normalized to 1000 events. QGSJET-II is not included, because it does not produce muons.

3.7.6   Test of Generators With All Processes Switched on

So far minimum bias events were generated with non-diffractive interactions were generated. Nevertheless some events produced by QGSJET-II were untypical (as compared to other generators) and similar to those of diffractive ones, but they were denoted by internal variables as inelastic collisions. In real experiment diffractive events can be found out by means of so called *rapidity gap*, which is the rapidity interval with no particle shower in calorimeter. It is useful to test generators with all relevant processes switched on, but with additional conditions which simulate the function of detector trigger. The conditions concern charged particles, which are easier to detect. At least one particle has to be in pseudorapidity interval of $0 < \eta < 3$ and one charged particle in region characterized by $-3 < \eta < 0$. Each of them has to have energy more than 2 GeV. All events which did not satisfy the conditions were excluded as diffractive ones.

To compare all four simulators, one has to generate proton-proton collisions. The *CMS* energy of *pp* collision is $\sqrt{s} = 14$ TeV at LHC condition as described in Subsec. 3.7.1. The same secondary particles were stored by which previous interactions were
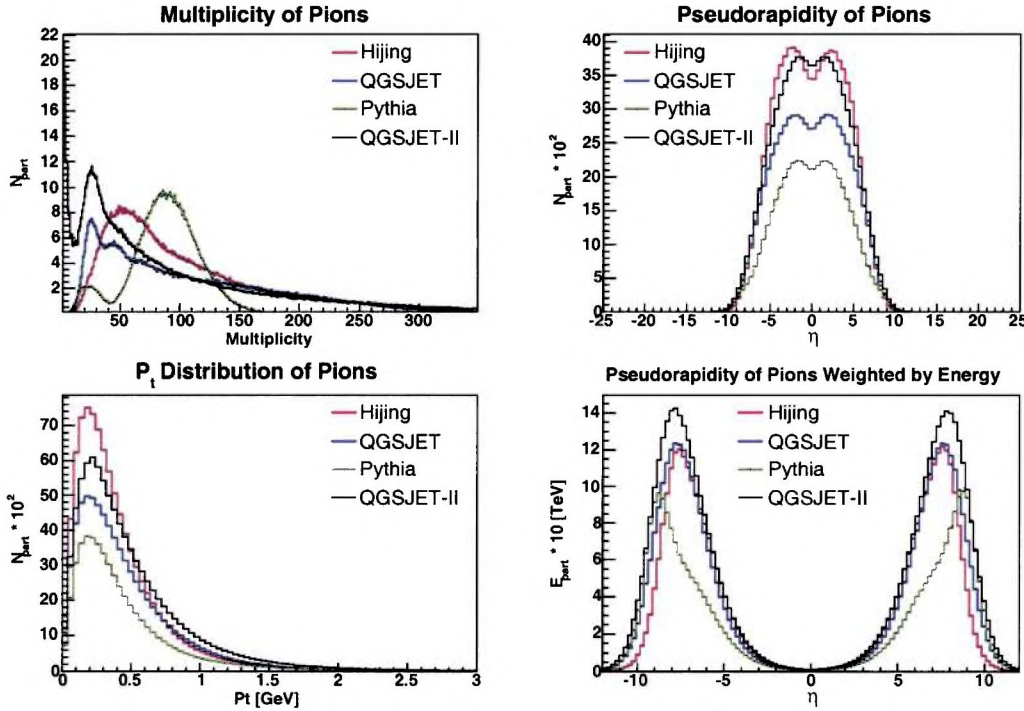
Figure 3.31: Resulting pion spectra from pp collisions at $\sqrt{s} = 14\,\text{TeV}$ with all processes switched on. Histograms are normalized to 1000 events.

described. Diffractive dissociation was switched on in HIJING and PYTHIA and of course diffractive events were not omitted in QGSJET and QGSJET-II. Beside single and double diffraction and minimum bias processes, which were used in previous interactions, there were another processes switched on in PYTHIA. These processes are contained in process groups: *open heavy production, closed heavy production, W/Z production, production of prompt photons* in PYTHIA. $5 \cdot 10^5$ events were generated. All Histograms shown below are normalized to 1000 events.

Fig. 3.31 shows pion distributions. It is obvious, that a large number of PYTHIA events did not satisfy the additional conditions on charged particles and therefore PYTHIA produced the smallest number of pions. Except for QGSJET-II which has the pion multiplicity curve very similar to simulations with diffraction switched off, the pion production of other generators starts at multiplicity equal to 10. QGSJET-II still produces non-negligible amount of events with small number of pions. All interactions have to satisfy the conditions on charged particles in mentioned pseudorapidity intervals. In means that even in collisions characterized by small number of secondary particles high $p_\perp$ has to be transferred. This interaction is call *hard diffraction*. Differences in pseudorapidity between QGSJET and QGSJET-II is more significant compared to pp minimum bias events (see the upper right histogram in
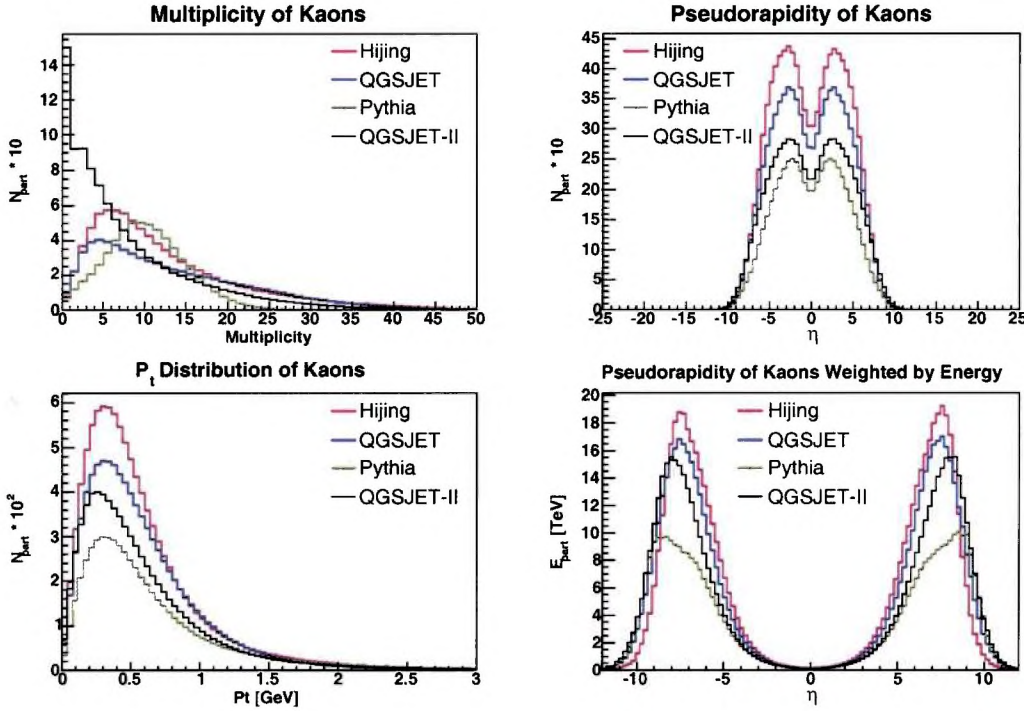
Figure 3.32: Resulting kaon distributions from pp collisions at $\sqrt{s} = 14\,\mathrm{TeV}$ with all processes switched on. Histograms are normalized to 1000 events.

Fig. 3.9). On the other hand QGSJET-II and HIJING produce similar pseudorapidity distributions, which are even more close to each other. PYTHIA has a little peak in multiplicity which can be caused by single diffractive dissociation. Other histograms show larger differences than in the case of minimum bias events. PYTHIA has very different shape of the pseudorapidity weighted by energy. In region $|\eta| < 9$ discrepancies can be incurred by the small multiplicity, in region $|\eta| > 9$ there is accordance between all generators.

Kaon histograms are drawn in Fig. 3.32. There are substantial differences in pseudorapidity distributions among all generators, although in minimum bias events QGSJET, PYTHIA and HIJING gave very similar results. PYTHIA produces the smallest number of $K^{\pm}$. QGSJET-II and HIJING have similar $K^{\pm}$ productions with those in case of pp minimum bias events. QGSJET and PYTHIA are more influenced by switching on diffraction processes and by conditions and they produce distinctively less $K^{\pm}$. Pseudorapidity distribution weighted by energy shows that QGSJET-II is not similar to PYTHIA as in case of minimum bias events of pp collisions (see the bottom right histogram in Fig. 3.10), but it is more close to distribution produced by HIJING and QGSJET.

Histograms in Fig. 3.33 illustrate proton characteristics. Except for QGSJET-
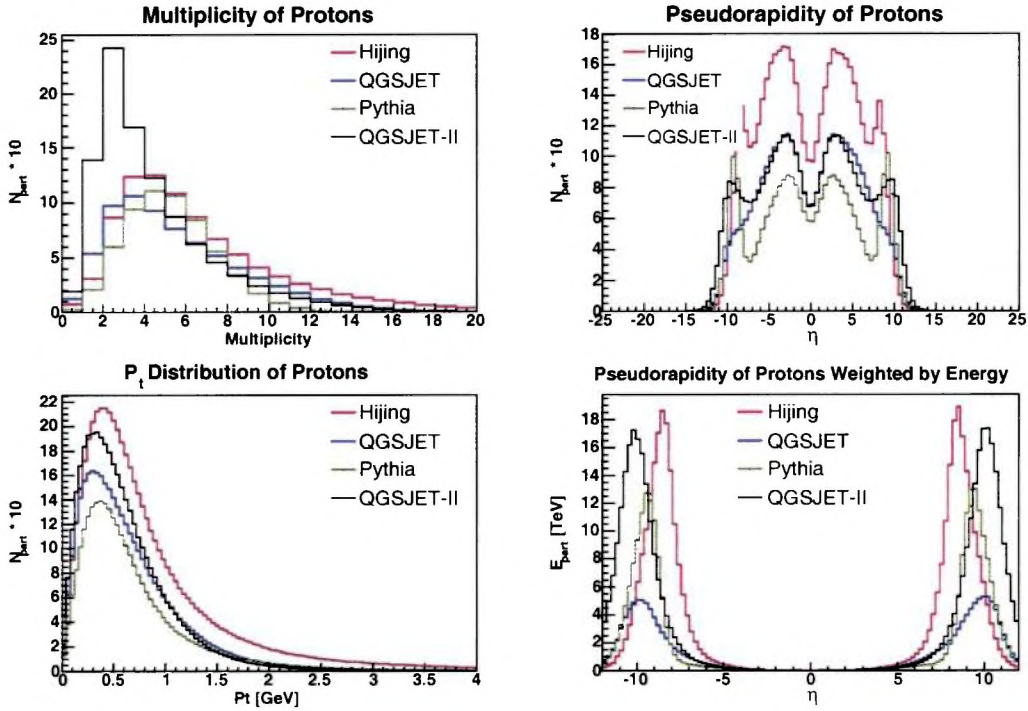
Figure 3.33: Resulting proton distributions from pp collisions at $\sqrt{s} = 14\,\text{TeV}$ with all processes switched on. Histograms are normalized 1000 events.

II, multiplicity histograms are similar, however, pseudorapidity distributions represent the essential property, in which dissimilarities can be observed. QGSJET and QGSJET-II have almost the same pseudorapidity distributions in interval $|\eta| < 6$. QGSJET-II events contain the highest amount of protons in pseudorapidity region $|\eta| > 10$ and they are so energetic that energy weights even increase differences to other simulators and therefore QGSJET-II produce most energy carried by protons in mentioned pseudorapidity range. HIJING produces non-negligible amount of protons with $p_\perp > 2.5$, whereas other generators does not.

Fig. 3.34 describes gamma distributions. Even in gamma pseudorapidity distribution (the upper right histogram) discrepancies among generators have increased because of switching on all processes and due to the mentioned conditions. Similarly to the previous histograms, PYTHIA has the smallest gamma production. Differences between HIJING and QGSJET in pseudorapidity distribution are not so large as in the case of minimum bias events of pp collisions (see the upper right histogram in Fig 3.12).

Muon distributions are shown in Fig. 3.35. Muon production does not dramatically differ from results in Subsec. 3.7.1. PYTHIA produces smaller number of muons than HIJING. QGSJET events contain less than half of muons seen in HIJING events

Figure 3.34: Resulting gamma spectra from pp collisions at $\sqrt{s} = 14\,\mathrm{TeV}$ with all processes switched on. Histograms are normalized to 1000 events.

which represents larger difference than in histogram from pp minimum bias collisions (see the upper right histogram in Fig. 3.13).

As apparent from all histograms depicted above, individual generators approach to diffractive dissociation in very different way, which causes large dissimilarities among generators. Apparently authors use different definitions of diffractive events.
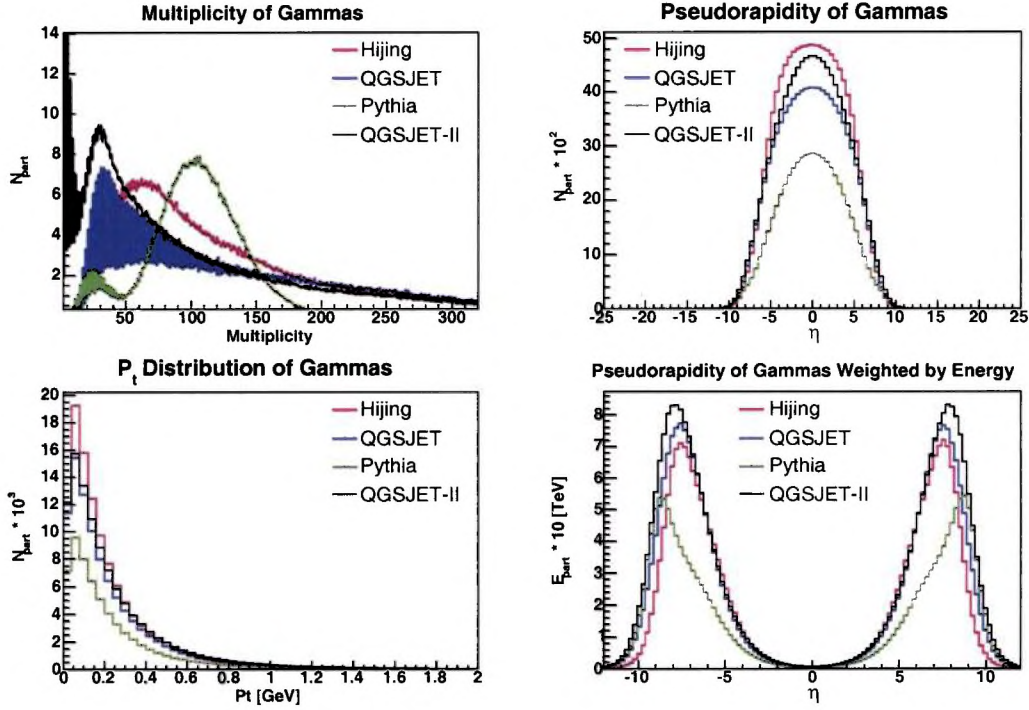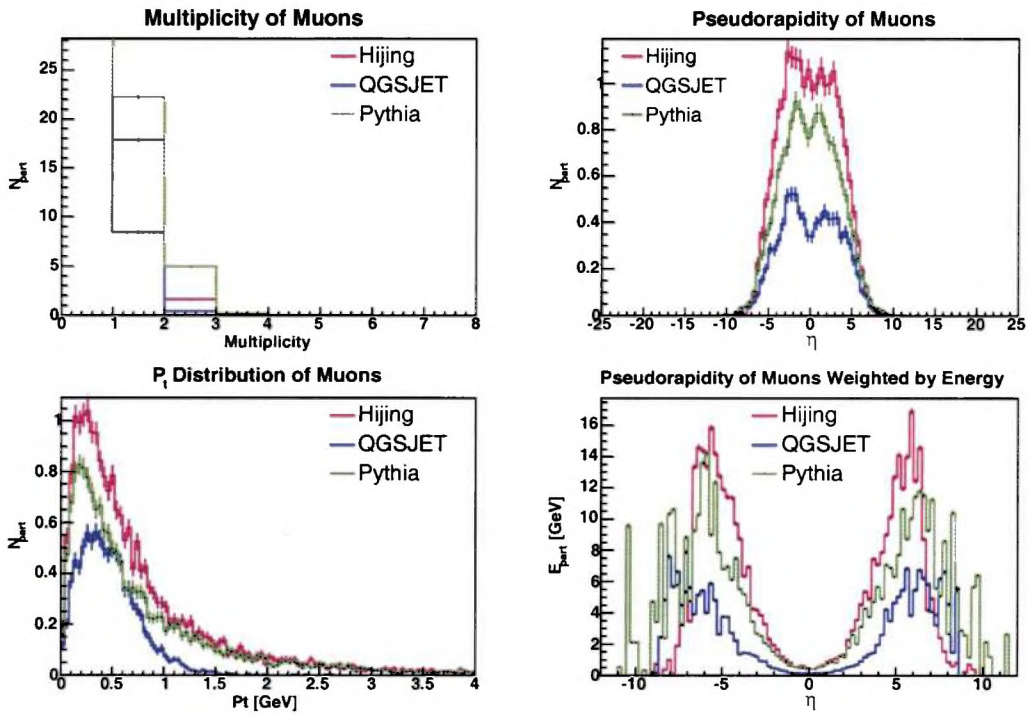
Figure 3.35: Resulting muon histograms from pp collisions at $\sqrt{s} = 14\,\text{TeV}$ with all processes switched on. Histograms are normalized to 1000 events.

Chapter 4

The ATLAS Experiment

4.1 The ATLAS Detector Description

The ATLAS detector is designed to study proton-proton collisions at the LHC accelerator at 14 TeV in *CMS*. In Fig. 4.1 the ATLAS detector is shown, there are three subsystems: inner tracker system, electromagnetic and hadronic calorimeters and full coverage muon detection. Detectors which are closest to the interaction point, inner tracker system, consist of 3 types of detectors: finely segmented silicon pixel detector, semiconductor tracker and the transition radiation tracker [64]. The segmentation is optimized for proton-proton collisions at design machine luminosity $(10^{34} \, cm^{-2}s^{-1})$.

To perform the primary goal of the experiment, to operate at such high luminosity, the precision measurements is required. High precision measurements are demanded especially around the vertex where the very large track density is expected at the LHC. Therefore the momentum and spatial resolution are needed for these goals. The inner detector is designed for such purposes. Semiconductor tracking detectors are the closest to the vertex and there are used silicon microstrip and pixel technologies. The highest granularity is achieved around the vertex region using semiconductor pixel detectors. The continuous track-following is provided by the transition radiation tracker based on the use of straw detectors. The overall inner detector provides full tracking coverage over $|\eta| < 2.5$.

The calorimetry consists of an electromagnetic (EM) and hadronic sections and the whole calorimeter system covers pseudorapidity region $|\eta| < 4.9$. All EM calorimeter parts can cover pseudorapidity region of $|\eta| < 3.2$. They can be divided into a barrel part with coverage $|\eta| < 1.475$ and two end-caps located in pseudorapidity region $1.375 < |\eta| < 3.2$. The EM calorimeter is a copper LAr detector with accordion geometry, which provides complete ϕ symmetry without azimuthal cracks. The EM calorimeter is finely segmented both longitudinally and transversally. There are three longitudinal sections. The first, so called strip section consists of narrow strips with granularity of $\Delta\eta \times \Delta\phi = 0.003 \times 0.1$ in the barrel part, while strips are slightly coarser in the end-caps. The middle section is composed of square towers of size $\Delta\eta \times \Delta\phi = 0.025 \times 0.025$. The back section has a granularity of $\Delta\eta \times \Delta\phi = 0.05 \times 0.025$.
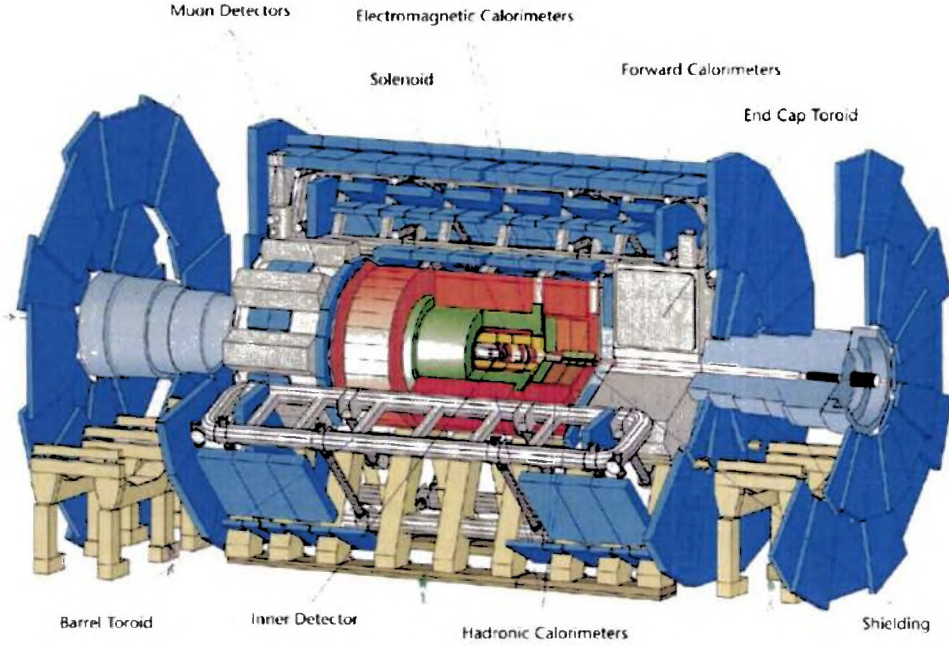
Figure 4.1: Overall layout of the ATLAS detector, taken from [65].

In addition a finely segmented presampler system with granularity $\Delta\eta \times \Delta\phi = 0.025 \times 0.1$ and coverage $|\eta| < 1.52$ is located in front of the EM calorimeter. The energy resolution of EM calorimeter was determined experimentally as $10\%/\sqrt{E} \oplus 0.7\%$.

The ATLAS hadronic calorimeters can be roughly divided into three parts: barrel calorimeter covering $|\eta| < 1.7$, hadronic end-caps calorimeters covering $1.5 < |\eta| < 3.2$ and forward calorimeters, which provide measurement in pseudorapidity region $3.1 < |\eta| < 4.9$. Different techniques are used to suit best to wide requirements. The barrel calorimeter is a sampling type, it uses iron as the absorber and scintillating tiles play a role of active material. The tiles are placed radially and staggered in depth. Wavelength shifting fibres are used to read out signals from scintillating tiles into separate photomultipliers. The hadronic calorimeter is longitudinally segmented in three layers. The granularity in the first and middle layer is $\Delta\eta \times \Delta\phi = 0.1 \times 0.1$ and 0.2×0.1 in the last layer. Hadronic end-cap calorimeters and forward calorimeters are liquid-argon ones to achieve radiation hardness. Granularity of end-cap calorimeters is 0.1×0.1 in pseudorapidity interval $1.5 < |\eta| < 2.5$ and 0.2×0.2 in $2.5 < |\eta| < 3.2$. Granularity of forward calorimeters is 0.2×0.2. The energy resolution of the hadronic calorimeters is roughly $50\%/\sqrt{\text{GeV}} \oplus 3\%$ for $|\eta| < 3$ and $100\%/\sqrt{\text{GeV}} \oplus 10\%$ for pseudorapidity region $3 < |\eta| < 5$.

ATLAS muon spectrometers are located behind the calorimeters in order to be shielded from hadronic showers. The muon spectrometer is based on the magnetic deflection of muon tracks in the large superconducting air-core toroid magnets. Several technologies for tracking devices are used. Over most of the η-range, a precision measurement is assured by the monitored drift tubes. At large pseudorapidities and close to the interaction point, cathode strip chambers with higher granularity are used in the innermost plane over $2 < |\eta| < 2.7$. There are barrel and end-cap chambers. Barrel chambers are arranged in the three cylindrical layers around the beam axis. The barrel chambers cover pseudorapidity region of $|\eta| < 1$. In the end-cap regions, three layers of chambers are installed vertically, which cover the range $1 < |\eta| < 2.7$. Muon system allows the reconstruction of high energy muons with $p_\perp$ from 6 GeV up to the limit of the muon spectrometer ($p_\perp \approx 2$ TeV). Muons with $p_\perp$ below 6 GeV can be efficiently identified and measured combining the inner detector track reconstruction with the energy available in calorimeters [64]. Muon $p_\perp$ momentum resolution is of the order of 2 % for muons with transversal momentum 3 GeV $< p_\perp < 100$ GeV using combination of muon spectrometer and inner detector. The resolution of muon spectrometer alone decreases from 8 % for muons with $p_\perp = 3$ GeV to 4 % for muons with $p_\perp = 10$ GeV. For higher $p_\perp$ muons the resolution is almost constant up to $p_\perp = 100$ GeV and then it increases.

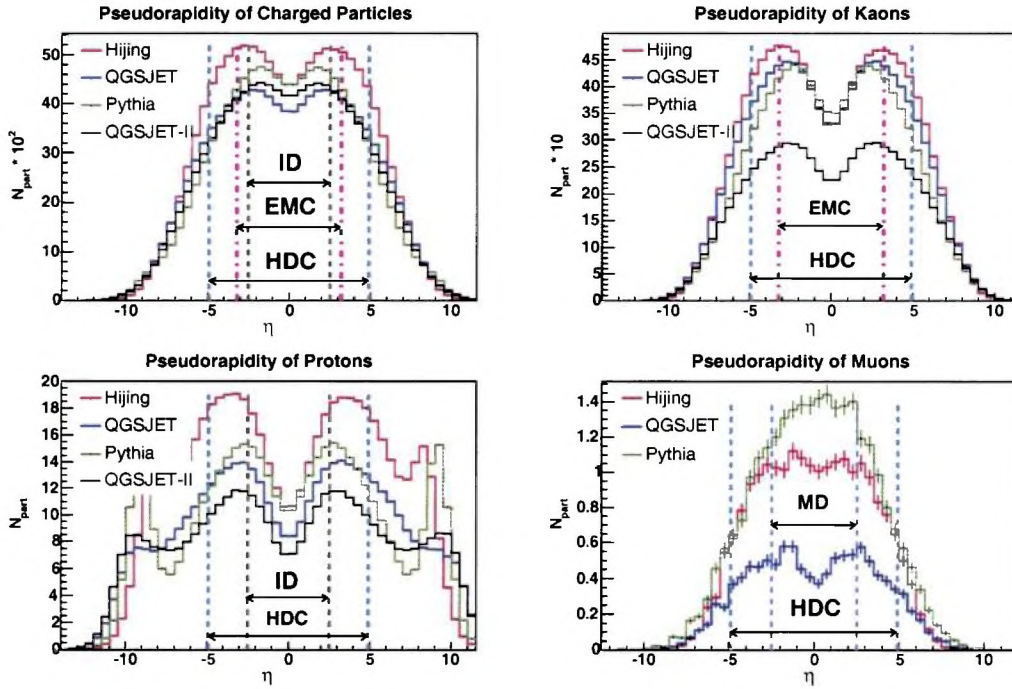Figure 4.2: Resulting histograms from *pp* collision at energy $\sqrt{s} = 14\,\text{TeV}$, pseudo-rapidity coverage of detectors are drawn by dashed lines. *HDC*, *EMC*, *MD* and *ID* denote hadronic and electromagnetic calorimeter, muon detectors and inner detector, respectively. Histograms are normalized to 1000 events.

4.2 Differences Observable by The ATLAS

To demonstrate, in which parts of the ATLAS differences among generators are in principle observable, the pseudorapidity coverage by particular detectors were used. Cuts of overall pseudorapidity coverage of hadronic calorimeter (HDC), electromagnetic calorimeter (EMC), muon detectors (MD) and inner detector (ID) are applied to simulations from Sec. 3.7.

Fig. 4.2 shows how much generators differ from each other in predictions of *pp* collisions at $\sqrt{s} = 14\,\text{TeV}$. There are no large differences in pseudorapidity distribution of pions among all generators. Pions represent the vast amount of all charged particles. Distribution of charged particles according to their pseudorapidity are drawn in the upper left histogram in Fig. 4.2. Differences between PYTHIA (HIJING) and QGSJET is of the order of 15 % in the central region.

QGSJET-II gives $K^{\pm}$ production at level of 70 % in comparison with other generators, which all give almost the same pseudorapidity distribution. It is in principle to distinguish between QGSJET-II and other generators, but it is very difficult to

Figure 4.3: Resulting histograms from pN collision at energy $\sqrt{s} = 37\,\text{TeV}$, pseudo-rapidity coverage of detectors are drawn by dashed lines. *HDC, EMC, MD* and *ID* denote hadronic and electromagnetic calorimeter, muon detectors and inner detector, respectively. Histograms are normalized to 1000 events.

measure the total distribution of $K^{\pm}$.

According to the number of secondary protons in central calorimeter one can distinguish between HIJING (PYTHIA), QGSJET and QGSJET-II (see the bottom left histogram). PYTHIA and QGSJET have very similar distribution of protons in the region of forward hadronic calorimeters ($3.1 < |\eta| < 4.9$) and differ from HIJING and QGSJET-II, but this region is out of the inner detector coverage.

The bottom right histogram shows the most apparent discrepancies, which concerns pseudorapidity distribution of muons. They would be observable in muon detectors. Muons are the best for testing generators because of large differences among all generators over the whole coverage of muon detectors and because the ATLAS detector is designed for muon detection. PYTHIA gives more than about double amount of muons as compared with QGSJET.

Simulations of pN collisions showed little differences in pion distribution and therefore even in charged particle distribution among generators (Subsec. 3.7.2). The differences are visible in pseudorapidity distribution of antiprotons, kaons, protons and muons. In the latter case energy was used as weight (see Fig. 4.3). Protons
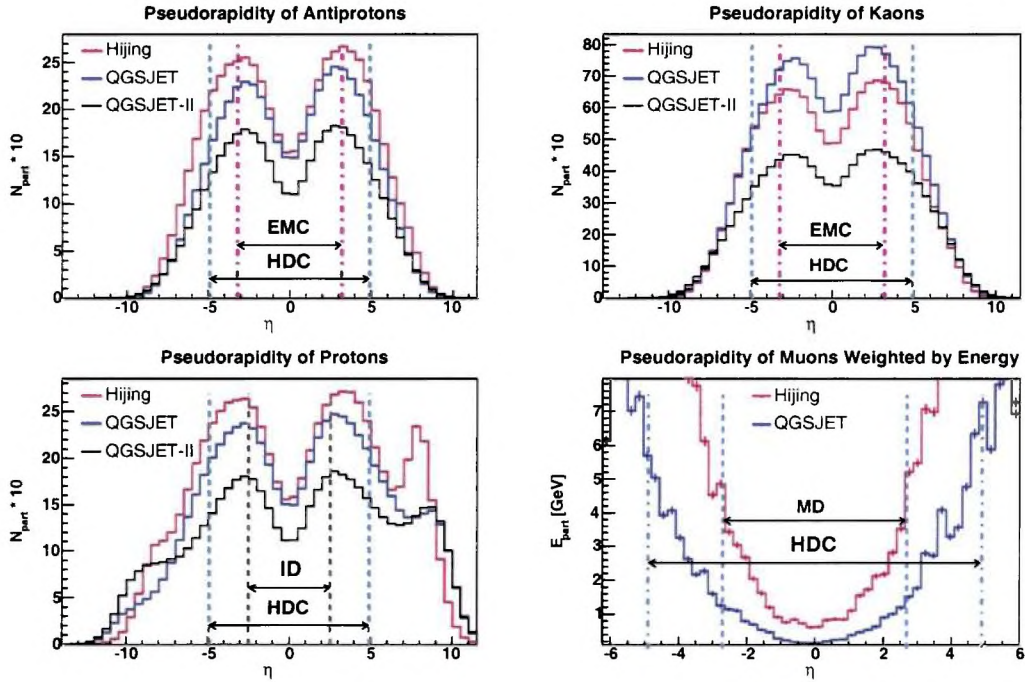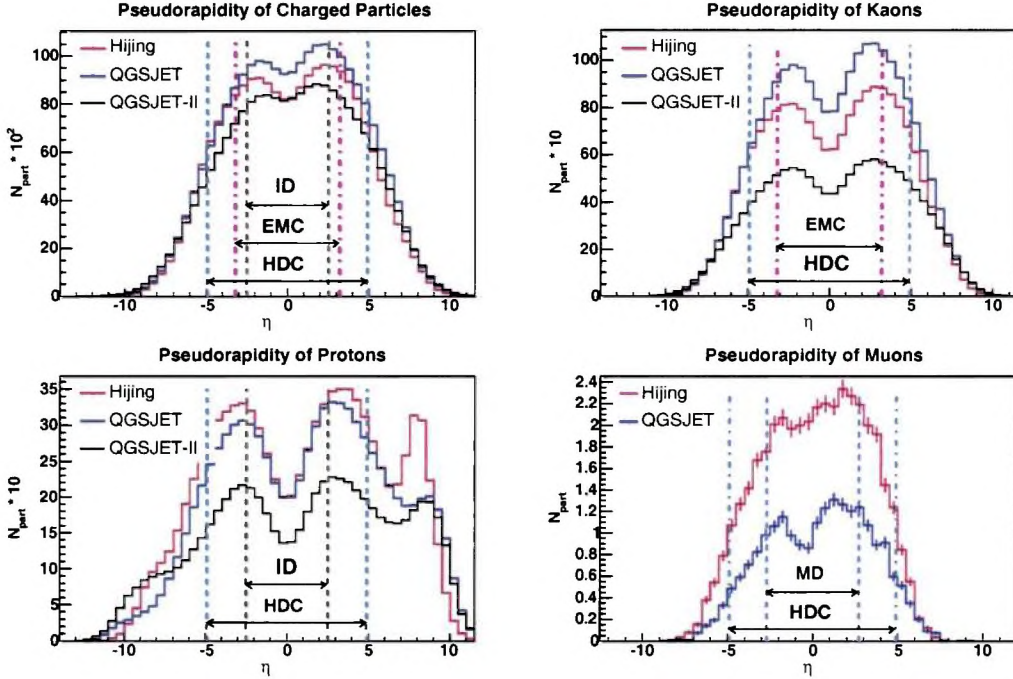
Figure 4.4: Resulting histograms from pS collision at energy $\sqrt{s} = 56\,\text{TeV}$, pseudo-rapidity coverage of detectors are drawn by dashed lines. *HDC, EMC, MD* and *ID* denote hadronic and electromagnetic calorimeter, muon detectors and inner detector, respectively. Histograms are normalized to 1000 events.

and antiprotons produced by HIJING and QGSJET turn out to be distributed very similarly in the central region of hadronic calorimeter, however QGSJET-II gives approximately 70 % of the multiplicity of the other simulators. $mu^{\pm}$ production together with muon pseudorapidity distribution weighted by energy seem to be the best for finding generator which approximates best results from interaction. Significant differences can be found also in pseudorapidity distribution of $K^{\pm}$, but total $K^{\pm}$ multiplicity is nearly indeterminable due to total number of particles and their energy produced in interaction.

Different curves of charged particle pseudorapidity distribution appear in results of pS collisions (the upper left histogram in Fig. 4.4). There is region outside the center of the hadronic calorimeter, which is covered by endcaps ($1.5 < |\eta| < 3.2$), where differences are observable in the order of 10 %. Similarly to the results from pN interactions, pseudorapidity distribution of kaons exhibits strong dependence on used generator in almost the whole range of the ATLAS calorimeters (and of course inner detector, too). Pseudorapidity distribution of protons enables to distinguish between QGSJET (HIJING) and QGSJET-II in central region of hadronic calorimeter. Muons
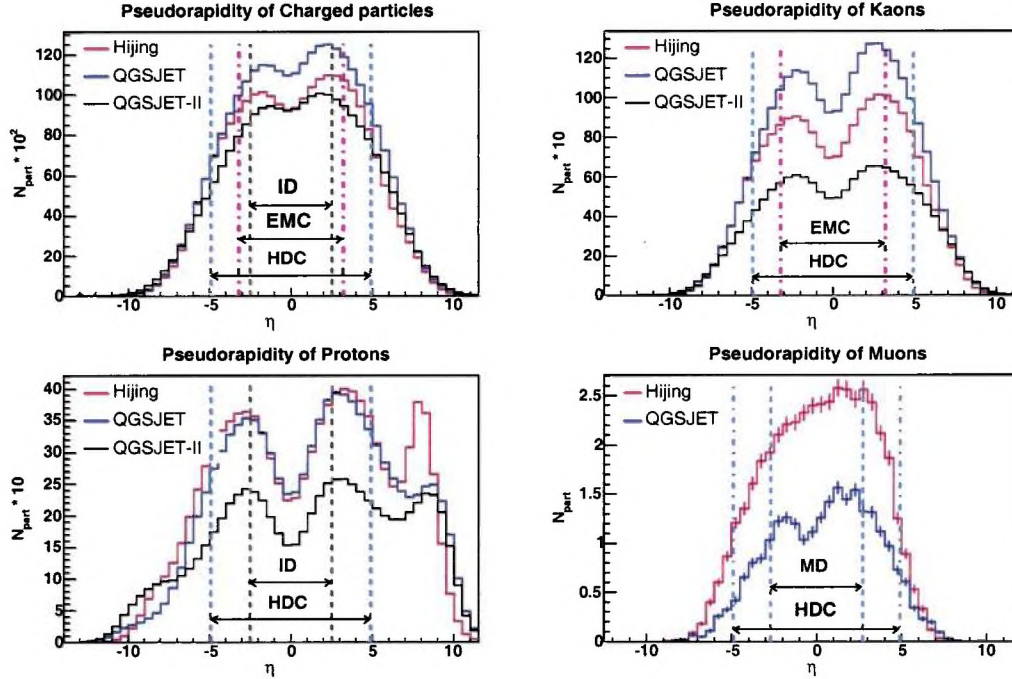
Figure 4.5: Resulting histograms from pFe collision at energy $\sqrt{s} = 71\,\mathrm{TeV}$, pseudorapidity coverage of detectors are drawn by dashed lines. *HDC, EMC, MD* and *ID* denote hadronic and electromagnetic calorimeter, muon detectors and inner detector, respectively. Histograms are normalized to 1000 events.

are again optimal for finding the large discrepancies in generator results (the bottom right histogram in Fig. 4.4).

Fig. 4.5 shows pseudorapidity cuts in four histograms, which come out from results of pFe collisions. Charged particles (the upper left histogram) are distributed similarly to the previous case. The central region seems to be occupied equally in case of HIJING and QGSJET-II, whereas QGSJET produced approximately 20 % more charged particles in the range covered by barrel ($|\eta| < 1.7$). Regarding forward calorimeters, it is possible to find differences only in the direction of primary iron momentum ($|\eta| > 0$). Curves of pseudorapidity distributions of protons from HIJING and QGSJET are even more similar than in pS collisions, but QGSJET-II gives much smaller multiplicity. Muons and kaons are still particles, where production is strongly generator dependent and thus give the best opportunity to differentiate among them.

Pseudorapidity cuts in resulting histograms from NFe collisions are drawn in Fig. 4.6. Larger differences among all generators than in previous cases are observable in charge particle pseudorapidity distribution (see the upper left histogram). Therefore detection of charge particle productions is now very convenient to compare generators
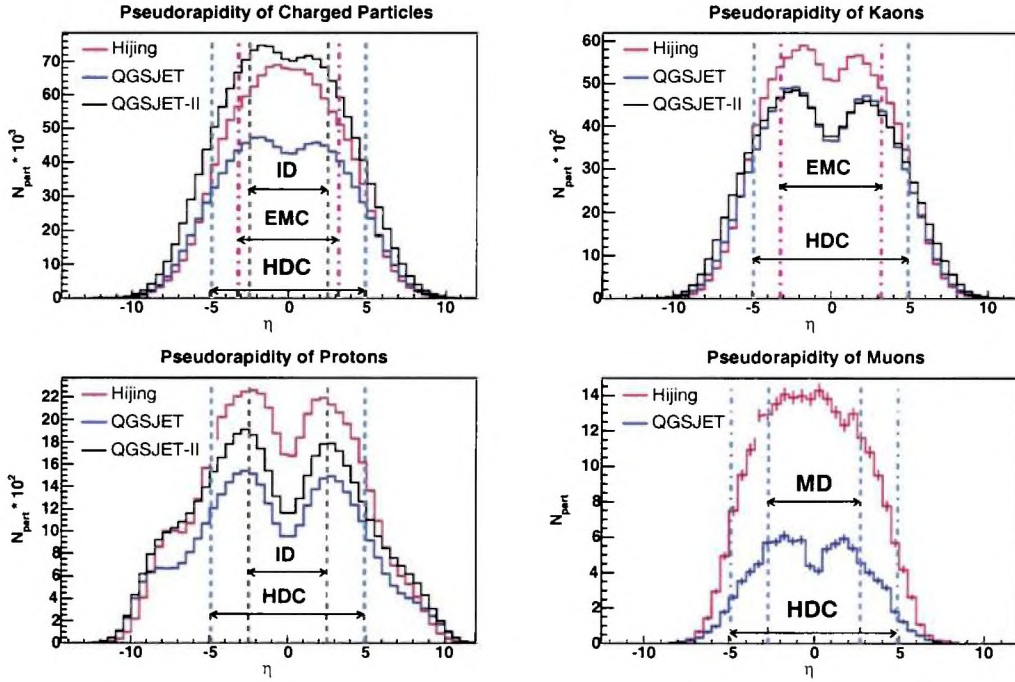
Figure 4.6: Resulting distributions from NFe collision at energy $\sqrt{s} = 189\,\text{TeV}$, pseudorapidity coverage of detectors are drawn by dashed lines. *HDC, EMC, MD* and *ID* denote hadronic and electromagnetic calorimeter, muon detectors and inner detector, respectively. Histograms are normalized to 1000 events.

with measured data. Charged particle production in QGSJET in the central region represents only 60 % of charged particle produced by QGSJET-II. In contrast to previous case, QGSJET and QGSJET-II have very similar pseudorapidity distribution of kaons in range covered by calorimeters and HIJING are more productive. Detection of protons would distinguish all generators. Production of muons and their pseudorapidity distribution are still the best for comparison of real data with simulations. Muon production in HIJING differ from number of muons produced by QGSJET by a factor ≈ 2 or more in all range covered by hadronic calorimeter (see the bottom right histogram).

Chapter 5

Conclusions

Four Monte Carlo generators: PYTHIA, HIJING, QGSJET and QGSJET-II have been tested at Tevatron and LHC energy regions. Different colliding particles were used in simulation of $\bar{p}p$, pp, pN, pS, NFe minimum bias events. The generators were compared regarding production of $\pi^{\pm}$, $K^{\pm}$, p, $\bar{p}$, γ, $\mu^{\pm}$.

Each model treats diffraction differently. In order to test generators in as far as possible similar conditions with mainly hard processes, which are the most important for events detectable in accelerator detectors, diffraction was switched off. Minimum bias events comprehend hard processes with low-p_t production without diffraction and elastic scattering.

Collisions with both diffraction dissociation and hard processes switched on were also generated with additional conditions playing role of the trigger detector. The aim was again to test models at same conditions, however, this time with all processes included.

Histograms resulting from test at Tevatron energy can be found in Sec. 3.5, Sec. 3.6 contains results of charm production test and resulting distributions from collisions simulated at LHC energies are drawn in Sec. 3.7. Tables with the mean values of multiplicities, energy distributions and $p_{\perp}$ distributions of $\pi^{\pm}$, $K^{\pm}$, $\mu^{\pm}$ and p are in Appendix B. Tab. B.1 contains the mentioned mean values of $\pi^{\pm}$, Tabs. B.2, B.3, B.4 contains the mean values of $K^{\pm}$, $\mu^{\pm}$ and p distributions.

Pseudorapidity distributions of pions corresponding to QGSJET, QGSJET-II and HIJING (PYTHIA) differ from each other even at Tevatron energy (see Fig. 3.3). On the other hand, QGSJET is able to successfully reproduce the CR data at this energy. The discrepancies between HIJING (PYTHIA) and QGSJET (QGSJET-II) are caused by pions with low energy, which are emitted into pseudorapidity region $|\eta| < 3$. From the point of view of the shower development, such pions do not play important role. The most important hadrons for the purposes of CR physics are very energetic particles emitted longitudinally with respect to the direction of the shower. Pseudorapidity of pions weighted by energy (the bottom right histogram in Fig. 3.3) shows good accordance among all generators in pseudorapidity regions covered by detectors.

Simulations at LHC energies show, that there are no huge differences between charged particle production generated by tested models. The differences are in principle observable in pseudorapidity ranges showed in Chapter 4, but the largest differences are of the order of $\approx 10\%$, in other words, it is possible to denote charge particle productions of all generators in accordance with each other. Particular generators are based on different theoretical approaches and philosophy and it is therefore very interesting and quite remarkable, that predictions are so similar.

Generators seem to be most different in "heavier" flavour production (not only charm, but already strangeness). This can be seen from large discrepancies in $K^{\pm}$ and $\mu^{\pm}$. Unstable particles decayed in simulations, and therefore sources of $\mu^{\pm}$ were mainly charmed particles and B-mesons. The production of $K^{\pm}$ is important for CR physics as kaons contribute differently than pions to muon production in extended air showers. Particles with charm are significant sources of $\mu^{\pm}$ and therefore charm production test was performed. HIJING produces almost twice as much charm than QGSJET. Beauty production was not tested as it is not produced in both QGSJET programs.

Regions where differences among generators can be seen in the ATLAS detector are depicted in histograms in Sec. 4.2. Muons turn out to be the most convenient for testing generators and comparison of simulation results with the real data. Muons will be easily detectable in ATLAS and differences among all generators are of the order of tens of percents.

MC generator HIJING does not produce as much energy in very forward regions ($|\eta| > 6$) as other generators, which can be seen in pseudorapidity histograms weighted by energy. Due to this fact, HIJING can not be suitable for generating CR showers.

QGSJET-II contains special processes, which other generators do not have. High p_t is transferred, but only a few secondary particles are produced and such events are called hard diffraction.

Charged particle production is quite in accordance among all generators in proton-nucleus collisions, but differences increase in nucleus-nucleus ones (nitrogen-iron), which gives another opportunity to differentiate generators.

The conclusions can be summarized as follows:

1. There is reasonable agreement at Tevatron energy among tested generators.

2. Remarkable agreement appears at LHC in gross features of particle production. One has to keep in mind that PYTHIA represents pure pQCD model, HIJING is pQCD generator with stress on minijet production, QGSJET is based on Gribov-Regge Theory and QGSJET-II is also based on GRT and includes also some non-linear effects.

3. The main differences are in production of strangeness and charm. The best opportunity to differentiate all generators represents muon production, which is dramatically different in each type of collision for all generators.

4. Particle distributions produced in nucleus-nucleus collisions (nitrogen-iron) are significantly different from those in proton-nucleus collisions. Beside muon production also charged particle distribution is very appropriate to compare real data with simulations in this case.

5. Additional differences among generators can be found in diffractive dissociation events, which is important for CR physics. Testing of such events will depend on detector coverage in very forward region.

Appendix A

Quantities and Variables

- **Rapidity** y is quantity which can be calculated from energy and longitudinal momentum of particle. Let denote longitudinal direction as the the direction of the z axis. Rapidity is then defined as

$$y = \frac{1}{2} \ln \left(\frac{E + p_z}{E - p_z} \right) , \qquad (A.1)$$

where E is particle energy and p_z is z-momentum of particle. Under a boost in the z-direction to a frame with velocity β, $y \to y - \tanh^{-1} \beta$. Hence the shape of the rapidity distribution dN/dy is invariant.

- **Pseudorapidity** η is defined as

$$y = - \ln \tan \left(\frac{\theta}{2} \right) , \qquad (A.2)$$

where $\cos \theta = p_z/p$. The pseudorapidity is approximately equal to the rapidity y for $p \gg m$ and $\theta \gg 1/\gamma$, and in any case can be measured when the mass and momentum of the particle is unknown.

- **Center of mass energy** is an invariant quantity. For case of n particles with masses $m_1, m_2, \ldots, m_n$ and energies $E_1, E_2, \ldots, E_n$ center-of-mass energy can be expressed in the Lorentz-invariant form

$$\sqrt{s} = \left[(E_1 + E_2 + \ldots + E_n)^2 - (\vec{p_1} + \vec{p_2} + \ldots + \vec{p_n})^2 \right]^{1/2} \qquad (A.3)$$

The velocity of the center-of-mass is given in the frame where energies and momenta are denoted identically as in the latter Eq.

$$\beta_{cm} = \frac{\vec{p_1} + \vec{p_2} + \ldots + \vec{p_n}}{E_1 + E_2 + \ldots + E_n} \qquad (A.4)$$

and γ factor of the center-of-mass

$$\gamma_{cm} = \frac{1}{\sqrt{1 - \beta_{cm}^2}} = \frac{E_1 + E_2 + \ldots + E_n}{E_{cm}} \qquad (A.5)$$

75

- **Transverse momentum** $p_\perp$ is given for particle going in z-direction by

$$p_\perp = \sqrt{p_x^2 + p_y^2},$$ (A.6)

where p_x and p_y is Cartesian components of particle momentum.

- **Transverse energy** $E_\perp$ of a jet is given by

$$E_\perp = E \sin(\theta),$$ (A.7)

where E is the energy of a jet and θ is the angle between beam direction and jet.

Appendix B

Configuration of Collisions, Tables

$$(\bar{p}, p, N, S, Fe, [N]) \qquad (p, p, p, p, p, [Fe])$$

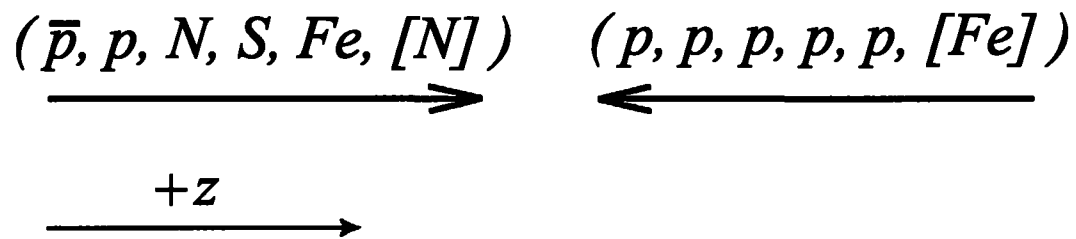$$\longrightarrow \qquad \longleftarrow$$

$$+z$$
$$\longrightarrow$$

Figure B.1: The configuration of collision simulations with orientation of the z-axis. Each particle (nucleus) written in brackets collides with particle (nucleus) from the second beam according to the sequence in brackets.

Collision	Quantity	PYTHIA	HIJING	QGSJET	QGSJET-II
$\bar{p}p$ at Tevatron	$\langle n \rangle_\pi$	43.7	46.3	41.4	37.3
	$\langle E \rangle_\pi$	13.72	11.65	15.69	14.87
	$\langle p_\perp \rangle_\pi$	0.40	0.38	0.45	0.46
	$\langle n_\gamma \rangle /2$	25.7	27.6	28.0	22.3
pp at LHC	$\langle n \rangle_\pi$	90.6	105.2	91.7	91.0
	$\langle E \rangle_\pi$	51.27	41.60	57.12	50.87
	$\langle p_\perp \rangle_\pi$	0.47	0.42	0.47	0.52
	$\langle n_\gamma \rangle /2$	53.3	63.7	59.0	51.2
pN	$\langle n \rangle_\pi$	—	163.3	174.1	145.2
	$\langle E \rangle_\pi$	—	26.70	35.11	39.23
	$\langle p_\perp \rangle_\pi$	—	0.42	0.46	0.51
	$\langle n_\gamma \rangle /2$	—	97.9	115.0	83.7
pS	$\langle n \rangle_\pi$	—	204.3	227.7	175.9
	$\langle E \rangle_\pi$	—	27.53	32.82	37.83
	$\langle p_\perp \rangle_\pi$	—	0.42	0.46	0.52
	$\langle n_\gamma \rangle /2$	—	122.5	149.4	102.1
pFe	$\langle n \rangle_\pi$	—	227.1	262.6	195.8
	$\langle E \rangle_\pi$	—	26.60	30.56	36.40
	$\langle p_\perp \rangle_\pi$	—	0.42	0.46	0.52
	$\langle n_\gamma \rangle /2$	—	137.1	174.6	116.85
NFe	$\langle n \rangle_\pi$	—	1069.0	852.1	1388.1
	$\langle E \rangle_\pi$	—	16.28	24.16	25.57
	$\langle p_\perp \rangle_\pi$	—	0.40	0.43	0.52
	$\langle n_\gamma \rangle /2$	—	639.5	546.5	813.0
pp at ATLAS	$\langle n \rangle_\pi$	86.2	93.4	105.9	91.6
	$\langle E \rangle_\pi$	53.53	37.93	52.54	53.53
	$\langle p_\perp \rangle_\pi$	0.47	0.42	0.47	0.52
	$\langle n_\gamma \rangle /2$	50.7	54.4	68.7	50.6

Table B.1: The mean values of $\pi^\pm$ multiplicities, energy distributions and $p_\perp$ distributions according to particular collisions. Energies and momenta are written in *GeV* units. There is the half of the average multiplicities of γ corresponding to each interactions.

Collision	Quantity	PYTHIA	HIJING	QGSJET	QGSJET-II
$\bar{p}p$ at Tevatron	$\langle n \rangle_K$	4.8	5.5	5.3	3.6
	$\langle E \rangle_K$	16.19	16.04	17.64	19.02
	$\langle p_\perp \rangle_K$	0.55	0.52	0.56	0.53
pp at LHC	$\langle n \rangle_K$	10.2	12.2	11.5	8.0
	$\langle E \rangle_K$	60.22	58.15	65.22	67.91
	$\langle p_\perp \rangle_K$	0.68	0.59	0.59	0.59
pN	$\langle n \rangle_K$	—	18.54	21.1	11.9
	$\langle E \rangle_K$	—	40.35	40.48	51.53
	$\langle p_\perp \rangle_K$	—	0.59	0.58	0.59
pS	$\langle n \rangle_K$	—	23.1	27.2	14.3
	$\langle E \rangle_K$	—	38.34	37.93	49.34
	$\langle p_\perp \rangle_K$	—	0.59	0.58	0.59
pFe	$\langle n \rangle_K$	—	25.6	31.3	15.1
	$\langle E \rangle_K$	—	37.10	35.32	47.83
	$\langle p_\perp \rangle_K$	—	0.59	0.58	0.59
NFe	$\langle n \rangle_K$	—	118.3	102.7	108.3
	$\langle E \rangle_K$	—	22.64	27.57	33.42
	$\langle p_\perp \rangle_K$	—	0.57	0.55	0.59
pp at ATLAS	$\langle n \rangle_K$	9.7	10.9	13.3	7.8
	$\langle E \rangle_K$	62.45	54.62	59.40	68.53
	$\langle p_\perp \rangle_K$	0.68	0.60	0.59	0.59

Table B.2: The mean values of $K^\pm$ distributions (multiplicities, energies, transverse momenta) according to the type of collision. Energies and momenta are written in *GeV* units.

Collision	Quantity	PYTHIA	HIJING	QGSJET
$\bar{p}p$ at Tevatron	$\langle n \rangle_\mu$	0.011	0.006	0.005
	$\langle E \rangle_\mu$	6.03	5.31	7.34
	$\langle p_\perp \rangle_\mu$	0.57	0.66	0.46
pp at LHC	$\langle n \rangle_\mu$	0.027	0.022	0.011
	$\langle E \rangle_\mu$	23.74	17.29	25.81
	$\langle p_\perp \rangle_\mu$	0.80	0.83	0.47
pN	$\langle n \rangle_\mu$	—	0.036	0.020
	$\langle E \rangle_\mu$	—	14.63	13.17
	$\langle p_\perp \rangle_\mu$	—	0.79	0.47
pS	$\langle n \rangle_\mu$	—	0.048	0.025
	$\langle E \rangle_\mu$	—	13.15	11.63
	$\langle p_\perp \rangle_\mu$	—	0.74	0.47
pFe	$\langle n \rangle_\mu$	—	0.054	0.029
	$\langle E \rangle_\mu$	—	14.05	11.76
	$\langle p_\perp \rangle_\mu$	—	0.76	0.48
NFe	$\langle n \rangle_\mu$	—	0.253	0.098
	$\langle E \rangle_\mu$	—	10.85	10.94
	$\langle p_\perp \rangle_\mu$	—	0.66	0.46
pp at ATLAS	$\langle n \rangle_\mu$	0.027	0.021	0.013
	$\langle E \rangle_\mu$	27.15	20.40	20.93
	$\langle p_\perp \rangle_\mu$	0.88	0.84	0.47

Table B.3: The mean values of $\mu^\pm$ multiplicities, energy distributions and $p_\perp$ distributions calculated for all type of collisions. Energies and momenta are written in *GeV* units.

Collision	Quantity	PYTHIA	HIJING	QGSJET	QGSJET-II
$\bar{p}p$ at Tevatron	$\langle n \rangle_p$	2.2	3.1	2.5	2.2
	$\langle E \rangle_p$	133.50	97.49	150.01	164.30
	$\langle p_\perp \rangle_p$	0.57	0.67	0.56	0.57
pp at LHC	$\langle n \rangle_p$	4.8	6.3	5.0	4.5
	$\langle E \rangle_p$	493.80	444.50	355.70	399.50
	$\langle p_\perp \rangle_p$	0.72	0.85	0.64	0.60
pN	$\langle n \rangle_p$	—	9.3	8.4	6.3
	$\langle E \rangle_p$	—	333.20	234.80	406.80
	$\langle p_\perp \rangle_p$	—	0.85	0.64	0.59
pS	$\langle n \rangle_p$	—	11.5	10.7	7.5
	$\langle E \rangle_p$	—	323.30	225.70	419.20
	$\langle p_\perp \rangle_p$	—	0.85	0.65	0.59
pFe	$\langle n \rangle_p$	—	12.7	12.3	8.4
	$\langle E \rangle_p$	—	311.80	213.90	402.80
	$\langle p_\perp \rangle_p$	—	0.84	0.64	0.58
NFe	$\langle n \rangle_p$	—	55.8	38.9	43.2
	$\langle E \rangle_p$	—	200.20	169.20	222.40
	$\langle p_\perp \rangle_p$	—	0.83	0.63	0.60
pp at ATLAS	$\langle n \rangle_p$	4.8	5.6	5.5	4.4
	$\langle E \rangle_p$	551.70	415.50	298.50	401.60
	$\langle p_\perp \rangle_p$	0.71	0.90	0.66	0.59

Table B.4: The mean values of p multiplicities, energy distributions and $p_\perp$ distributions for all studied collisions. Energies and momenta are written in *GeV* units.
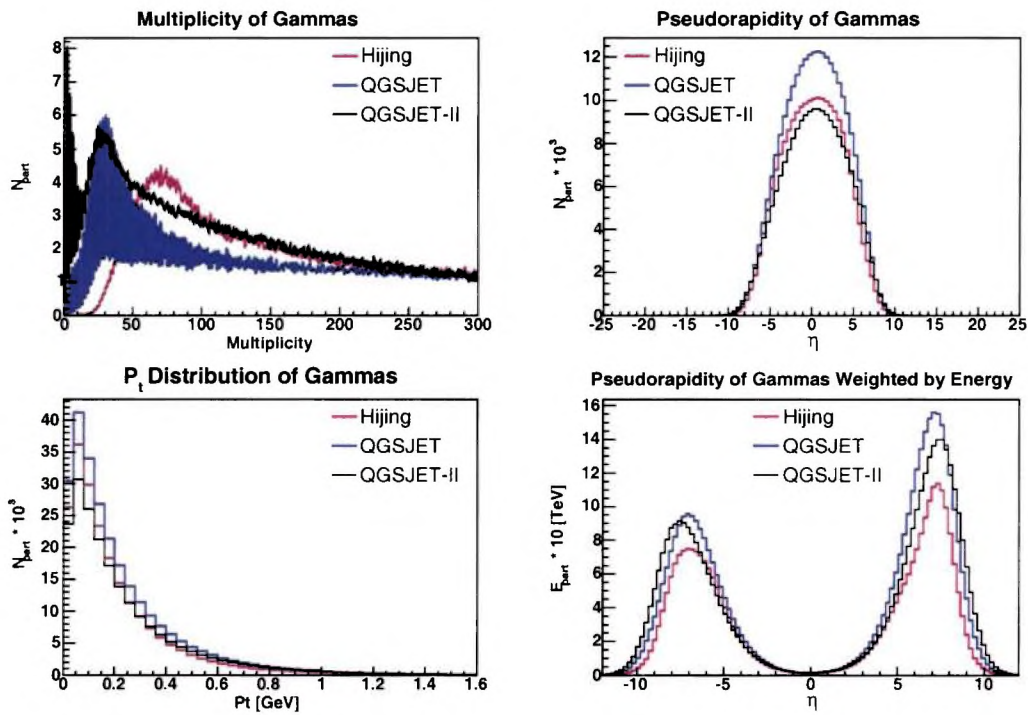
Appendix C

Histograms

Figure C.1: Results of generated collisions of pS at energy $\sqrt{s} = 56\,\text{TeV}$, gamma spectra. Histograms are normalized to 1000 events.
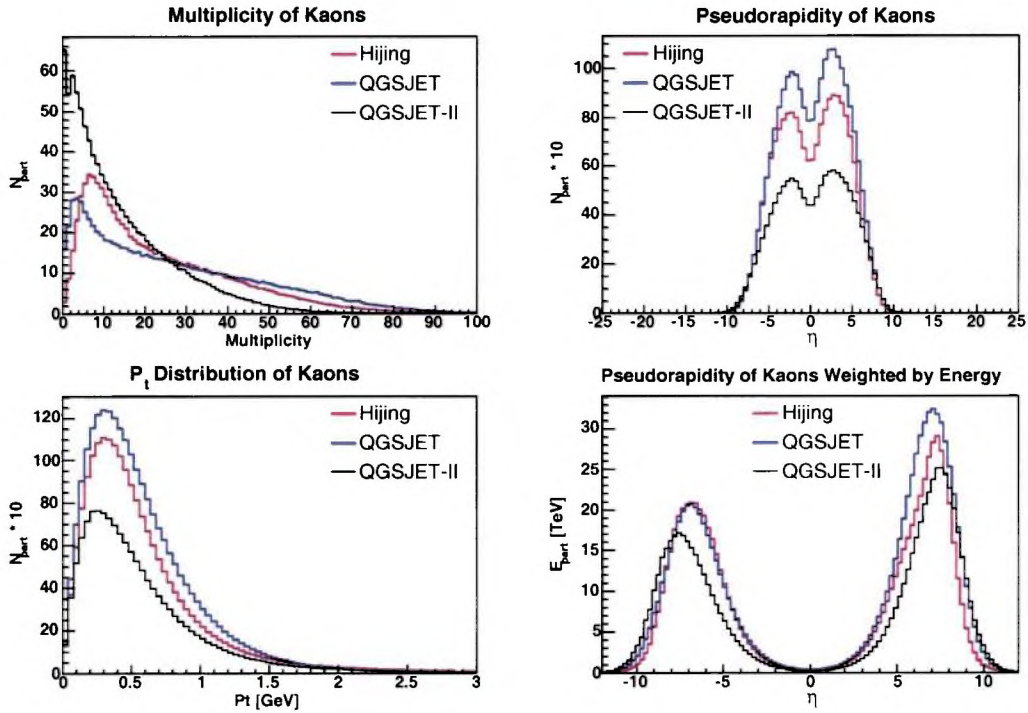
Figure C.2: Results of generated collisions of pS at energy $\sqrt{s} = 56\,\text{TeV}$, charged kaon spectra. Histograms are normalized to 1000 events.
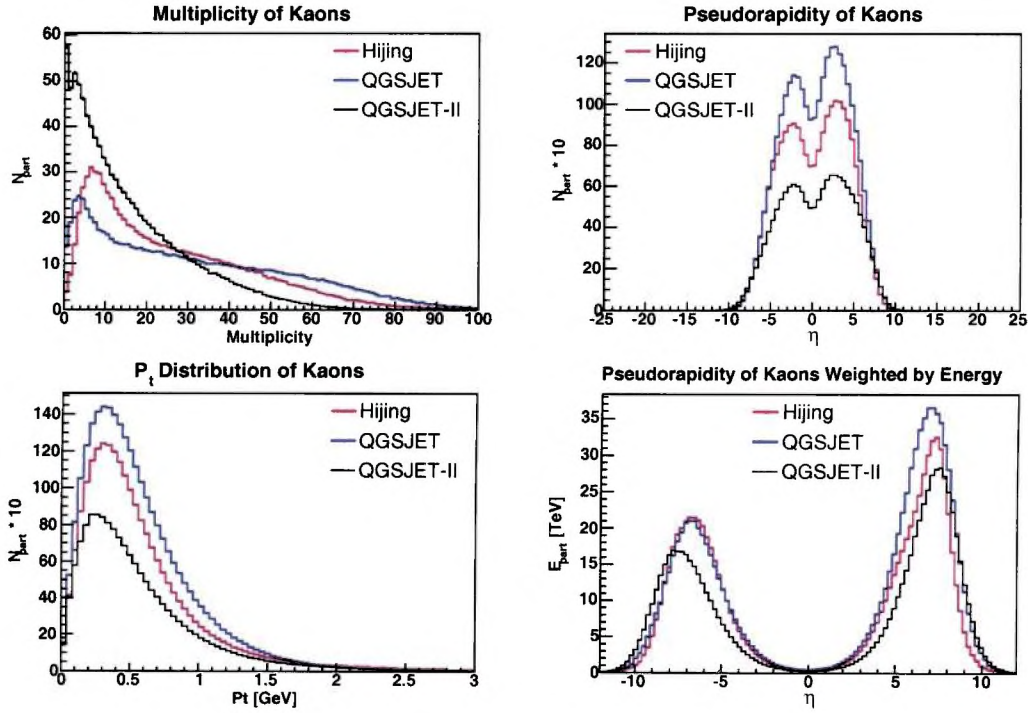
Figure C.3: Results of generated collisions of pFe at energy $\sqrt{s} = 71\,\text{TeV}$, charged kaon distributions. Histograms are normalized to 1000 events.

Bibliography

[1] Milke J. *et al.* (2004): Test of Hadronic Interaction Models with Kascade. *Acta Phys. Pol. B* **35**, 341–348.

[2] Gaisser T. K. (1990): Cosmic Rays and Particle Physics. Cambridge University Press, Cambridge.

[3] Greisen K. (1966): *Phys. Rev. Lett.* **16**, 748.

[4] Zatsepin G. T., Kuzmin V. A. (1966): *Sov. Phys. - JETP Lett.* **4**, 78.

[5] Wikipedia, http://en.wikipedia.org/wiki/Cosmic_ray.

[6] Aronson S. *et al.* (2002): A Nuclear Physics Program at the ATLAS Experiment at the CERN Large Hadron Collider. *Letter of Intent*, Brookhaven National Laboratory.

[7] Chaloupka S. (2002): Multiboson Effects at RHIC. *Diploma Thesis*, Charles University at Prague, 6–23.

[8] Sjostrand S., Eden P., Friberg C., Lonnblad L., Miu G., Mrenna S., Norrbin E. (2001): High-energy physics event generation with PYTHIA 6.1. *Comput. Phys. Commun.* **135**, 238–259.

[9] Kalmykov N. N., Ostapchenko S. S., Pavlov A. I. (1997): *Nucl. Phys. B (Proc. Suppl.)* **52**, 17.

[10] Wang X. N., Gyulassy M. (1991): HIJING: A Monte Carlo model for multiple jet production in p p, p A and A A collisions. *Phys. Rev. D* **44**, 3501.

[11] Ostapchenko S. (2006): *Nucl. Phys. Proc. Suppl. B* **151**, 143.

[12] Steinberg P. A. (2001): Systematics of Charged Particle Production in 4π with the PHOBOS Detector at RHIC, Brookhaven National Laboratory, George Washington University.

[13] Armesto N. (2004): Review of Monte Carlo Methods for Particle Multiplicity Evaluation. *Preprint* hep-ph/0410161.

[14] Antoni T. *et al.* (1999): Test of High-energy Interaction Models Using the Hadronic Core of EAS. *J. Phys. G: Nucl. Part. Phys.* **25**, 2161–2175.

[15] Armesto N. (2000): Central Rapidity Densities of Charged Particles at RHIC and LHC. *Preprint* hep-ph/0002163.

[16] Carrol A. S. *et al.* (1979): *Phys. Lett.* B **80**, 319.

[17] Roberts T. J. *et al.* (1979): *Phys. Lett.* B **159**, 56.

[18] Amos N. A. *et al.* (E710 Collaboration) (1992): *Phys. Rev. Lett.* **68**, 2433.

[19] Abe F. *et al.* (CDF Collaboration) (1994): *Phys. Rev. D* **50**, 5550.

[20] Avila C. *et al.* (E811 Collaboration) (1999): *Phys. Lett. B* **445**, 419.

[21] Heck D., Knapp J., Capdevielle J. N., Schatz G. and Thouw T. (1998): COR-SIKA: A Monte Carlo Code to Simulate Extensive Air Showers. *Report* FZKA 6029 Forschungszentrum Karlsruhe, http://www-ik3.fzk.de/~heck/corsika

[22] Risse M. *et al.* (2001): Test of Hadronic Interaction Models in the Forward region with KASCADE event Rates *J. Phys. G: Nucl. Part. Phys.* **27**, 1785–1798.

[23] Kahana D. E., Kahana S. H. (1998): Two Phase Simulation of Ultrarelativistic Nulear Collisions. *Phys. Rev.* C **58**, 3574 (*Preprint* nucl-th/9804017).

[24] Jeon S., Kapusta J. I. (1997): Linear Extrapolation of Ultrarelativistic Nucleon Nucleon Scattering to Nucleus Nucleus Collisions. *Phys. Rev.* C **56**, 468 (*Preprint* nucl-th/9703033).

[25] Bass A. S., Müller B., Srivastava D. K. (2004): RHIC Physics with the Parton Cascade Model. *J. Phys. G: Nucl. Phys.* **30**, S1283–S1286.

[26] Zhang B., Ko C. M., Li B. A., Lin Z. W. (2000): A Multi-phase Transport Model for Nuclear Collisions at RHIC. *Phys. Rev.* C **61**, 067901 (*Preprint* nucl-th/9907017).

[27] Cheng S., Pratt S., Csizmadia P., Nara Y., Molnar D., Gyulassy M., Vance S. E., Zhang B. (2002): The Effect of Finite-Range Interactions in Classical transport Theory. *Phys. Rev.* C **65** 024901.

[28] Geiger K. (1992): Particle Production in High-Energy Nuclear Collisions: A Parton Cascade Cluster Hadronization Model. *Phys. Rev.* D **47**, 133.

[29] Bass S. A., Müller B., Srivastava D. K. (2003): Parton Rescattering and Screening in Au + Au Collisions at RHIC. *Phys. Lett.* B **551**, 277–283.

[30] Werner K. (1994): String Models for Ultrarelativistic Hadronic Interactions: Concepts, Limitations, and New Directions. *Preprint* nucl-th/9411033.

[31] Kaidalov A. B., Ter-Martinrosyan K. A. (1982) *Phys. Lett.* B **117**, 247.

[32] Amelin N. S., Armesto N., Pajares C., Sousa D. (2001): Monte Carlo Model for Nuclear Collisions from SPS to LHC Energies. *Eur. Phys. J.* C **22**, 149 (*Preprint* hep-ph/01030600).

[33] Ranft J. (1994): The Dual Parton Model at Cosmic Ray Energies. *Phys. Rev.* D **51**, 64.

[34] Drescher H. J., Hladik M., Ostapchenko S., Werner K. (1999): A New Approach to Nuclear Collisions at RHIC Energies. *Nucl. Phys.* A **661**, 604 (*Preprint* hep-ph/9906428).

[35] Andersson B., Tai A. (1996): The Firecracker Model, a Possible Collective Effect in High-energy Heavy Ion Collisions. *Z. Phys.* C **71**, 155.

[36] Werner K. (1993): Strings, Pomerons and the Venus Model of Hadronic Interactions at Ultrarelativistic Energies. *Phys. Rep.* **232**, 87–295.

[37] Andersson B., Gustafson G., Nilsson-Almqvist B. (1987): A Model for Low P(T) Hadronic Reactions, with Generalizations to Hadron-Nucleus and Nucleus-Nucleus Collisions. *Nucl. Phys.* B **281**, 289.

[38] Amelin N. S., Braun M. A., Pajares C. (1993): Multiple Production in the Monte Carlo String Fusion Model. *Phys. Lett.* B **306**, 312.

[39] Andersson B ., Gustafson G., Ingelman G., Sjostrand T. (1983) *Phys. Rep.* **97**, 31.

[40] Wang X. N., Gyulassi M., LBL 31036(1991), LBL 31159(1991).

[41] Haidt D., Zerwas P. M. *et al.* (1998): The European Physical Journal C, Springer-Verlag, Heidelber.

[42] Ostapchenko S. (2001): Modéls for cosmic ray interactions. *Czechoslovak Journal of Physics* **51**, 1.

[43] Sorge H., Stocker H., Greiner W. (1989): Poincare Invariant Hamiltonian Dynamics: Modeling Multi-Hadronic Interactions In a Phase Space Approach. *Annals Phys.* **192**, 266.

[44] Bass S. A. *et al.* (1998): Microscopic Models for Ultrarelativistic Heavy Ion Collisions. *Prog. Part. Nucl. Phys.* **41**, 225 (*Preprint* nucl-th/9803035).

[45] The HSD Transport Approach, *HSD-Homepage*, http://www.th.physik.uni-frankfurt.de/~brat/hsd.html.

[46] Paige F. E., Protopopescu S. D. (1986): Proc. of Summer Study of the Physics of the SSC, Snowmass, CO, USA.

[47] Corcella G. *et al.*, (2001): HERWIG 6.5: An Event Generator for Hadron Emission Reactions With Interfering Gluons (Including Supersymetric Processes). *JHEP* **0101**(2001)010, (arXiv:hep-ph/0011363).

[48] Ordorico, R. (1984) *Comp. Phys. Comm.* **32**, 139.

[49] Ali A., Eijk V., Have I. T. (1987) *Nucl. Phys.* B **292**, 1.

[50] EM Collab., J. Ashman *et al.* (1988): *Phys. Lett.* B **202**, 603.; EM Collab., M. Arneodo *et al.* (1988): *Phys.Lett.* B **211**, 493.

[51] Gyulassy M., Xin-Nian Wang (1997): HIJING 1.0: A Monte Carlo Program for Parton and Particle Production in High Energy Hadronic and Nuclear Collisions. LBL-34346, *Comp. Phys. Comm.* **83**, 307.

[52] HIJING Monte Carlo Program: http://www-nsdth.lbl.gov/~xnwang/hijing/

[53] Chýla J. (1997): Quarks, partons and Quantum Chromodyna-mics, Prague Theory Papers 1997; http://www-hep.fzu.cz/chyla/lectu-res/text.pdf.

[54] PYTHIA (and JETSET) webpage: http://www.thep.lu.se/~torbjorn/Pythia.html.

[55] The ROOT System Home Page: http://root.cern.ch/.

[56] Kaidalov A. B. *et al.* (1986): *Yad. Fiz.* **43**, 1282.

[57] Kalmykov N. N. *et al.* (1985): *Yad. Fiz.* **41**, 947.

[58] Dedenko L. G. (1991): *Izv. Akad. Nauk SSSR Ser. Fiz.* **55**, 720.

[59] Lagutin A. A. *et. al.* (1987): *Leningrad Nucl. Phys. Inst.*, Preprint 1289.

[60] Erlykin A. D. *et. al.* (1985): *Proc. 19th ICRC (La Jolla)* **6**, 92.

[61] Kalmykov N. N. *et. al.* (1994): *Izv. RAN Ser. Fiz* **58**, 12, 21.

[62] Klages H. O. *et. al.* (KASCADE Collaboration) (1997): *Nucl. Phys. B (Proc. Suppl.)* B **52**, 92.

[63] Brož J., Roskovec V., Valouch M. (1980): Fyzikální a matematické tabulky, SNTL, Praha.

[64] ATLAS Collaboration (1999): ATLAS detector and physics performance Technical Design Report Volume I, CERN/LHCC/99-14, CERN.

[65] http://www.hep.phy.cam.ac.uk/~barr/thesispngs/.